НАЦІОНАЛЬНА АКАДЕМІЯ НАУК УКРАЇНИ
ІНСТИТУТ ЗАГАЛЬНОЇ ТА НЕОРГАНІЧНОЇ ХІМІЇ імені В. І. ВЕРНАДСЬКОГО
КИЇВСЬКИЙ НАЦІОНАЛЬНИЙ УНІВЕРСИТЕТ імені ТАРАСА ШЕВЧЕНКА

УКРАЇНСЬКИЙ ХІМІЧНИЙ ЖУРНАЛ

№ 4
Том 88 / Vol. 88
2022
https://ucj.org.ua

UKRAINIAN CHEMISTRY JOURNAL

Зміст

Contents

UDC 621.762.242+661.8...22 doi: 10.33609/2708-129X.88.04.2022.63-78

SYNTHESIS AND CHARACTERIZATION OF $(Ba_{1-x}Sr_x)_7Nb_4MoO_{20}$ POWDERS FOR PROTON-CONDUCTING SOLID OXIDE FUEL CELLS

O. V. Bezdorozhev[1,*], I. V. Solodkyi[2], A. S. Ostroverkh[1], I. A. Morozov[1], Y. M. Ostroverkh[1], Yu. M. Solonin[1]

[1]Frantsevich Institute for Problems of Materials Science of NAS of Ukraine, Krzhizhanovsky str. 3, 03142, Kyiv, Ukraine
[2]National Technical University of Ukraine "Igor Sikorsky Kyiv Polytechnic Institute", Peremogy ave. 37, 03056, Kyiv, Ukraine
**e-mail: oleksii.bezdorozhev@gmail.com*

This work reports on the preparation and characterization of Sr^{2+}-doped $Ba_7Nb_4MoO_{20}$ powders prepared by a solid-state synthesis as promising materials for solid oxide fuel cells. The influence of synthesis parameters and strontium content (x = 0; 0.05; 0.10; 0.15; 0.20) on the phase composition and properties of $(Ba_{1-x}Sr_x)_7Nb_4MoO_{20}$ powders was studied. The results of the phase analysis show that $(Ba_{1-x}Sr_x)_7Nb_4MoO_{20}$ (x = 0; 0.05; 0.10) powders with a minimum amount of secondary phases can be obtained after at least three repeated synthesis cycles at 1060–1080 °C for 10 h. According to the laser diffraction analysis, the synthesized powders comprise particles with a polydisperse size distribution spreading from 0.05 μm to 12 μm and average particle size of 2.1 μm. Electron microscopy observations support these findings and demonstrate that the particles and their aggregates have rounded irregular shape. Moreover, it was found that the morphology and particle size of the powder does not depend on the strontium content. Doping $(Ba_{1-x}Sr_x)_7Nb_4MoO_{20}$ with 15 mol.% and 20 mol.% Sr^{2+} leads to the formation of a significant amount of secondary phases due to exceeding the solubility limit of strontium, thus making these compositions unsuitable for use in solid oxide fuel cells.

Keywords: solid-state synthesis, perovskite, $Ba_7Nb_4MoO_{20}$, powder, electrolyte.

INTRODUCTION

In recent years, the world is increasingly focused on hydrogen energy as one of the clean energy sources [1, 2]. The use of hydrogen will have a positive impact on environmental, energy security and economic development issues [3]. Hydrogen can be obtained by electrolysis of water using electricity produced from excess renewable energy [4, 5]. The produced hydrogen can be burned to generate electricity and heat using fuel cells, which are more efficient than combustion engines [6, 7].

Fuel cells (FCs) are electrochemical devices that can convert the chemical energy

of a fuel directly into electrical and thermal energy [8]. The main advantages of FCs are high efficiency (up to 50%) [9], low level of pollutants and noise emissions, modularity and compact design, which allows easy and quick assemble of power plants with different capacities within one technology [8]. Among many types of FCs, the most promising for electrochemical oxidation of hydrogen are solid oxide fuel cells (SOFCs) with a ceramic oxide electrolyte. SOFCs can be divided into two types with respect to the charge transfer mechanism through a dense electrolyte: oxygen-ion-conducting (O^{2-}-SOFCs) and proton-conducting (H^+-SOFCs). The main advantage of O^{2-}-SOFCs is their flexibility in terms of using different types of gaseous fuel that is oxidized at the anode [10]. While H^+-SOFCs have higher energy conversion efficiency (up to 60%) due to lower activation energy of proton conductivity (0.3–0.6 eV) compared to that of ionic conductivity (0.8–1.1 eV) [11]. In addition, water is formed at the cathode during the operation of H^+-SOFCs, and therefore the fuel does not mix with the products of its oxidation leading to more efficient fuel utilization. High efficiency at low temperatures (500–600 °C) reduces the requirements for other SOFCs components and significantly decreases the rate of their degradation. These advantages provide 27–37% lower cost for production of H^+-SOFC stacks with an operating temperature of 550 °C compared to O^{2-}-SOFCs operating at 800 °C [12].

Solid solutions of $BaZrO_3$ and $BaCeO_3$ with the perovskite-type ABO_3 structure are the most widely used electrolytes for H^+-SOFCs [13–16]. However, the need for high sintering temperatures (up to 1600 °C) [17] and alloying with rare earth oxides encourage the search for new, more technological and cheaper materials with better functional properties.

High proton and oxide ion conductivity in $Ba_7Nb_4MoO_{20}$ compound with a disordered hexagonal perovskite structure has recently been discovered [18, 19]. This perovskite has high oxide ion conductivity in dry oxygen environment and proton conductivity in a humidified or reducing atmosphere. For example, the bulk conductivity in humidified air at 510 °C is about twice as high (4 mS/cm) compared to the conductivity in dry air (1.9 mS/cm). Note that the bulk conductivity of $Ba_7Nb_4MoO_{20}$ in dry oxygen is significantly higher than that for 8YSZ and is comparable with that of $La_{0.8}Sr_{0.2}Ga_{0.83}Mg_{0.17}O_{2.815}$, whereas in humidified air (pH_2O ~0.021 atm) the proton conductivity of $Ba_7Nb_4MoO_{20}$ is close to that of barium cerates. Fop et al. [20] also demonstrated that the positional oxide ion disorder generated by the close proximity of available oxygen sites due to the particular topology of the palmierite layers in hydrated $Ba_7Nb_4MoO_{20}$ contributes to the creation of a frustrated proton sublattice with high proton mobility and low energy diffusion pathways. $Ba_7Nb_4MoO_{20}$ also has low sintering temperature (up to 1200 °C) and relatively high chemical resistance to CO_2 [18].

Two recent papers [18, 19] have noted that the properties of $Ba_7Nb_4MoO_{20}$ can be improved by doping, in this regard we proposed the synthesis of $(Ba_{1-x}Sr_x)_7Nb_4MoO_{20}$ (x = 0.05; 0.10; 0.15; 0.20), where part of Ba atoms is replaced by Sr atoms. The choice of strontium as an alloying additive is due to its similar chemical properties and ionic radius (1.39 Å for Sr^{2+}) to barium (1.49 Å for Ba^{2+}) [21] that will provide partial replacement of barium atoms without destroying the crystal lattice of the perovskite.

ISSN 2708-129X. Укр. хім. журн., 2022

Regarding the synthesis of $Ba_7Nb_4MoO_{20}$, it should be noted that this issue is almost not studied in the available literature. The first report on the synthesis and crystal structure of $Ba_7Nb_4MoO_{20}$ was made by Garcia-Gonzalez et al. [22], who synthesized it by solid-state reaction of $BaCO_3$, Nb_2O_5, and MoO_3 at 1300 °C for 72 hours. Fop et al. [18] reported that a single-phase powder can be obtained after repeated annealing at 1050 °C, while the synthesis at 1100–1150 °C leads to the formation of phases other than $Ba_7Nb_4MoO_{20}$. Whereas in the paper [19], repeated annealing at 900 °C for 10–12 hours was carried out to synthesize $Ba_7Nb_4MoO_{20}$-based materials. Taking into account the discrepancies noted above, as well as the fact that strontium carbonate has a higher melting point (t_m = 1497 °C) than barium carbonate (t_m = 811 °C) [23], we tailored the synthesis parameters and then synthesized $(Ba_{1-x}Sr_x)_7Nb_4MoO_{20}$ with various strontium content (x = 0; 0.05; 0.10; 0.15; 0.20). The phase composition, particles size and morphology of the obtained powders were studied.

EXPERIMENT AND DISCUSSION OF THE RESULTS

Solid-state synthesis was used to obtain powders with nominal compositions of $(Ba_{1-x}Sr_x)_7Nb_4MoO_{20}$, x = 0.05; 0.10; 0.15; 0.20. Barium carbonate ($BaCO_3$, ≥99%, Carl Roth GmbH + Co. KG), strontium carbonate ($SrCO_3$, 99%, Alfa Aesar), niobium(V) oxide (Nb_2O_5, 99.5%, ChemPur Feinchemikalien und Forschungsbedarf GmbH), and molybdenum(VI) oxide (MoO_3, ≥99.8%, Carl Roth GmbH + Co. KG) were used as starting materials. The required amount of materials was mixed and ground in a porcelain mortar. The resulting mechanical mixture was sieved and packed down tightly into the crucible by tamping with a glass rod. The solid-state synthesis of $(Ba_{1-x}Sr_x)_7Nb_4MoO_{20}$ powders was performed in an air muffle furnace at temperatures of 1000–1100 °C (step 20 °C) to determine the best reaction conditions for obtaining powders with the maximum concentration of the required phase. The duration of each synthesis was 10 h, and the number of repeated synthesis operations under the same conditions was varied from two to four in order to optimize the synthesis process as well. The heating rate to the dwell temperature was 8 °C/min, while cooling was allowed to take place naturally. After each annealing the powders were additionally grinded and mixed.

The effect of synthesis temperature and strontium content on the phase composition of powders was investigated by X-ray diffraction method using Rigaku Ultima IV diffractometer (Rigaku Co. Ltd., Japan). The diffractograms were recorded using continuous scanning with a step of 0.05° or with a counting time of 4 s per step at U = 30 kV, I = 30 mA with monochromatic Cu Kα radiation. Phase analysis was performed using the JCPDS database and PDXL2 v. 2.0.3.0 software.

The average crystallite size was calculated using the Scherrer formula [24] from the two most intense diffraction peaks at ~27.8° and ~30.5° corresponding to (014) and (110) planes of $Ba_7Nb_4MoO_{20}$ structure, respectively:

$$D = 0.89\lambda/\beta\cos\theta\,, \qquad (1)$$

where D is the crystallite size, λ is the X-ray wavelength of 1.5406 Å, θ is Bragg diffraction angle, and β is the full wide of half maximum of the XRD peak.

Dislocation density was defined by relation [25]:

$$\delta = 1/D^2. \quad (2)$$

where δ is the dislocation density and D is the crystallite size.

Lattice strain was calculated by using the following equation [25]:

$$\varepsilon = \beta/4\tan\theta, \quad (3)$$

where ε is the strain and β is the full wide of half maximum of the XRD peak.

The particle size distribution of the powders was measured by Bettersizer S3 Plus (Bettersize Instruments Ltd., China), which determine the angular variation in intensity of light scattered as a laser beam passes through a dispersed particulate sample. Distilled water was used as the dispersing medium. An ultrasonic actuator built into the device was used to destroy weak agglomerates. The Fraunhofer evaluation model was applied to process the raw data using associated software.

Electron microscopic studies of the obtained powders were performed on a scanning electron microscope (SEM) Axia ChemiSEM (Thermo Fisher Scientific Inc., USA).

The synthesized $(Ba_{1-x}Sr_x)_7Nb_4MoO_{20}$ powders with a nominal content of Sr^{2+} equal to 5 mol.%, 10 mol.%, 15 mol.%, and 20 mol.% are denoted as BS5NMO, BS10NMO, BS15NMO, and BS20NMO, respectively for convenience.

Chemical reactions between carbonates and metal oxides take place during the heating and holding processes at the annealing temperature of the powder mixture. Due to the low melting point of barium carbonate (t_m = 811 °C) and molybdenum oxide (t_m = 802 °C) [23], the synthesis occurs through the formation of a liquid phase, which accelerates the processes of homogenization and phase formation. After some period of time, the synthesis proceeds in the solid phase due to the formation of more refractory oxides [18], which finally form $Ba_7Nb_4MoO_{20}$ perovskite at optimal solid-state reaction conditions.

To determine the optimal temperature for solid-state reaction, a powder mixture with a nominal composition of $(Ba_{0.9}Sr_{0.1})_7Nb_4MoO_{20}$ was selected as a representative sample, the phase composition of which was investigated within a 2θ range of 23–33°, where the main peaks of the formed phases are located [18, 19]. **Fig. 1** shows XRD patterns of BS10NMO powder after three annealing cycles for 10 h at 1000 °C, 1020 °C, 1040 °C, 1060 °C, 1080 °C, and 1100 °C. According to **Fig. 1a**, the main phase of the powder after synthesis at 1000 °C is a solid solution of strontium in $Ba_7Nb_4MoO_{20}$ (ICDD No. 00-051-0484), there are also two secondary phases, namely, $BaMoO_4$ (ICDD No. 00-029-0193) and $Ba_4SrNb_4O_{15}$ (ICDD No. 00-054-1174). The relative intensity of $Ba_4SrNb_4O_{15}$ phase is high, indicating its high concentration possibly due to the incomplete chemical reaction at low synthesis temperature. While the amount of $BaMoO_4$ phase is very low as indicated by the intensity of the main peak (**Fig. 1a**). The formation of these phases is possible by the following chemical reactions (4) – (6):

$$7(Ba_{1-x}Sr_x)CO_3 + 2Nb_2O_5 + MoO_3 \rightarrow (Ba_{1-x}Sr_x)_7Nb_4MoO_{20} + 7CO_2\uparrow, \quad (4)$$

$$BaCO_3 + MoO_3 \rightarrow BaMoO_4 + CO_2\uparrow, \quad (5)$$

$$4BaCO_3 + SrCO_3 + 2Nb_2O_5 \rightarrow Ba_4SrNb_4O_{15} + 5CO_2\uparrow. \quad (6)$$

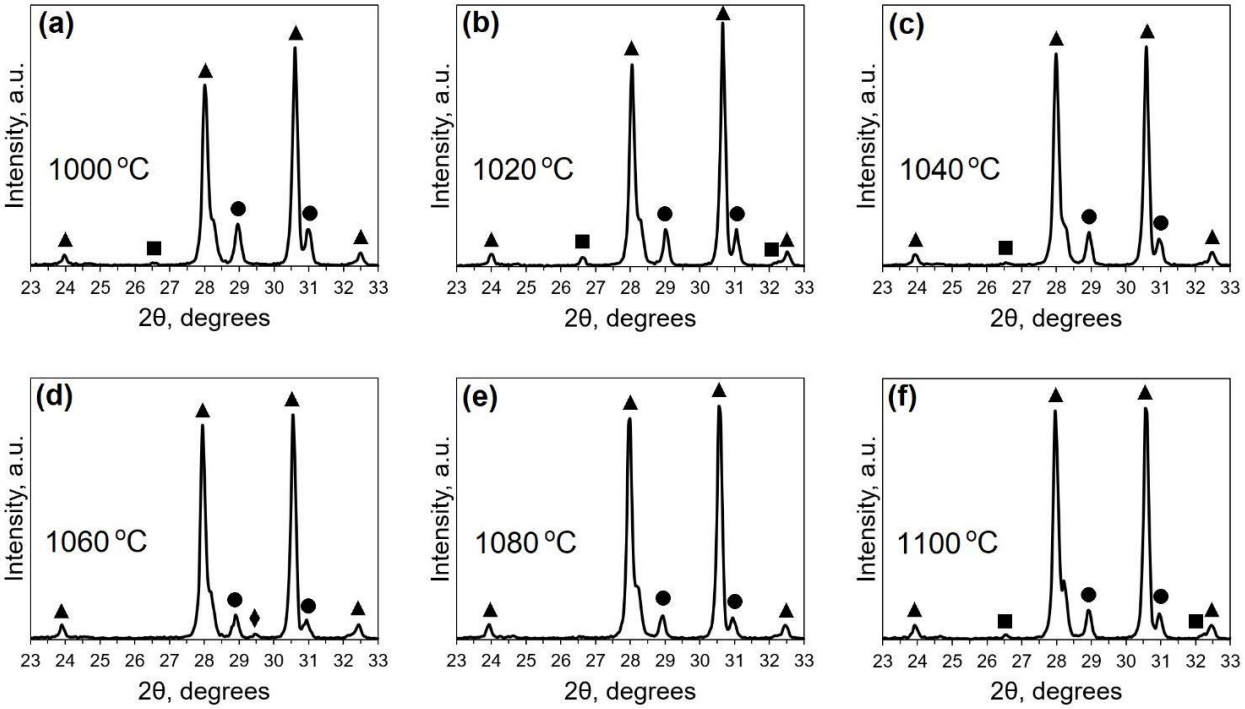

Fig. 1. XRD patterns of BS10NMO powder after sythesis at (a) 1000 °C, (b) 1020 °C, (c) 1040 °C, (d) 1060 °C, (e) 1080 °C, and (f) 1100 °C. Marked peaks: ▲ – $(Ba_{0,9}Sr_{0,1})_7Nb_4MoO_{20}$; ■ – $BaMoO_4$; ● – $Ba_4SrNb_4O_{15}$; ♦ – $Ba_6Nb_3O_{13.5}$.

When the synthesis temperature was increased to 1020 °C (**Fig. 1b**), the phase composition of the powder did not change qualitatively, but the diffraction pattern showed a slight increase in the intensity of $BaMoO_4$ peaks and the opposite for $Ba_4SrNb_4O_{15}$ peaks. This indicates that the amount of $BaMoO_4$ and $Ba_4SrNb_4O_{15}$ is slightly increased and decreased, respectively. A further increase in the synthesis temperature to 1040 °C (**Fig. 1c**) led to an increase in the intensity of the main phase peaks, while the intensities of $BaMoO_4$ and $Ba_4SrNb_4O_{15}$ peaks decreased, which is accompanied by the disappearance of less intense $BaMoO_4$ peak at 2θ = ~32.1°. These results indicate that the chemical reaction (4) proceeds more quickly with increasing synthesis temperature.

At the synthesis temperature of 1060 °C (**Fig. 1d**), the tendency of reducing the intensities of secondary phases still continues. As a result, the $BaMoO_4$ phase disappeared completely, and the intensity of $Ba_4SrNb_4O_{15}$ peaks decreased by about a quarter. However, the diffraction pattern shows a peak at 2θ = 29.5°, which most likely belongs to $Ba_6Nb_3O_{13.5}$ (ICDD No. 00-035-0933). This phase has two main most intense peaks, which are located at 2θ = 27.51° and 29.55°. The peak at 27.51° is not observed, apparently due to its lower intensity in this case. The formation of $Ba_6Nb_3O_{13.5}$ is most likely due to the inhomogeneous distribution

of the starting materials in the mixture and/or incomplete solid-state synthesis reactions [18]. It should be noted that the content of $Ba_6Nb_3O_{13.5}$ phase in the obtained powder is insignificant.

Increasing the synthesis temperature to 1080 °C under other identical conditions (triple annealing for 10 h) resulted in the powder that in addition to the main phase, contains only one secondary phase, namely $Ba_4SrNb_4O_{15}$ (see **Fig. 1e**). As could be suggested from the relative intensity of $Ba_4SrNb_4O_{15}$ peaks (**Fig. 1e**), the amount of this phase is low in comparison with the samples obtained at 1000-1040 °C and remains almost the same as after synthesis at 1060 °C (**Fig. 1d**).

When the synthesis temperature was increased further to 1100 °C (**Fig. 1f**), $BaMoO_4$ formed and the relative intensity of $Ba_4SrNb_4O_{15}$ phase increased, indicating its higher content in the synthesized powder. The most probable reason for this is the decomposition of $(Ba_{0.9}Sr_{0.1})_7Nb_4MoO_{20}$ to $Ba_4SrNb_4O_{15}$ and $BaMoO_4$ due to the low thermal stability of $(Ba_{0.9}Sr_{0.1})_7Nb_4MoO_{20}$ at high temperatures [18] and the evaporation of barium oxide [26, 27], according to the chemical reaction (7):

$$(Ba_{1-x}Sr_x)_7Nb_4MoO_{20} \rightarrow Ba_{4-x}Sr_xNb_4O_{15} + Ba_{1-x}MoO_4 + BaO\uparrow. \quad (7)$$

Thus, according to the obtained XRD results, the optimal temperature interval for solid-state synthesis of $(Ba_{1-x}Sr_x)_7Nb_4MoO_{20}$ is 1060–1080 °C that provides a minimum concentration of secondary phases in the powder.

In the case of solid-state synthesis, it is common that the intermediates of the reaction can be located in different parts of the volume of the powder mixture and have different reactivity, as a result the efficiency of further interaction in the system is significantly reduced. Therefore, in order to achieve homogeneous phase chemistry, it is necessary to further activate the reactivity in the system, which can be done by repeated procedures of grinding and mixing the reaction products, followed by prolonged annealing [18, 19, 28, 29].

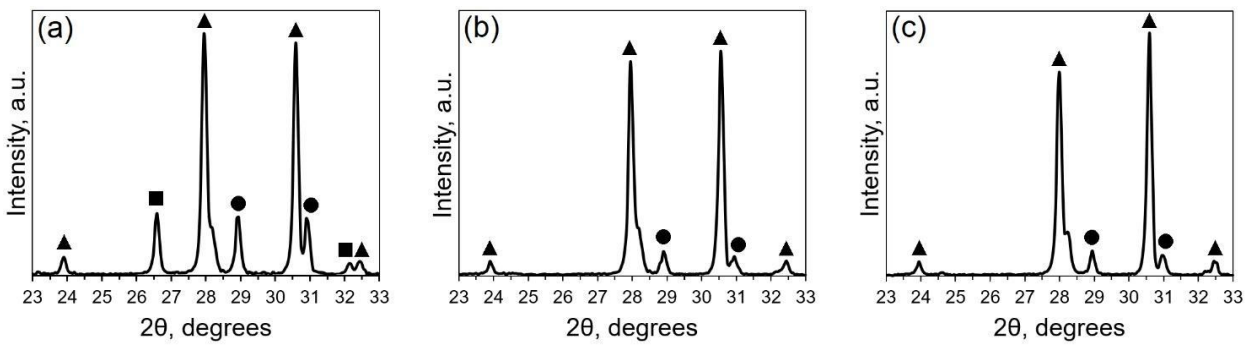

Fig. 2. XRD patterns of BS10NMO powder after (a) two, (b) three, and (c) four repeated synthesis cycles at 1080 °C for 10 h. Marked peaks: ▲ – $(Ba_{0,9}Sr_{0,1})_7Nb_4MoO_{20}$; ■ – $BaMoO_4$; ● – $Ba_4SrNb_4O_{15}$.

The XRD pattern in **Fig. 2a** indicates that double annealing at 1080 °C for 10 h is not enough to obtain pure BS10NMO powder. Although the main phase is $(Ba_{1-x}Sr_x)_7Nb_4MoO_{20}$, there are still significant amounts of residual phases such as $BaMoO_4$ and $Ba_4SrNb_4O_{15}$. After triple synthesis processes, the concentration of $Ba_4SrNb_4O_{15}$ notably reduced, while $BaMoO_4$ phase disappeared (**Fig. 2b**). The obtained powder was then additionally subjected to the synthesis procedure in order to eliminate unwanted phases. However, as can be seen from **Fig. 2c**, the phase composition and intensity of the peaks remained much the same indicating that the reaction closely approached its thermodynamic equilibrium and further repeated annealing can be considered as ineffective [29]. Thus, under the applied synthesis conditions, the solid-state synthesis process should be repeated not less than three times in order to obtain $(Ba_{1-x}Sr_x)_7Nb_4MoO_{20}$ perovskite with a small amount of secondary phases.

Using the above-established optimized synthesis parameters we carried out solid-state synthesis of a series of $(Ba_{1-x}Sr_x)_7Nb_4MoO_{20}$ (x = 0; 0.05; 0.10; 0.15; 0.20) powders and studied their XRD structural parameters.

According to the XRD pattern shown in **Fig. 3a**, the powder without the strontium additive contains two phases, namely $Ba_7Nb_4MoO_{20}$ and $Ba_5Nb_4O_{15}$, after triple annealing at 1060 °C for 10 h. From the ratio of peaks' intensity in **Fig. 3a**, it can be suggested that the amount of $Ba_5Nb_4O_{15}$ phase is small.

In the case of BS5NMO powder (**Fig. 3b**), it can be seen that except the peaks of the main phase (solid solution of Sr in $Ba_7Nb_4MoO_{20}$), there are other peaks which belong to $Ba_4SrNb_4O_{15}$ and $Ba_6Nb_3O_{13.5}$ phases. The small intensity of the peaks of $Ba_6Nb_3O_{13.5}$ indicates that the amount of this phase is very small, while the amount of $Ba_4SrNb_4O_{15}$ remained almost the same compared to that of $Ba_5Nb_4O_{15}$ phase in the powder without strontium additive.

To synthesize $(Ba_{1-x}Sr_x)_7Nb_4MoO_{20}$ with 10–20 mol.% Sr^{2+}, the temperature of multiple annealing was increased to 1080 °C in order to accelerate the diffusion processes due to the increase in the powder mixture of more refractory $SrCO_3$ (t_m = 1497 °C) compared to $BaCO_3$ (t_m = 811 °C) [23]. The XRD pattern of BS10NMO powder in **Fig. 3c** shows that in addition to the main peaks of $Ba_7Nb_4MoO_{20}$-based oxide, there are peaks that belong to $Ba_4SrNb_4O_{15}$, while $Ba_6Nb_3O_{13.5}$ or $BaMoO_4$ phases were not detected. It should be noted that the amount of $Ba_4SrNb_4O_{15}$ phase in BS10NMO powder is slightly higher compared to that of BS5NMO powder as indicated by the increased intensity of the respective peaks.

According to the XRD pattern of BS15NMO powder in **Fig. 3d**, an increase in strontium content to 15 mol.% resulted in the formation of $BaMoO_4$ and $Ba_3Nb_6O_{13.5}$ phases, which have relatively high intensity of XRD peaks. There is also a significant increase in the intensity and number of $Ba_4SrNb_4O_{15}$ peaks indicating an increase in the amount of this phase in the powder. However, the solid solution of Sr in $Ba_7Nb_4MoO_{20}$ remains as the main phase in the synthesized powder. The most probable reason for such a significant increase in the amount of secondary phases is that Sr reached its solubility limit in $Ba_7Nb_4MoO_{20}$, and as a result the excess amount of Sr leads to redistribution of elements and formation of secondary phases. It should be noted that the crystal lattice parameters of $(Ba_{1-x}Sr_x)_7Nb_4MoO_{20}$ phase in BS10NMO and BS15NMO powders remained unchanged.

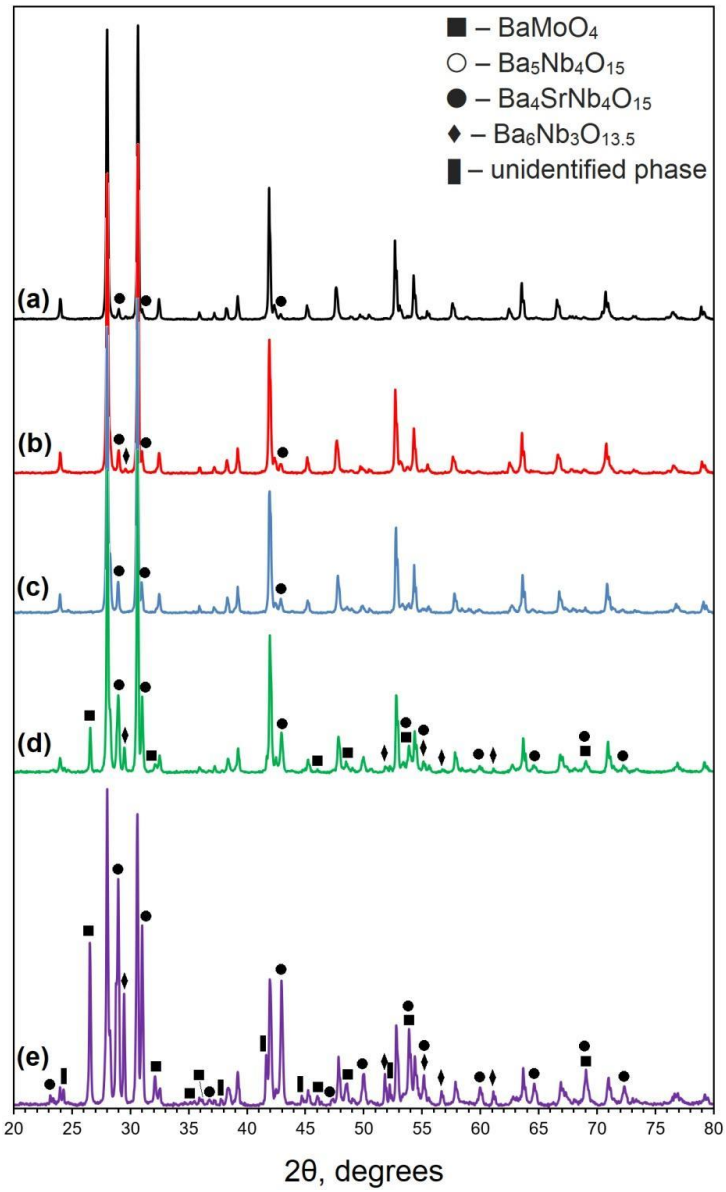

Fig. 3. XRD patterns of (a) $Ba_7Nb_4MoO_{20}$, (b) BS5NMO, (c) BS10NMO, (d) BS15NMO, and (e) BS20NMO powders. All unmarked peaks correspond to the main $(Ba_{1-x}Sr_x)_7Nb_4MoO_{20}$ phase.

As can be seen from **Fig. 3e**, when barium is partially replaced by 20 mol.% Sr^{2+}, there is a further remarkable increase in the intensity of the diffraction peaks of $BaMoO_4$, $Ba_3Nb_6O_{13.5}$, $Ba_4SrNb_4O_{15}$, and unidentified phase with a simultaneous decrease in the intensity of $(Ba_{1-x}Sr_x)_7Nb_4MoO_{20}$ phase, leading to a significant difference in phase composition from the expected one. Thus, BS15NMO and BS20NMO materials cannot be used as an electrolyte for

ISSN 2708-129X. Укр. хім. журн., 2022

H^+-SOFCs because they contain a significant amount of $BaMoO_4$, $Ba_4SrNb_4O_{15}$, $Ba_3Nb_6O_{13.5}$ phases, which do not possess high ionic or proton conductivities [30–32].

It should be noted that Sr-based impurity phases were not detected in the synthesized powders (**Fig. 3**). The reason for this lies in the following facts: (a) Ba and Sr have similar chemical properties; (b) strontium has smaller ionic radius than that of barium [21]; (c) the used concentration of Sr^{2+} to dope $Ba_7Nb_4MoO_{20}$ was low (5–20 mol.%). Therefore, strontium would rather substitute part of barium atoms in Ba-based compounds than form separate Sr-based phases.

The crystal lattice parameters of $(Ba_{1-x}Sr_x)_7Nb_4MoO_{20}$ (x = 0; 0.05, 0.10, 0.15, 0.20) perovskites are given in **Table 1**. It can be seen that the crystal lattice parameters of the synthesized perovskites have a tendency to decrease with increase Sr content due to the smaller ionic radius of Sr^{2+} (1.32 Å) compared to that of Ba^{2+} (1.49 Å) [21]. The volume of the crystal lattice of $Ba_7Nb_4MoO_{20}$ decreases by ~ 0.57% and ~ 0.71% with the addition of 5 mol.% Sr^{2+} and 10 mol.% Sr^{2+}, respectively. The variations in the crystal lattice parameters and unit cell volume indicated that the strontium ion is entering in the lattice of $Ba_7Nb_4MoO_{20}$ perovskite.

The crystallite size of $(Ba_{1-x}Sr_x)_7Nb_4MoO_{20}$ (x = 0; 0.05, and 0.10) powders was found to be in the range of 45–53 nm (**Table 1**). It follows the same trend of decreasing values with increasing strontium content reaching a minimum at 10 mol.%. This can be due to the increase in lattice strains because of ionic size mismatch as ionic size of Sr^{2+} is lower than that of Ba^{2+}. The strain increases with the increase in strontium content due to the distortion of the lattice. The incorporation of Sr into $(Ba_{1-x}Sr_x)_7Nb_4MoO_{20}$ not only produced lattice distortion but lattice defects and nucleation centers which inhibits the growth of the perovskite crystals. With increasing the Sr doping content to 15 mol.% and 20 mol.%, some fluctuations in the width and intensity of the two main diffraction peaks of the main phase are observed (**Fig. 3**). Although the lattice parameters remain unchanged (**Table 1**), the other structural parameters of BS15NMO and BS20NMO powders most likely to be affected by significant amount of impurity phases and chemical inhomogeneity [25].

Table 1

Structural parameters of $(Ba_{1-x}Sr_x)_7Nb_4MoO_{20}$ perovskites.

Powder	Lattice parameters			Unit cell volume, Å^3	Crystallite size, nm	Lattice strain, %	Dislocation density, m^{-2}
	a, Å	*b*, Å	*c*, Å				
$Ba_7Nb_4MoO_{20}$	5.861	5.861	16.518	491.4	53	0.264	$3.63\cdot10^{17}$
BS5NMO	5.852	5.852	16.473	488.6	48	0.299	$4.53\cdot10^{17}$
BS10NMO	5.842	5.842	16.409	485.1	45	0.308	$4.94\cdot10^{17}$
BS15NMO	5.842	5.842	16.409	485.1	51	0.267	$3.84\cdot10^{17}$
BS20NMO	5.842	5.842	16.409	485.1	43	0.317	$5.41\cdot10^{17}$

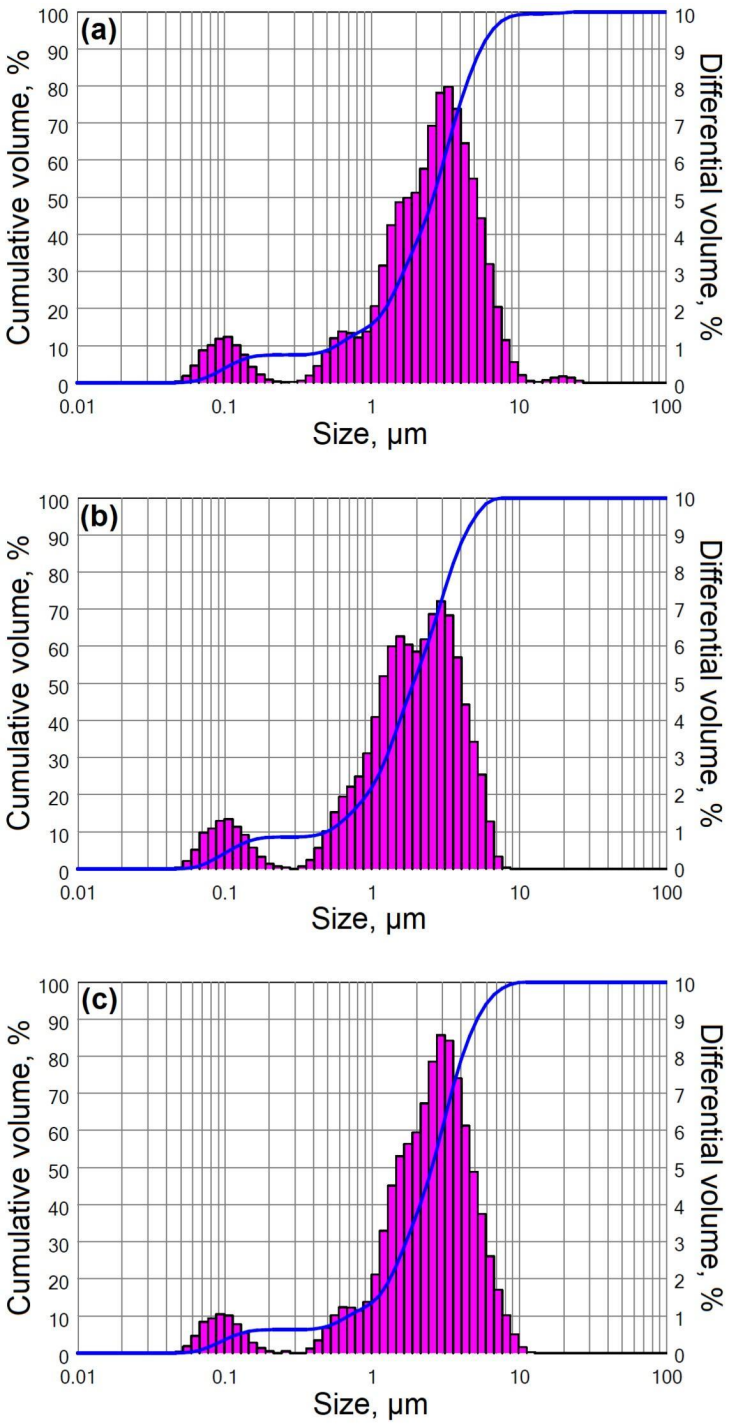

Fig. 4. Particle size distribution of (a) $Ba_7Nb_4MoO_{20}$, (b) BS5NMO, and (c) BS10NMO powders.

Particle size distribution is an important characteristic of powders that influences their physical and chemical properties, and, accordingly, their technological properties as well as the feasibility of their practical use [33]. For example, the particle size of the powder affects its behavior during compaction and sintering, as well as such characteristics of the sintered products as microstructure, physical and mechanical properties [34–38].

In **Fig. 4** and **Table 2** is presented the results of the particle size analysis of the powders with different strontium content in $(Ba_{1-x}Sr_x)_7Nb_4MoO_{20}$ perovskite. It should be noted that the particle size distribution and morphology of BS15NMO and BS20NMO powders was not studied here due to the significant amount of the secondary phases that can affect the results. A comparison of the particle size distribution of $Ba_7Nb_4MoO_{20}$, BS5NMO, and BS10NMO powders suggests that their size distribution is approximately the same and does not depend on the phase and chemical composition of the powders. The particle size of the synthesized powders is in the range of 0.05–12 μm, and their average size is about 2.1 μm.

Table 2

Particle size distribution of $(Ba_{1-x}Sr_x)_7Nb_4MoO_{20}$ powders.

Powder	Size (d_n) below which n-percent of the particles is contained, μm										Span
	d_3	d_6	d_{10}	d_{16}	d_{25}	d_{50}	d_{75}	d_{84}	d_{90}	d_{97}	
$Ba_7Nb_4MoO_{20}$	0.09	0.12	0.50	0.76	1.10	1.90	3.10	3.68	4.28	5.53	1.98
BS5NMO	0.09	0.12	0.49	0.76	1.10	1.90	3.09	3.69	4.27	5.53	1.99
BS10NMO	0.09	0.16	0.69	1.15	1.51	2.54	3.75	4.45	5.16	6.91	1.76

The obtained powders are polydisperse and show a weak bimodal distribution with a relatively small fraction of fine particles of ~50–110 nm in size and coarse particles with sizes from ~0.4 μm to 12 μm. The volume contribution of the fine fraction does not exceed 12%. The majority of the particles are within the 1.5–5 μm size range and the span of the particle size distribution is 1.76–1.99. The formation of the coarse powder fraction is due to the sintering of small particles into dense aggregates during synthesis at high temperatures. While the formed aggregates cannot be effectively destroyed by the applied methods in this study. The relatively small particle size of the powders was obtained as the result of using starting powder materials with particles less than 5 μm in size, as well as due to the fast nucleation and slow growth of $(Ba_{1-x}Sr_x)_7Nb_4MoO_{20}$ phase [39].

Electron microscopic studies were performed to investigate the morphology and size of $(Ba_{1-x}Sr_x)_7Nb_4MoO_{20}$ particles after solid-state synthesis. According to **Fig. 5**, particles and their aggregates are characterized mainly by a rounded irregular shape, which is the result of formation of new phase, sintering of nano- and submicron particles, and disintegration of large agglomerates during grinding of synthesis products. Particles and their

aggregates are characterized by a relatively wide size distribution, which is in the range of 0.3–10 μm. The size of most particles does not exceed 5 μm, while the fraction of particles/aggregates with sizes between about 5 μm and 10 μm is relatively small. According to SEM analysis of $(Ba_{1-x}Sr_x)_7Nb_4MoO_{20}$ powders, it can be concluded that the morphology and particle size of the powder does not depend on the strontium content. Thus, the effect of particle size on the powder compaction behavior will be the same for powders with different strontium content [38]. It should be noted that the results obtained by SEM and laser diffraction measurements are in good agreement indicating the correctness of the applied research methods. Our future efforts will be focused on the preparation of the electrolyte and anode from the synthesized powders and their characterization for SOFC application.

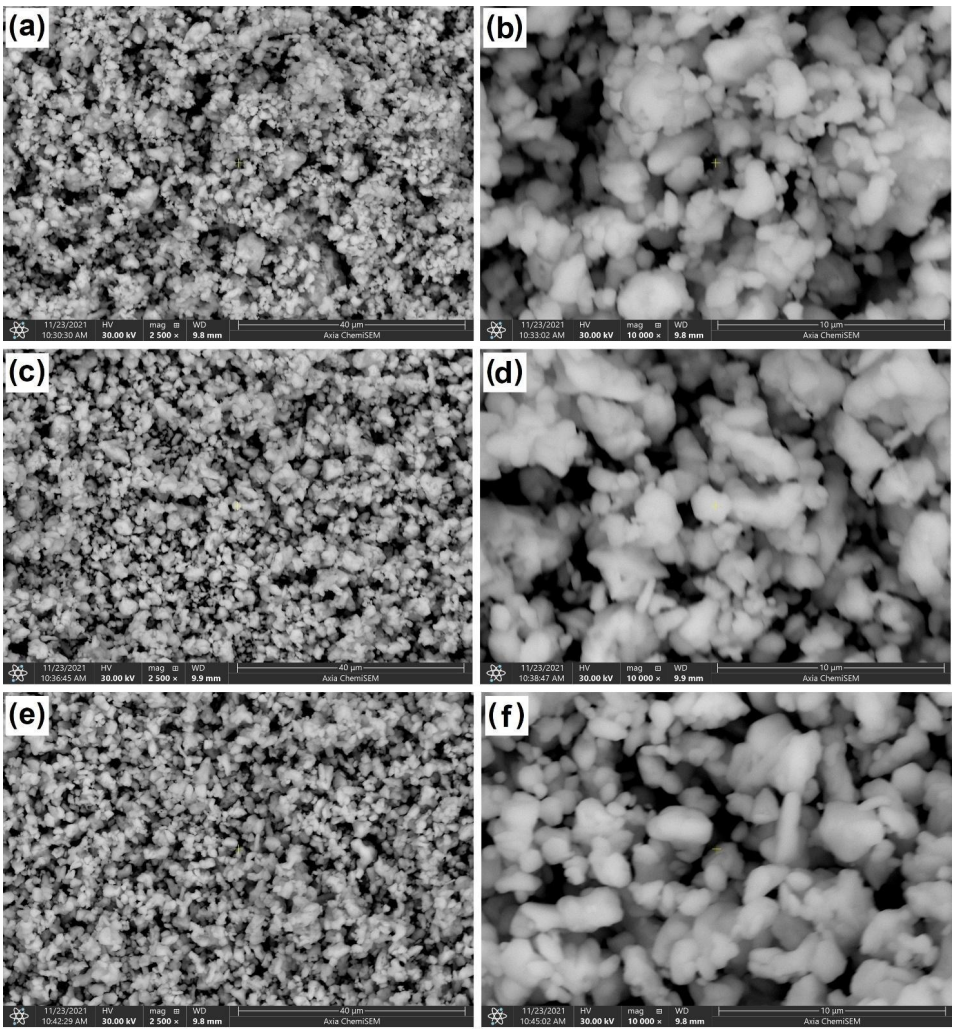

Fig. 5. SEM images of (a, b) $Ba_7Nb_4MoO_{20}$, (c, d) BS5NMO, and (e, f) BS10NMO powders at magnification of 2500× (a, c, e) and 10000× (b, d, f).

CONCLUSIONS

The effect of solid-state synthesis conditions and strontium content on the phase composition and properties of $(Ba_{1-x}Sr_x)_7Nb_4MoO_{20}$ powders was studied. It was found that the optimal temperature interval for solid-state synthesis of $(Ba_{1-x}Sr_x)_7Nb_4MoO_{20}$ (x = 0; 0.05; 0.10) powders with a minimum content of secondary phases is 1060–1080 °C. Moreover, under the applied synthesis temperatures, the solid-state synthesis process should be repeated not less than three times. The X-ray diffraction patterns reveal the formation of $(Ba_{1-x}Sr_x)_7Nb_4MoO_{20}$ perovskites with an average crystallite size in the range of 45–53 nm. The crystallite size decreases with the increase of Sr^{2+} content due to the increase in lattice strains which suppress the growth of the crystals. It was observed that an increase in the strontium content in $(Ba_{1-x}Sr_x)_7Nb_4MoO_{20}$ above 10 mol.% leads to redistribution of elements and formation of significant amount of $BaMoO_4$, $Ba_3Nb_6O_{13.5}$, and $Ba_4SrNb_4O_{15}$. According to the laser diffraction method, the synthesized $(Ba_{1-x}Sr_x)_7Nb_4MoO_{20}$ powders had particle size in the range of 0.05–12 μm with an average size of about 2.1 μm. Moreover, the size of the particles was found not to depend on the strontium content and was mainly influenced by synthesis parameters, size of starting powders, and grinding efficiency after repeated annealing operations. These results correlate with the results obtained by electron microscopy, according to which the particles and their aggregates have rounded irregular shape. The study findings indicate that 15 mol.% and 20 mol.% Sr^{2+}-doped $Ba_7Nb_4MoO_{20}$ cannot be used as an electrolyte for H^+-SOFCs due to the significant amount of second phases.

ACKNOWLEDGMENTS. This study was performed under the project 2020.02/0301 "Development of new functional materials for the needs of hydrogen energy" funded by the National Research Foundation of Ukraine.

СИНТЕЗ ТА ВЛАСТИВОСТІ ПОРОШКІВ $(Ba_{1-x}Sr_x)_7Nb_4MoO_{20}$ ДЛЯ ПРОТОН-ПРОВІДНИХ ТВЕРДООКСИДНИХ ПАЛИВНИХ КОМІРОК

О. В. Бездорожев[1,*], Є. В. Солодкий[2], А. С. Островерх[1], І. А. Морозов[1], Є. М. Островерх[1], Ю. М. Солонін[1]

[1]Інститут проблем матеріалознавства ім. І. М. Францевича НАН України, вул. Кржижановського 3, Київ 03142, Україна
[2]National Національний технічний університет України «Київський політехнічний інститут імені Ігоря Сікорського», просп. Перемоги 37, Київ 03056, Україна
**e-mail: oleksii.bezdorozhev@gmail.com*

Одним із перспективних напрямів вироблення та споживання електричної енергії є воднева енергетика. Для вироблення електроенергії з водню найефективніше використовувати електрогенеруючі установки на основі твердооксидних паливних комірок (ТОПК) із протонною провідністю електроліту завдяки їхній високій ефективності за робочих температур 500–600 °C. Для використання в ролі електроліту перспективними вважають матеріали на основі гексагонального перовськіту $Ba_7Nb_4MoO_{20}$, властивості якого можуть бути покращені шляхом його легування. У зв'язку з цим

нами було запропоновано здійснити синтез перовськіту $Ba_7Nb_4MoO_{20}$, в якому частина атомів барію була б заміщена атомами стронцію, та відпрацювати умови його синтезу. Отже, в цій роботі досліджено вплив параметрів твердофазного синтезу та вмісту стронцію на фазовий склад та властивості порошків із номінальним складом $(Ba_{1-x}Sr_x)_7Nb_4MoO_{20}$ (x = 0; 0,05; 0,10; 0,15; 0,20). Для цього використані такі методи дослідження, як рентгенівська дифракція, скануюча електронна мікроскопія та лазерна дифракція. Відповідно до результатів рентгенофазового аналізу порошків, синтезованих за 1000–1100 °С, встановлено, що оптимальним температурним інтервалом для одержання перовськітів $(Ba_{1-x}Sr_x)_7Nb_4MoO_{20}$ (x = 0; 0,05; 0,10) із мінімальним вмістом вторинних фаз є 1060–1080 °С. Тоді як необхідна кількість повторних відпалів по 10 год має бути не менше трьох. При вмісті стронцію 15 мол.% та 20 мол.% спостерігаємо суттєве зростання вмісту вторинних фаз ($BaMoO_4$, $Ba_4SrNb_4O_{15}$, $Ba_6Nb_3O_{13,5}$) внаслідок досягнення границі розчинності Sr в $Ba_7Nb_4MoO_{20}$, що виключає можливість використання зазначених перовськітів як електроліту ТОПК. Дослідження гранулометричного складу порошків $(Ba_{1-x}Sr_x)_7Nb_4MoO_{20}$ (x = 0; 0,05; 0,10) показало, що дисперсність порошків не залежить від їхнього хімічного складу та визначається в основному дисперсністю вихідних речовин, умовами синтезу та ефективністю подрібнення порошку після повторних операцій відпалу. Встановлено, що розмір частинок порошків $(Ba_{1-x}Sr_x)_7Nb_4MoO_{20}$ знаходиться в діапазоні 0,05–12 мкм, тоді як їхній середній розмір складає 2,1 мкм. Ці результати співпадають із результатами електронної мікроскопії, відповідно до якої частинки порошку мають неправильну округлу форму, яка зумовлена процесами формоутворення, що відбуваються під час утворення нової фази з вихідних речовин, руйнування/агломерації частинок під час подрібнення продуктів синтезу та спікання малих частинок під дією температури.

Ключові слова: твердофазний синтез, перовськіт, порошок, $Ba_7Nb_4MoO_{20}$, електроліт.

REFERENCES

1. Falcone P. M., Hiete M., Sapio A. Hydrogen economy and sustainable development goals: Review and policy insights. *Current Opinion in Green and Sustainable Chemistry*. 2021. **31**: 100506. https://doi.org/10.1016/j.cogsc.2021.100506.
2. Abdin Z., Zafaranloo A., Rafiee A., Merida W., Lipinski W., Khalilpour K.R. Hydrogen as an energy vector. *Renewable and Sustainable Energy Reviews*. 2020. **120**: 109620. https://doi.org/10.1016/j.rser.2019.109620.
3. Sun T., Ocko I. B., Sturcken E., Hamburg S. P. Path to net zero is critical to climate outcome. *Scientific Reports*. 2021. **11**: 22173. https://doi.org/10.1038/s41598-021-01639-y.
4. Fan L., Tu Z., Chan S. H. Resent development of hydrogen and fuel cell technologies: A review. *Energy Reports*. 2021. **7**: 8421–8446. https://doi.org/10.1016/j.egyr.2021.08.003.
5. Venkataraman V., Perez-Fortes M., Wang L., Hajimolana Y. S., Boigues-Munoz C., Agostini A., McPhail S. J., Marechal F., Herle J. V., Aravind P. V. Reversible solid oxide systems for energy and chemical applications – Review & perspectives. *Journal of Energy Storage*. 2019. **24**: 100782.

https://doi.org/10.1016/j.est.2019.100782.
6. Abdalla A. M.,Hossain S., Petra P. M., Ghasemi M., Azad A. K. Achievements and trends of solid oxide fuel cells in clean energy field: a perspective review. *Frontiers in Energy*. 2020. **14**: 359–382. https://doi.org/10.1007/s11708-018-0546-2.
7. Chuahy F. D. F., Kokjohn S. L. Solid oxide fuel cell and advanced combustion engine combined cycle: A pathway to 70% electrical efficiency. *Applied Energy*. 2019. **235**: 391–408. https://doi.org/10.1016/j.apenergy.2018.10.132.
8. Singh M., Zappa D., Comini E. Solid oxide fuel cell: Decade of progress, future perspectives and challenges. *International Journal of Hydrogen Energy*. 2021. **46**(54): 27643–27674. https://doi.org/10.1016/j.ijhydene.2021.06.020.
9. Azizi M. A., Brouwer J. Progress in solid oxide fuel cell-gas turbine hybrid power systems: System design and analysis, transient operation, controls and optimization. *Applied Energy*. 2018. **215**: 237–289. https://doi.org/10.1016/j.apenergy.2018.01.098.
10. Zhang W., Hu Y. H. Progress in proton-conducting oxides as electrolytes for low-temperature solid oxide fuel cells: From materials to devices. *Energy Science and Engineering*. 2021. **9**: 984–1011. https://doi.org/10.1002/ese3.886.
11. Kreuer K. D. Proton-conducting oxides. *Annual Review of Materials Research*. 2003. **33**: 333–359. https://doi.org/10.1146/annurev.matsci.33.022802.091825.
12. Dubois A., Ricote S., Braun R. J. Benchmarking the expected stack manufacturing cost of next generation, intermediate-temperature protonic ceramic fuel cells with solid oxide fuel cell technology. *Journal of Power Sources*. 2017. **369**: 65–77. https://doi.org/10.1016/j.jpowsour.2017.09.024.
13. Singh K., Kannan R., Thangadurai V. Perspective of perovskite-type oxides for proton conducting solid oxide fuel cells. *Solid State Ionics*. 2019. **339**: 114951. https://doi.org/10.1016/j.ssi.2019.04.014.
14. Hossain M. K., Chanda R., El-Denglawey A., Emrose T., Rahman M. T., Biswas M. C., Hashizume K. Recent progress in barium zirconate proton conductors for electrochemical hydrogen device applications: A review. *Ceramics International*. 2021. **47**(17): 23725–23748. https://doi.org/10.1016/j.ceramint.2021.05.167.
15. Hossain S., Abdalla A. M., Jamain S. N. B., Zaini J. H., Azad A. K. A review on proton conducting electrolytes for clean energy and intermediate temperature-solid oxide fuel cells. *Renewable and Sustainable Energy Reviews*. 2017. **79**: 750–764. https://doi.org/10.1016/j.rser.2017.05.147.
16. Irvine J., Rupp J. L. M., Liu G., Xu X., Haile S., Qian X., Snyder A., Freer R., Ekren D., Skinner S., Celikbilek O., Chen S., Tao S., Shin T. H., O'Hayre R., Huang J., Duan C., Papac M., Li S., Celorrio V., Russell A., Hayden B., Nolan H., Huang X., Wang G., Metcalfe I., Neagu D., Martín S. G. Roadmap on inorganic perovskites for energy applications. *Journal of Physics: Energy*. 2021. **3**(3): 031502. https://doi.org/10.1088/2515-7655/abff18.
17. Li J., Wang C., Wang X., Bi L. Sintering aids for proton-conducting oxides – A double-edged sword? A mini review. *Electrochemistry Communications*. 2020. **112**: 106672. https://doi.org/10.1016/j.elecom.2020.106672.
18. Fop S., McCombie K. S., Wildman E. J. High oxide ion and proton conductivity in a disordered hexagonal perovskite. *Nature Materials*. 2020. **19**: 752–757. https://doi.org/10.1038/s41563-020-0629-4.
19. Yashima M., Tsujiguchi T., Sakuda Y., Yasui Y., Zhou Y., Fujii K., Torii S., Kamiyama T., Skinner S. J. High oxide-ion conductivity through the interstitial oxygen site in $Ba_7Nb_4MoO_{20}$-based hexagonal perovskite related oxides. *Nature Communications*. 2021. **12**: 556. https://doi.org/10.1038/s41467-020-20859-w.
20. Fop S., Dawson J. A., Fortes A. D., Ritter C., McLaughlin A. C. Hydration and ionic conduction mechanisms of hexagonal perovskite derivatives. *Chemistry of Materials*. 2021. **33**(12): 4651–4660.

https://doi.org/10.1021/acs.chemmater.1c01141.
21. Gaft M., Reisfeld R., Panczer G. Modern luminescence spectroscopy of minerals and materials. Berlin: Springer, 2005. 345 p.
22. Garcia-Gonzalez E., Parras M., Gonzalez-Calbet J. M. Crystal structure of an unusual polytype: 7H-$Ba_7Nb_4MoO_{20}$. *Chemistry of Materials*. 1999. **11**(2): 433–437. https://doi.org/10.1021/cm981011i.
23. Perry D. L. Handbook of inorganic compounds. Boca Raton: CRC Press, 2011. 554 p.
24. Patterson A. L. The Scherrer formula for X-Ray particle size determination. *Physical Review*. 1939. **56**(10): 978–982. https://doi.org/10.1103/PhysRev.56.978.
25. Klung H.P., Alexander L.E. X-ray diffraction procedures: For polycrystalline and amorphous materials. New York: Wiley, 1974. 992 p.
26. Wu J., Davies R. A., Islam M. S., Haile S. M. Atomistic study of doped $BaCeO_3$: dopant site-selectivity and cation nonstoichiometry. *Chemistry of Materials*. 2005. **17**(4): 846–851. https://doi.org/10.1021/cm048763z.
27. Gdula-Kasica K., Mielewczyk-Gryn A., Lendze T., Molin S., Kusz B., Gazda M. Synthesis of acceptor-doped Ba-Ce-Zr-O perovskites. *Crystal Research and Technology*. 2010. **45**(12): 1251–1257. https://doi.org/10.1002/crat.201000380.
28. Gusak A. M. Diffusion-controlled solid state reactions in alloys, thin-films, and nanosystems. Weinheim: WILEY-VCH Verlag GmbH & Co., 2010. 475 p.
29. Tretyakov Yu. D. Solid-phase reactions. Moscow: Khimiya, 1978. 360 p. (*in Russian*).
30. Arora S. K., Trivikrama Rao G. S. Electrical conductivity of $BaMoO_4$ single crystals. *Crystal Research and Technology*. 1982. **17**(10): 1303–1305. https://doi.org/10.1002/crat.2170171023.
31. Malyi O. I., Yeung M. T., Poeppelmeier K. R., Persson C., Zunger A. Spontaneous non-stoichiometry and ordering in degenerate but gapped transparent conductors. *Matter*. 2019. **1**(1): 280–294. https://doi.org/10.1016/j.matt.2019.05.014.
32. Unti L. F. K., Grzebielucka E. C., Chinelatto A. S. A., Mather G. C., Chinelatto A. L. Synthesis and electrical characterization of $Ba_5Nb_4O_{15}$ and $Ba_5Nb_{3.9}M_{0.1}O_{(15-\delta)}$ (M = Ti, Zr) hexagonal perovskites. *Ceramics International*. 2019. **45**(4): 5087–5092. https://doi.org/10.1016/j.ceramint.2018.11.211.
33. Black D. L., McQuay M. Q., Bonin M. P. Laser-based techniques for particle-size measurement: A review of sizing methods and their industrial applications. *Progress in Energy and Combustion Science*. 1996. **22**(3): 267–306. https://doi.org/10.1016/S0360-1285(96)00008-1.
34. Averardi A., Cola C., Zeltmann S. E., Gupta N. Effect of particle size distribution on the packing of powder beds: A critical discussion relevant to additive manufacturing. *Materials today communications*. 2020. **24**: 100964. https://doi.org/10.1016/j.mtcomm.2020.100964.
35. Yeh T.-S., Sacks M. D. Effect of particle size distribution on the sintering of alumina. *Journal of the American Ceramic Society*. 1988. **71**(12): C-484–C-487. https://doi.org/10.1111/j.1151-2916.1988.tb05812.x.
36. Bai Y., Wagner G., Williams C. B. Effect of particle size distribution on powder packing and sintering in binder jetting additive manufacturing of metals. *Journal of Manufacturing Science and Engineering*. 2017. **139**(8): 081019. https://doi.org/10.1115/1.4036640.
37. Shiau F.-S., Fang T.-T., Leu T.-H. Effect of particle-size distribution on the microstructural evolution in the intermediate stage of sintering. *Journal of the American Ceramic Society*. 1997. **80**(2): 286–290. https://doi.org/10.1111/j.1151-2916.1997.tb02828.x.
38. Olsson E., Larsson P.-L. On the effect of particle size distribution in cold powder compaction. *Journal of Applied Mechanics*. 2012. **79**(5): 051017. https://doi.org/10.1115/1.4006382.
39. Dirksen J. A., Ring T. A. Fundamentals of crystallization: Kinetic effects on particle size distributions and morphology. *Chemical Engineering Science*. 1991. **46**(10): 2389–2427. https://doi.org/10.1016/0009-2509(91)80035-W.

Стаття надійшла 16.04.2022.

UCD: 539.216:546.817:548.736.442.6 doi: 10.33609/2708-129X.88.04.2022.79-93

INFLUENCE OF THE SOLVENT AND THE RATIO OF STARTING REAGENTS ON THE PROPERTIES OF ORGANIC-INORGANIC PEROVSKITE $MAPbI_3$

Torchyniuk P.V.[1], V'yunov O.I.*[1], Vlasiuk V.M.[2], Kostylyov V.P.[2], Belous A.G.[1]

[1]V.I. Vernadsky Institute of General and Inorganic Chemistry of National Academy of Sciences of Ukraine, Acad. Palladina Ave., 32/34, Kyiv 03142, Ukraine
[2]V.E. Lashkarev Institute of Semiconductor Physics of National Academy of Sciences of Ukraine, pr. Nauki 41, Kyiv 03028, Ukraine
** e-mail: vyunov@ionc.kiev.ua*

The peculiarities of formation and properties of organic-inorganic $MAPbI_3$ perovskite films, obtained from solutions with different ratios of starting reagents (PbI_2:MAI = 1:1,1:2, and 1:3), in the DMF and DMSO solvents, studied. As the PbI_2:MAI ratio increases, the temperature of the formation of a single-phase $MAPbI_3$ perovskite film also increases. The slight changes in the structural and electrophysical characteristics for perovskite films obtained at the different ratios of PbI_2:MAI in DMF and DMSO were found. These changes are related to the solvent that is included in the crystalline structure of perovskite. In the same ratios of starting reagents, DMF is included in the structure of perovskite in a greater amount than DMSO.

Keywords: organic-inorganic perovskite, phase transformations, structural parameters, electrophysical characteristics.

INTRODUCTION. The global energy crisis is one of the greatest challenges facing humanity. It is necessary to develop new technologies for the successful use of energy from renewable sources due to the reduced availability of fossil fuels. Solar energy is a rich, freely available source and promising replacement for non-renewable fossil fuels.

The solar cells based on organic-inorganic perovskites have attracted the attention of scientists according to a significant increase in efficiency to 25.2%, low cost, and ease of production. [1–2]. This effect was achieved by improving the design of solar cells, adding new conductive layers (of n- and p-type), and improving the quality of the perovskite films. Organic-inorganic perovskites combine the advantages of organic and inorganic semiconductors: high optical absorption, high mobility of charge carriers [3], and regulated bandgap [4].

Photoactive halide perovskites usually exhibit a three-dimensional crystal structure with the characteristic chemical formula ABX_3, where A is a monovalent cation of methylammonium ($CH_3NH_3^+$), formamidinium ($HC(NH_2)_2^+$), cesium (Cs^+) or rubidium (Rb^+),

and B is a divalent metal cation Pb^{2+} or Sn^{2+}, and X is a halide anion (Cl^-, Br^- or I^-) [5, 6].

Achieving the high photoelectric characteristics of organic-inorganic perovskite depends on the nucleation and growth of crystal processes. As a result of the process control, it is possible to obtain a smooth and compact film of perovskite. External factors (temperature, moisture, oxygen), as well as solvent, methods of obtaining films, and annealing can significantly affect the structural and physical properties of organic-inorganic perovskite. It is known that solvents (DMF, DMSO, γ-butyrolactone (GBL), NMP) [7, 8] were used for the synthesis of perovskites can affect the properties of films.

Changes in the synthesis conditions (ratio of starting reagents and solvent) may affect the properties of perovskites. It was shown that the ratio of starting reagents PbI_2:MAI (CH_3NH_3I) affects electrophysical characteristics, particularly, the bandgap [9]. Solvent replacement also affects the properties of organic-inorganic perovskite. An increase in the stability of films to moisture and the mobility of charge carriers detected by using dimethyl sulfoxide instead of dimethylformamide during the synthesis of perovskite [10].

The method of obtaining perovskites is a key factor in achieving high characteristics (surface coverage, crystallinity, thickness, and quality of films responsible for the morphological and transport properties of perovskite). Several methods can be used to obtain films of organic-inorganic perovskites. The most common methods of them are one-step and two-step deposition, spin-coating, the method of rapid deposition crystallization, and thermal evaporation.

It is known that organic-inorganic perovskites are unstable materials that can degrade and decompose into various components under the influence of external factors. Finding ways to increase the stability of perovskites is an urgent task, as its solution will allow them to be used in the large-scale creation of solar cells. Nowadays, the best laboratory samples of elements based on perovskite demonstrate high efficiency and a low cost of their production. However, they have relatively low stability, although some solar cells show stable operation throughout the year [11, 12].

This work aims to study the peculiarities of perovskite formation, and structural and electrophysical characteristics of organic-inorganic $MAPbI_3$ perovskite films depending on the solvent and the ratio of starting reagents.

EXPERIMENT AND DISCUSSION OF THE RESULTS.

Materials. Lead iodide (PbI_2) and methylammonium iodide MAI (CH_3NH_3I) were used as starting reagents for the synthesis of organic-inorganic perovskites. To stabilize the structure of perovskite, partial replacement of iodine with chlorine was carried out by adding chemically pure methylammonium chloride MACl (CH_3NH_3Cl). Dried chemically pure dimethylformamide (DMF) and dimethyl sulfoxide (DMSO) were used as solvents.

The starting reagents PbI_2 and MAI in the ratios 1:1, 1:2, 1:3 were dissolved in DMF and DMSO and stirred at 70 °C for 1 hour to obtain $MAPbI_3$ ($CH_3NH_3PbI_3$) films. The formation of crystalline $MAPbI_3$ films was performed in a dry box. A pre-prepared clear solution was deposited on cleaned glass substrates by spin-coating at a speed of 1200 rpm for 30 s. The heat treatment of the films was performed on a preheated stove at temperatures from 20 to 205 °C for 15 minutes.

The identifications of the phase composition of films and calculations of the parameters of the unit cell were performed by X-ray diffractometry (XRD) using a DRON-4-07 (CuKα radiation and Ni filter, 40 kV, 18 mA) at 2Θ = 5–50°, a step of 0.04° and a count time of 4 s.

SiO_2 (angle standard 2Θ) and Al_2O_3 (certified intensity standard) were used as standards [13]. The parameters of the unit cell and the coordinates of atoms were determined using the FullProf program developed by Juan Rodríguez-Carvajal, Laboratoire Léon Brillouin (France) [14].

Peculiarities of phase transformations in the formation of organic-inorganic perovskite $MAPbI_3$ in DMF, DMSO solvents. Plots of the percentage of crystalline phases versus the film treatment temperature were constructed based on diffractograms of perovskite films obtained at different ratios of starting reagents in the DMF solvent (Fig. 1).

Figure 1 shows that the temperature ranges of the existence of intermediate compounds $(MA)_2(DMF)_2Pb_3I_8$, $(MA)_2(DMF)_xPbI_4$, $(MA)_3(DMF)PbI_5$, $(MA)_2(DMF)_2Pb_2I_6$ and organic-inorganic perovskite $MAPbI_3$ in the film can be determined depending on the ratio of reagents. The structure of $MAPbI_3$ perovskite begins to form at a temperature of 20-25 °C, regardless of the ratio of starting reagents. The formation of organic-inorganic perovskite occurs by the formation and decomposition of various amounts of intermediate compounds. At the ratio of starting reagents PbI_2:MAI – 1:1, there are three intermediate compounds, and at 1:2, 1:3 four and two intermediate compounds, respectively. In a detailed analysis of the percentage of crystalline phases and diffractograms, formation reactions of $MAPbI_3$ perovskite were obtained at the PbI_2:MAI = 1:1 ratio in DMF (Table 1).

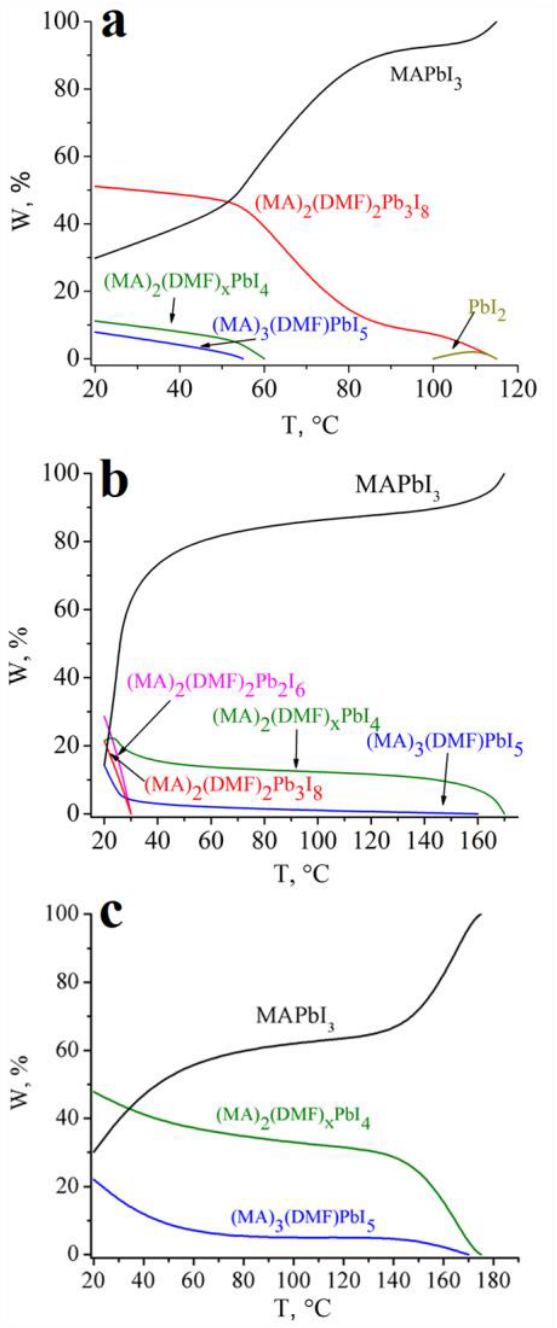

Fig. 1. The dependence of the percentage of crystalline phases on the treatment temperature of the film obtained at different ratios PbI_2:MAI in DMF: a) 1:1; (b) 1:2; (c) 1:3.

Table 1

Phase transformations in the formation of $MAPbI_3$ perovskite at a ratio of starting reagents of 1:1 in DMF.

Reagents	Temperature	Reaction products
$13PbI_2 + 13MAI$ **(1:1 in DMF)**	20–45 °C	$(MA)_3(DMF)PbI_5 + (MA)_2(DMF)_xPbI_4 + 2MAPbI_3 + 3(MA)_2(DMF)_2Pb_3I_8$
	50 °C	$0.5(MA)_3(DMF)PbI_5 + 0.75(MA)_2(DMF)_xPbI_4 + 1.25MAI + 3(MA)_2(DMF)_2Pb_3I_8 + 2.75MAPbI_3$
	55°C	$0.5(MA)_2(DMF)_xPbI_4 + 2.5(MA)_2(DMF)_2Pb_3I_8 + 2MAI + 5MAPbI_3$
	> 55–105 °C	$(MA)_2(DMF)_2Pb_3I_8 + 10MAPbI_3 + MAI$
	>105–110 °C	$0.5(MA)_2(DMF)_2Pb_3I_8 + 11MAPbI_3 + MAI + 0.5PbI_2$
	> 110–115 °C	$13\ MAPbI_3$
$13PbI_2 + 13MAI$	20–45° C	$(MA)_3(DMF)PbI_5 + (MA)_2(DMF)_xPbI_4 + 2MAPbI_3 + 3(MA)_2(DMF)_2Pb_3I_8$
$(MA)_3(DMF)PbI_5$	50 °C	$0.5(MA)_3(DMF)PbI_5 + 0.5(MA)_2(DMF)_xPbI_4 + 0.5MAI + (0.5\text{-}0.5x)DMF$
$2(MA)_2(DMF)_xPbI_4$		$0.25(MA)_2(DMF)_xPbI_4 + 0.75MAPbI_3 + 0.75MAI + 1.5xDMF$
$0.5(MA)_3(DMF)PbI_5$	55 °C	$0.5(MA)_2(DMF)_xPbI_4 + 0.5MAI + (0.5\text{-}0.5x)DMF$
$0.75(MA)_2(DMF)_xPbI_4$		$0.75MAPbI_3 + 0.75MAI + 0.75xDMF$
$3(MA)_2(DMF)_2Pb_3I_8 + 0.5MAI$		$2.5(MA)_2(DMF)_2Pb_3I_8 + 1{,}5MAPbI_3 + 2DMF$
$0.5(MA)_2(DMF)_xPbI_4$	>55-105 °C	$0.5MAPbI_3 + 0.5MAI + 0.5xDMF$
$2.5(MA)_2(DMF)_2Pb_3I_8 + 0.5MAI$		$(MA)_2(DMF)_2Pb_3I_8 + 4.5MAPbI_3 + 3DMF$
$(MA)_2(DMF)_2Pb_3I_8$	> 105–110 °C	$0.5(MA)_2(DMF)_2Pb_3I_8 + MAPbI_3 + 0.5PbI_2 + DMF$
$0.5(MA)_2(DMF)_2Pb_3I_8 + 0.5MAI$	> 110–115 °C	$1{,}5MAPbI_3 + DMF$
$0.5PbI_2 + 0.5MAI$		$0.5MAPbI_3$

At a ratio of 1:1, a single-phase perovskite film is formed at 115 °C. There is a gradual decomposition of the intermediate compound $(MA)_3(DMF)PbI_5$ into $(MA)_2(DMF)_xPbI_4$, which completely decomposes into $MAPbI_3$ at T> 55 °C. The compound $(MA)_2(DMF)_2Pb_3I_8$ is completely decomposed into $MAPbI_3$ perovskite at T> 110 °C.

When the ratio of starting reagents is 1:2 in DMF, a single-phase $MAPbI_3$ perovskite film is formed at 170 °C (Table 2). At this ratio, similar transformations of the intermediate compounds $(MA)_3(DMF)PbI_5$, $(MA)_2(DMF)_xPbI_4$, $(MA)_2(DMF)_2Pb_3I_8$ are observed for the ratio 1:1, but the temperatures of transformations are greatly different. In addition, the conversion of the intermediate $(MA)_2(DMF)_2Pb_2I_6$ to $MAPbI_3$ is observed in this system at T> 30 °C.

Table 2

Phase transformations in the formation of $MAPbI_3$ perovskite at a ratio of starting reagents of 1:2 in DMF.

Reagents	Temperature	Reaction products
$24PbI_2 + 48MAI$ **(1:2 in DMF)**	20 °C	$4(MA)_2(DMF)_2Pb_2I_6 + 2(MA)_3(DMF)PbI_5 + 20MAI + 3(MA)_2(DMF)_xPbI_4 + 3(MA)_2(DMF)_2Pb_3I_8 + 2MAPbI_3$
	25 °C	$3(MA)_2(DMF)_2Pb_2I_6 + (MA)_3(DMF)PbI_5 + 20MAI + 4(MA)_2(DMF)_xPbI_4 + 2(MA)_2(DMF)_2Pb_3I_8 + 7MAPbI_3$
	>30–130 °C	$3(MA)_2(DMF)_xPbI_4 + 0.5(MA)_3(DMF)PbI_5 + 20MAI + 20.5MAPbI_3$
	>130–160 °C	$2.5(MA)_2(DMF)_xPbI_4 + 21.5MAPbI_3 + 21.5MAI$
	>160–170 °C	$24MAPbI_3 + 24MAI$
$24PbI_2 + 48MAI$	20 °C	$4(MA)_2(DMF)_2Pb_2I_6 + 2(MA)_3(DMF)PbI_5 + 3(MA)_2(DMF)_xPbI_4 + 3(MA)_2(DMF)_2Pb_3I_8 + 2MAPbI_3 + 20MAI$
$4(MA)_2(DMF)_2Pb_2I_6$	25 °C	$3(MA)_2(DMF)_2Pb_2I_6 + 2MAPbI_3 + 2DMF$
$2(MA)_3(DMF)PbI_5$		$(MA)_3(DMF)PbI_5 + (MA)_2(DMF)_xPbI_4 + MAI + (1-x)DMF$
$3(MA)_2(DMF)_2Pb_3I_8 + MAI$		$2(MA)_2(DMF)_2Pb_3I_8 + 3MAPbI_3 + 2DMF$
$3(MA)_2(DMF)_2Pb_2I_6$	>30–130 °C	$6MAPbI_3 + 6DMF$
$(MA)_3(DMF)PbI_5$		$0.5(MA)_3(DMF)PbI_5 + 0.5(MA)_2(DMF)_xPbI_4 + 0.5MAI + (0.5-0.5x)DMF$
$4(MA)_2(DMF)_xPbI_4$		$2.5(MA)_2(DMF)_xPbI_4 + 1.5MAPbI_3 + 1.5MAI + 1.5xDMF$
$2(MA)_2(DMF)_2Pb_3I_8 + 2MAI$		$6MAPbI_3 + 4DMF$
$3(MA)_2(DMF)_xPbI_4$	>130–160 °C	$2(MA)_2(DMF)_xPbI_4 + MAPbI_3 + MAI + xDMF$
$0.5(MA)_3(DMF)PbI_5$		$0.5(MA)_2(DMF)_xPbI_4 + 0.5MAI + (0.5-0.5x)DMF$
$2.5(MA)_2(DMF)_xPbI_4$	>160–170 °C	$2.5MAPbI_3 + 2.5MAI + 2.5xDMF$

Table 3

Phase transformations in the formation of $MAPbI_3$ perovskite at a ratio of starting reagents of 1:3 in DMF.

Reagents	Temperature	Reaction products
$9PbI_2 + 27MAI$ **(1:3 in DMF)**	20–150 °C	$4(MA)_2(DMF)_xPbI_4 + (MA)_3(DMF)PbI_5 + 4MAPbI_3 + 12MAI$
	>150–170 °C	$2(MA)_2(DMF)_xPbI_4 + 7MAPbI_3 + 16MAI$
	>170–175 °C	$9MAPbI_3 + 18MAI$
$9PbI_2 + 27MAI$	20–150 °C	$4(MA)_2(DMF)_xPbI_4 + (MA)_3(DMF)PbI_5 + 4MAPbI_3 + 12MAI$
$4(MA)_2(DMF)_xPbI_4 + (MA)_3(DMF)PbI_5$	>150–170 °C	$2(MA)_2(DMF)_xPbI_4 + 4MAI + 3MAPbI_3 + (2x+1)DMF$
$2(MA)_2(DMF)_xPbI_4$	>170–175 °C	$2MAPbI_3 + 2MAI + 2xDMF$

At the ratio PbI_2:MAI = 1:3, the formation of a single-phase $MAPbI_3$ perovskite film occurs at 175 °C (Table 3).

There is a gradual decomposition of the intermediate compound $(MA)_3(DMF)PbI_5$ into 4MAI and $(MA)_2(DMF)_xPbI_4$; the latter completely decomposes into $MAPbI_3$ at T> 170 °C.

Thus, the ratio of starting reagents in DMF significantly affects the number of intermediate compounds that are formed during the synthesis. As the ratio of reagents increases, the temperature of formation of single-phase $MAPbI_3$ perovskite film increases. The $MAPbI_3$ phase is present in the film after heat treatment at 20 °C in amounts of 15-30 wt. %. However, at higher temperatures of 40-60 °C, the intermediate phases begin to decompose, and in this temperature range, the transformation of the intermediate phases into perovskite is not completed.

For the perovskite films synthesized at different ratios of starting reagents in the DMSO solvent, plots of the crystalline phase content versus the film treatment temperature were constructed (Fig. 2).

Figure 2 shows that the structure of $MAPbI_3$ perovskite begins to form at 60 °C for the ratios 1:1, 1:2, and at 70 °C for the ratio 1:3. At a ratio of 1:1, the perovskite film obtained at T> 160 °C begins to degrade, which is accompanied by a decrease in the percentage of perovskite $MAPbI_3$ and an increase in the percentage of the intermediate PbI_2·DMSO (Fig. 2a). At this ratio of starting reagents, a single-phase film is not formed. At a ratio of 1:2, 1:3, intermediate compounds completely decompose and a single-phase $MAPbI_3$ film is formed at 190 and 205 °C, respectively.

The quantitative content of the phases $(MA)_2(DMSO)_2Pb_3I_8$, $(MA)_2(DMSO)_xPbI_4$, PbI_2·DMSO, PbI_2·2DMSO, and organic-inorganic perovskite $MAPbI_3$ in the film depends on the ratio of reagents and treatment temperature.

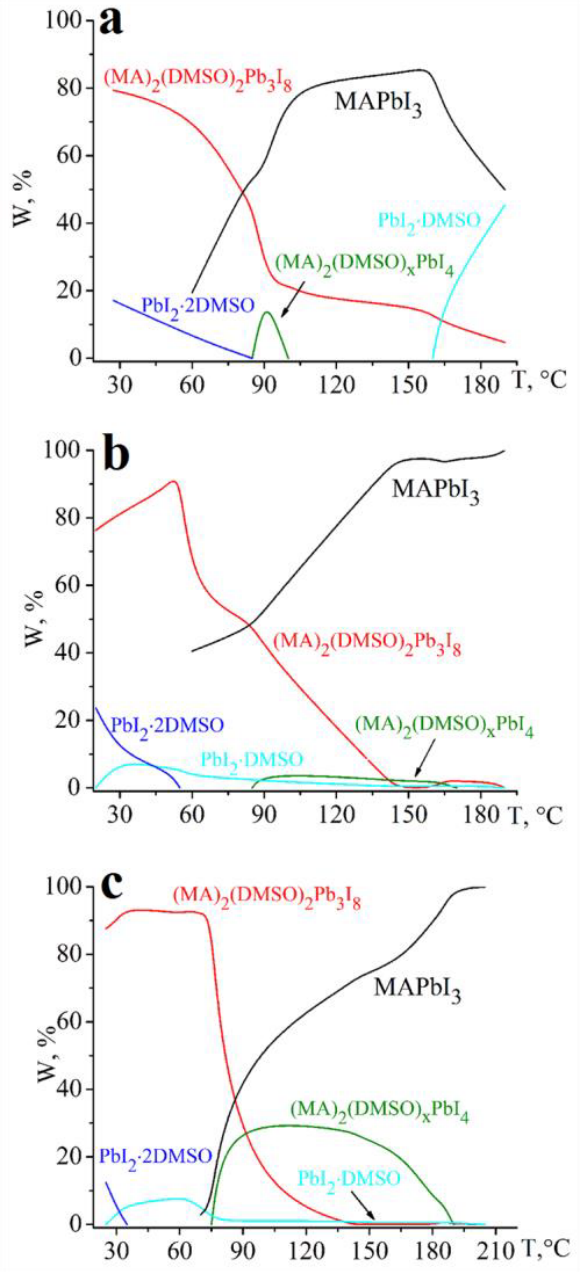

Fig. 2. The dependence of the percentage of crystalline phases on the treatment temperature of the film obtained at different ratios PbI_2:MAI in DMSO: (a) 1:1; (b) 1:2; (c) 1:3.

Table 4

Phase transformations in the formation of $MAPbI_3$ perovskite at a ratio of starting reagents of 1:1 in DMSO.

Reagents	Temperature	Reaction products
$10PbI_2$ + 10MAI **(1:1 in DMSO)**	20–50 °C	$3(MA)_2(DMSO)_2Pb_3I_8 + PbI_2 \cdot 2DMSO + 4MAI$
	60–85 °C	$2(MA)_2(DMSO)_2Pb_3I_8 + PbI_2 \cdot 2DMSO + 3MAPbI_3 + 3MAI$
	90 °C	$(MA)_2(DMSO)_2Pb_3I_8 + (MA)_2(DMSO)_xPbI_4 + 6MAPbI_3$
	> 90–100 °C	$(MA)_2(DMSO)_2Pb_3I_8 + 7MAPbI_3 + MAI$
	110 °C	$0.5(MA)_2(DMSO)_2Pb_3I_8 + 0.5PbI_2 \cdot 2DMSO + MAI + 8MAPbI_3$
	> 110–160 °C	$0.5(MA)_2(DMSO)_2Pb_3I_8 + 8.5MAPbI_3 + 0.5MAI$
	> 165–180 °C	$0.25(MA)_2(DMSO)_2Pb_3I_8 + 9MAPbI_3 + 0.5MAI + 0.25PbI_2 \cdot DMSO$
	190 °C	$0.25(MA)_2(DMSO)_2Pb_3I_8 + 7MAPbI_3 + 2.25PbI_2 \cdot DMSO + 2.5MAI$
$10PbI_2$ + 10MAI	20–50 °C	$3(MA)_2(DMSO)_2Pb_3I_8 + PbI_2 \cdot 2DMSO + 4MAI$
$3(MA)_2(DMSO)_2Pb_3I_8$ + MAI	60–85 °C	$2(MA)_2(DMSO)_2Pb_3I_8 + 3\ MAPbI_3 +$ 2DMSO
$2(MA)_2(DMSO)_2Pb_3I_8$ + 2MAI	90 °C	$(MA)_2(DMSO)_2Pb_3I_8 + (2\text{-}x)DMSO + (MA)_2(DMSO)_xPbI_4 + 2MAPbI_3$
$PbI_2 \cdot 2DMSO$ + MAI		$MAPbI_3 + 2DMSO$
$(MA)_2(DMSO)_xPbI_4$	> 90–100 °C	$MAPbI_3 + MAI + xDMSO$
$(MA)_2(DMSO)_2Pb_3I_8$	110 °C	$0.5(MA)_2(DMSO)_2Pb_3I_8 + MAPbI_3 + 0.5PbI_2 \cdot 2DMSO$
$0.5PbI_2 \cdot 2DMSO$ + MAI	> 110–160 °C	$0.5\ MAPbI_3 + 0.5\ MAI + DMSO$
$0.5(MA)_2(DMSO)_2Pb_3I_8$ + 0.5MAI	> 165–180 °C	$0.25(MA)_2(DMSO)_2Pb_3I_8 + 0.5MAPbI_3 + 0.25PbI_2 \cdot DMSO + 0.25DMSO$
$0.25PbI_2 \cdot DMSO$ + $2MAPbI_3$	190 °C	$2\ MAI + 2.25PbI_2 \cdot DMSO$

In a detailed analysis of diffractograms and the phase content of the film, formation reactions of $MAPbI_3$ perovskite at the ratio PbI_2:MAI = 1:1 in DMSO were obtained (Table 4).

At a ratio of starting reagents of 1:1 in DMSO, the formation of organic-inorganic perovskite $MAPbI_3$ occurs through the formation and decomposition of 4 intermediates $(MA)_2(DMSO)_2Pb_3I_8$, $(MA)_2(DMSO)_xPbI_4$, $PbI_2 \cdot DMSO$, $PbI_2 \cdot 2DMSO$. It was shown that the intermediate compound $(MA)_2(DMSO)_2Pb_3I_8$ at 90 °C decomposes into the compound $(MA)_2(DMSO)_xPbI_4$, from which perovskite formation takes place.

At a ratio of 1:2 in DMSO, a single-phase perovskite film is formed at 190 °C (Table 5). In this case, the same 4 intermediate compounds are also formed, which are formed at a ratio of 1:1.

Table 5

Phase transformations in the formation of $MAPbI_3$ perovskite at a ratio of starting reagents of 1:2 in DMSO.

Reagents	Temperature	Reaction products
$8PbI_2$ + 16MAI **(1:2 in DMSO)**	20–55 °C	$3(MA)_2(DMSO)_2Pb_3I_8$ + PbI_2·2DMSO + PbI_2· DMSO + 12MAI
	60–85 °C	$2(MA)_2(DMSO)_2Pb_3I_8$ + PbI_2·DMSO + $MAPbI_3$ + 11MAI
	90–140 °C	$(MA)_2(DMSO)_2Pb_3I_8$ + PbI_2·DMSO + $3MAPbI_3$ + 9MAI + $(MA)_2(DMSO)_xPbI_4$
	>140–160 °C	PbI_2·DMSO + $2(MA)_2(DMSO)_xPbI_4$ + $5MAPbI_3$ + 7MAI
	165 °C	$0.5(MA)_2(DMSO)_2Pb_3I_8$ + $0.5PbI_2$·DMSO + $5MAPbI_3$ + $(MA)_2(DMSO)_xPbI_4$ + 8MAI
	>165–185 °C	$0.75(MA)_2(DMSO)_2Pb_3I_8$ + $5.25MAPbI_3$ + $0.5PbI_2$·DMSO + 9.25MAI
	190 °C	$8MAPbI_3$ + 8MAI
$8PbI_2$ + 16MAI	20–55 °C	$2(MA)_2(DMSO)_2Pb_3I_8$ + PbI_2·2DMSO + PbI_2·DMSO + 12MAI
PbI_2· 2DMSO	60–85 °C	PbI_2·DMSO + DMSO
PbI_2· DMSO + MAI		$MAPbI_3$ + DMSO
$2(MA)_2(DMSO)_2Pb_3I_8$ + 2MAI	90–140 °C	$(MA)_2(DMSO)_2Pb_3I_8$ + $2MAPbI_3$ + (2-x)DMSO + $(MA)_2(DMSO)_xPbI_4$
$(MA)_2(DMSO)_2Pb_3I_8$ + 2MAI	>140–160 °C	$(MA)_2(DMSO)_xPbI_4$ + $2MAPbI_3$ + (2-x)DMSO
$2(MA)_2(DMSO)_xPbI_4$ + PbI_2· DMSO	165 °C	$0.5(MA)_2(DMSO)_2Pb_3I_8$ + $0.5PbI_2$·DMSO + $(MA)_2(DMSO)_xPbI_4$ + MAI + (x-0.5)DMSO
$0.5(MA)_2(DMSO)_2Pb_3I_8$ + $(MA)_2(DMSO)_xPbI_4$	>165-185 °C	$0.75(MA)_2(DMSO)_2Pb_3I_8$ + $0.25MAPbI_3$ + 1.25MAI + (x-0.5)DMSO
$0.75(MA)_2(DMSO)_2Pb_3I_8$ + 1.25MAI	190 °C	$2.25\ MAPbI_3$ + 1.5DMSO + 0.5MAI
$0.5PbI_2$· DMSO + 0.5MAI		$0.5MAPbI_3$ + 0.5DMSO

At a ratio of 1:2, interconversion of compounds $(MA)_2(DMSO)_2Pb_3I_8 \leftrightarrow (MA)_2(DMSO)_xPbI_4$ is observed. At low temperatures (90-160 °C) the preceding reaction proceeds in the forward direction with the formation of $(MA)_2(DMSO)_xPbI_4$, while a part of $(MA)_2(DMSO)_2Pb_3I_8$ is converted into $MAPbI_3$. At T > 165-185 °C, the reaction proceeds in the reverse direction, while a part of $(MA)_2(DMSO)_xPbI_4$ is converted into $MAPbI_3$. A conversion of the compound PbI_2·2DMSO to PbI_2·DMSO is also observed, which in interaction with MAI forms perovskite $MAPbI_3$.

When increasing the ratio of starting reagents to 1:3, a single-phase perovskite film is formed at 205 °C (Table 6). The formation of

perovskite occurs through the formation and decomposition of 4 intermediate compounds. At a ratio of 1:3, interconversion of compounds $(MA)_2(DMSO)_2Pb_3I_8 \leftrightarrow (MA)_2(DMSO)_xPbI_4$ is also observed, but in a wider temperature range. There is also a conversion of the compound $PbI_2 \cdot 2DMSO$ to $PbI_2 \cdot DMSO$, which when interacting with MAI forms perovskite $MAPbI_3$ as for the ratio 1:2.

Table 6

Phase transformations in the formation of $MAPbI_3$ perovskite at a ratio of starting reagents of 1:3 in DMSO.

Reagents	Temperature	Reaction products
$8PbI_2 + 24MAI$ **(1:3 in DMSO)**	20–30 °C	$2(MA)_2(DMSO)_2Pb_3I_8 + PbI_2 \cdot 2DMSO + PbI_2 \cdot DMSO + 20MAI$
	>30–65 °C	$2(MA)_2(DMSO)_2Pb_3I_8 + 2PbI_2 \cdot DMSO + 20MAI$
	70–75 °C	$2(MA)_2(DMSO)_2Pb_3I_8 + PbI_2 \cdot DMSO + MAPbI_3 + 19MAI$
	80–140 °C	$(MA)_2(DMSO)_2Pb_3I_8 + PbI_2 \cdot DMSO + 3MAPbI_3 + (MA)_2(DMSO)_xPbI_4 + 17MAI$
	>140–160 °C	$3(MA)_2(DMSO)_xPbI_4 + 5MAPbI_3 + 13MAI$
	>165–185 °C	$0.5(MA)_2(DMSO)_2Pb_3I_8 + 0.5(MA)_2(DMSO)_xPbI_4 + 6MAPbI_3 + 16MAI$
	>185–200 °C	$PbI_2 \cdot DMSO + 7MAPbI_3 + 17MAI$
	205 °C	$8MAPbI_3 + 16MAI$
$8PbI_2 + 24MAI$	20–30 °C	$2(MA)_2(DMSO)_2Pb_3I_8 + PbI_2 \cdot 2DMSO + PbI_2 \cdot DMSO + 20MAI$
$PbI_2 \cdot 2DMSO + PbI_2 \cdot DMSO$	>30–65 °C	$2PbI_2 \cdot DMSO + DMSO$
$2PbI_2 \cdot DMSO + MAI$	70–75 °C	$PbI_2 \cdot DMSO + MAPbI_3 + DMSO$
$2(MA)_2(DMSO)_2Pb_3I_8 + 2MAI$	80–140 °C	$(MA)_2(DMSO)_2Pb_3I_8 + 2MAPbI_3 + (2-x)DMSO + (MA)_2(DMSO)_xPbI_4$
$(MA)_2(DMSO)_2Pb_3I_8 + 3MAI$	>140–165 °C	$MAPbI_3 + 2(MA)_2(DMSO)_xPbI_4 + (2-2x)\ DMSO$
$PbI_2 \cdot DMSO + MAI$		$MAPbI_3 + DMSO$
$3(MA)_2(DMSO)_xPbI_4$	>165-185 °C	$0.5(MA)_2(DMSO)_2Pb_3I_8 + MAPbI_3 + 3MAI + 0.5(MA)_2(DMSO)_xPbI_4 + (2.5x-1)\ DMSO$
$0.5(MA)_2(DMSO)_2Pb_3I_8 + 0.5(MA)_2(DMSO)_xPbI_4$	>185-200 °C	$PbI_2 \cdot DMSO + MAPbI_3 + MAI + 0.5xDMSO$
$PbI_2 \cdot DMSO + MAI$	205 °C	$MAPbI_3 + DMSO$

Thus, regardless of the ratio of starting reagents in DMSO, the formation of $MAPbI_3$ perovskite occurs through the formation of 4 intermediate compounds. When the ratio of reagents increases, the temperature of formation of single-phase $MAPbI_3$ film increases.

Crystallographic and electrophysical characteristics of organic-inorganic perovskites $MAPbI_3$, obtained at different ratios PbI_2:MAI in DMF, and DMSO. The calculation of the unit cell parameters of organic-inorganic $MAPbI_3$ perovskite films was performed by the Rietveld full-profile analysis method using X-ray diffraction patterns (Fig. 3).

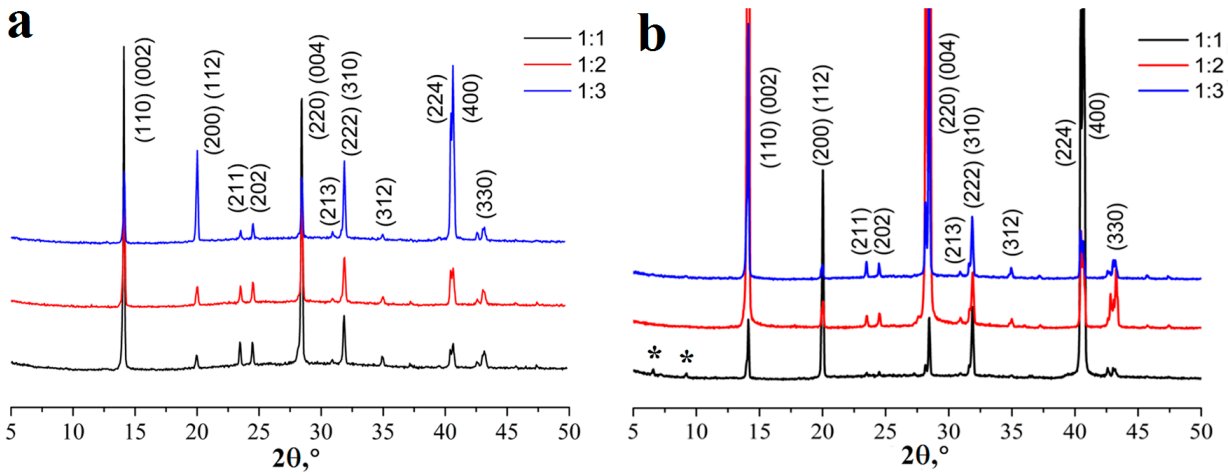

Fig. 3. Experimental X-ray diffraction patterns of samples of $MAPbI_3$ films obtained at different ratios of starting reagents in the DMSO solvent. The Miller indices are given in parentheses. * – $(MA)_2(DMSO)_2Pb_3I_8$.

It was found that depending on the ratio of starting reagents and solvent, there are slight changes in the volume of the cell for perovskite films (Table 7). The changes in the unit cell volume are associated with a small amount of the solvent that is part of the crystalline structure of perovskite. It was proved that the solvent DMSO can replace the cation MA^+ in the structure of organic-inorganic perovskite $MAPbI_3$ [15]. The radius of DMSO and DMF molecules are 3.05 Å and 3.13 Å, respectively [16], and the radius of the cation MA^+ is 2.17 Å [17]. Since DMF and DMSO molecules are close in size, it can be assumed that DMF enters into the crystal structure, creating deformations. To test this assumption, we will calculate the changes in volume and solvent concentration.

From literature, it is known that the volume of the unit cell for perovskite is $V_{perovskite}$ = 990 Å^3 [18], or $V_{perovskite}/Z = 990/4 = 247.5$ Å^3. Table 7 shows that the experimental values of unit cell volume are slightly larger than the theoretical value of unit cell volume of 990 Å^3.

Table 7

Structural parameters of organic-inorganic perovskites $MAPbI_3$, obtained at different ratios PbI_2:MAI (1:1, 1:2, 1:3) in the DMF and DMSO solvents.

Parameters	DMF			DMSO		
	1:1	1:2	1:3	1:1	1:2	1:3
V, Å^3	994.5(3)	998.6(5)	997.5(4)	991.3(1)	994.7(4)	994.5(2)
Deposition temperature	115 °C	170 °C	175 °C	150 °C	190 °C	205 °C

The calculation of the amount of solvent in the structure of perovskite was performed according to formula (1) using the unit cell volumes of the starting reagents, and perovskite, as well as the volumes of DMF, DMSO solvent molecules, and methylammonium cation MA^+:

$$\frac{V_{perovskite}}{Z_1} = \frac{V_{(PbI_2)}}{Z_2} + \frac{V_{(MAI)}}{Z_3} + (V_{solvent} - V_{(MA^+)}) \cdot x\,, \quad (1)$$

where Z_1, Z_2, and Z_3 are the formula unit for perovskite, PbI_2, and MAI, respectively, x is the amount of solvent included in the structure of perovskite, $V(PbI_2)$ is the unit cell volume of PbI_2, V(MAI) is the unit cell volume of MAI, $V_{solvent}$ is the volume of the solvent molecule, V (MA^+) is the volume of the methylammonium cation MA^+. Taking into account the values of the volumes of compounds and their formula units, we obtain $V(PbI_2)/Z_2 = 125.69/1 = 125.69$ Å^3, $V(MAI)/Z_3 = 235.93/2 = 117.965$ Å^3,

The calculation of the volume of the solvent ($V_{solvent}$) was performed according to formula (2) under the assumption that the solvent molecule has a spherical shape [18].

$$V = \frac{4}{3}\pi R^3\,, \quad (2)$$

where R is the radius of the solvent molecule. A similar volume calculation was performed for the MA^+ cation. The volume of the DMF and DMSO solvents is $V_{(DMF)} = 128.4$ Å^3, and $V_{(DMSO)} = 118.8$ Å^3, respectively. The volume of the cation MA^+ is V (MA^+) = 42.8 Å^3.

The replacement of a smaller MA^+ cation with a larger molecule of DMF or DMSO leads to minor changes in structural and electrophysical characteristics, which is confirmed by the following calculations.

The solvent content of the structure (x) was determined from formula (3), which was derived from formula (1):

$$x = \frac{\frac{V_{perovskite}}{Z_1} - \frac{V_{(PbI_2)}}{Z_2} - \frac{V_{(MAI)}}{Z_3}}{V_{solvent} - V_{(MA^+)}}\,. \quad (3)$$

The results of the calculations are summarized in table 8.

Table 8

Determination of the amount of solvent in the structure of perovskite depending on the ratios of starting reagents PbI_2:MAI in the DMF, DMSO solvent.

PbI_2:MAI	$V_{perovskite}$. Å^3	Z_1	$V_{perovskite}/Z_1$. Å^3	$V_{solvent}$. Å^3		x. %
$MAPbI_3$	990.0	4	247.5	–	–	0
1:1	991.3(1)	4	247.8	DMSO	118.8	5.5
1:2	994.7(4)	4	248.7			6.6
1:3	994.5(2)	4	248.6			6.5
1:1	994.5(3)	4	248.6	DMF	128.4	5.8
1:2	998.6(5)	4	249.6			7.0
1:3	997.5(4)	4	249.4			6.7

It was found that at the same ratios of starting reagents, the structure of perovskite included the DMF solvent in a greater amount than DMSO.

The fact that the solvent is part of the structure of perovskite affects not only the structural parameters but also the electrophysical characteristics, in particular, the width of the bandgap (Table 9).

Table 9

Influence of the solvent on the electrophysical characteristics of perovskite $MAPbI_3$.

Solvent		DMF			DMSO		
PbI_2:MAI		1:1	1:2	1:3	1:1	1:2	1:3
Solvent content, %	0	5.8	7	6.7	5.5	6.6	6.5
Bandgap, eV	1.55 [18]	1.59	1.62	1.57	1.57	1.53	1.54

The bandgap for the perovskites obtained at different ratios of starting reagents in DMSO is less than for the films obtained using DMF.

CONCLUSIONS

The peculiarities of formation and properties of organic-inorganic $MAPbI_3$ perovskite films have been studied as a function of the ratio of starting reagents in DMF and DMSO solvents. As the PbI_2:MAI ratio increases, the temperature of the formation of single-phase $MAPbI_3$ perovskite film increases. It was found that when using the DMF solvent, the number of crystalline phases in the film depends on

the ratio of starting reagents. At a ratio of 1:1 in DMF, the number of phases is 4 and at 1:2, 1:3 5, and 3, respectively. When using DMSO, regardless of the ratio of starting reagents, there are 5 crystalline phases in the film.

Plots of the percentage of crystalline phases in the film versus the treatment temperature have been constructed for perovskite films synthesized at different ratios of starting reagents in the DMF, and DMSO solvents. It was shown that the formation of organic-inorganic perovskite occurs through the formation and decomposition of intermediate compounds (phases). Reactions of $MAPbI_3$ perovskite formation at different ratios PbI_2:MAI in DMF and DMSO have been obtained.

It was found that for the perovskite films obtained at different ratios PbI_2: MAI in DMF and DMSO, there are slight changes in the structural (unit cell volume) and electrophysical (bandgap) characteristics. These changes are related to the solvent that is included in the crystalline structure of perovskite. It was found that at the same ratios of starting reagents, DMF is included in the structure of perovskite in a greater amount than DMSO.

Acknowledgment. The authors express their gratitude to the Armed Forces of Ukraine for providing security to perform this work. This work has become possible only because of the fortitude and courage of the Ukrainian Army.

ВПЛИВ РОЗЧИННИКА ТА СПІВВІДНОШЕННЯ ВИХІДНИХ РЕАГЕНТІВ НА ВЛАСТИВОСТІ ОРГАНО-НЕОРГАНІЧНОГО ПЕРОВСЬКІТУ $MAPbI_3$

Торчинюк П. В.[1], В'юнов О. І.[1], Власюк В. М.[2], Костильов В. П.[2], Білоус А. Г.[1]

[1]Інститут загальної та неорганічної хімії ім. В. І. Вернадського НАН України, просп. Академіка Палладіна, 32/34, Київ, 03142, Україна
[2]Інститут фізики напівпровідників імені В. Є. Лашкарьова НАН України, просп. Науки, 41, Київ, 03028, Україна
** e-mail: vyunov@ionc.kiev.ua*

Синтезовано органо-неорганічний перовськіт $MAPbI_3$ ($CH_3NH_3PbI_3$) методом одностадійного осадження за різного співвідношення вихідних реагентів (PbI_2 та MAI, які брали у співвідношенні 1:1, 1:2, 1:3) у розчиннику ДМФА та ДМСО. Для отримання плівок органо-неорганічного перовськіту $MAPbI_3$ використовували метод spin-coating.

Досліджено особливості утворення та властивості плівок органо-неорганічного перовськіту $MAPbI_3$ залежно від співвідношення вихідних реагентів у розчиннику DMF, DMSO. Зі збільшенням співвідношення PbI_2:MAI зростає температура утворення однофазної плівки перовськіту $MAPbI_3$. Показано, що утворення органо-неорганічного перовськіту відбувається через утворення та розкладання проміжних сполук (фаз). Отримано реакції утворення перовськіту $MAPbI_3$ за різного співвідношення PbI_2:MAI у DMF, DMSO.

Встановлено, що структура перовськіту $MAPbI_3$ починає формуватися за температури 20–25 °С незалежно від співвідношення вихідних реагентів у DMF. При використанні DMSO структура перовськіту $MAPbI_3$ починає формуватися за температури 60 °С для співвідношень 1:1, 1:2, та при 70 °С для співвідношення 1:3.

Встановлено, що при використанні розчинника DMF кількість кристалічних фаз у плівці залежить від співвідношення вихідних реагентів. При співвідношенні 1:1 у DMF кількість фаз становить 4, а при 1:2, 1:3 – 5 та 3 відповідно. При використанні DMSO незалежно від співвідношення вихідних реагентів у плівці присутні 5 кристалічних фаз.

Для плівок перовськіту, отриманих за різного співвідношення вихідних реагентів у розчиннику DMF, DMSO, було побудовано залежність вмісту кристалічних фаз у плівці від температури оброблення. Встановлено, що для плівок перовськіту, отриманих за різного співвідношення PbI_2:MAI у DMF, DMSO спостерігаємо незначні зміни в структурних (об'єм елементарної комірки) та електрофізичних (ширина забороненої зони) характеристиках. Ці зміни пов'язані з розчинником, який входить у кристалічну структуру перовськіту. Встановлено, що за однакових співвідношень вихідних реагентів DMF входить в структуру перовськіту у більшій кількості, ніж DMSO.

Ключові слова: органо-неорганічний перовськіт, фазові перетворення, структурні параметри, електрофізичні характеристики.

REFERENCES

1. Yang Z., Zhang S., Li L., Chen W., Research progress on large-area perovskite thin films and solar modules. *Journal of Materiomics.* 2017. **3** (4). 231–244.
2. Jiang Q., Zhao Y., Zhang X., Yang X., Chen Y., Chu Z., Ye Q., Li X., Yin Z., You J., Surface passivation of perovskite film for efficient solar cells. *Nature photonics.* 2019. **13** (7). 460–466.
3. Zheng X., Chen B., Dai J., Fang Y., Bai Y., Lin Y., Wei H., Zeng X. C., Huang J., Defect passivation in hybrid perovskite solar cells using quaternary ammonium halide anions and cations. *Nature Energy.* 2017. **2** (7). 1–9.
4. Stolterfoht M., Wolff C. M., Márquez J. A., Zhang S., Hages C. J., Rothhardt D., Albrecht S., Burn P. L., Meredith P., Unold T., Neher D., Visualization and suppression of interfacial recombination for high-efficiency large-area pin perovskite solar cells. *Nature Energy.* 2018. **3** (10). 847–854.
5. Miyata A., Mitioglu A., Plochocka P., Portugall O., Wang J. T.-W., Stranks S. D., Snaith H. J., Nicholas R. J., Direct measurement of the exciton binding energy and effective masses for charge carriers in organic–inorganic tri-halide perovskites. *Nature Physics.* 2015. **11** (7). 582–587.
6. Saba M., Quochi F., Mura A., Bongiovanni G., Excited state properties of hybrid perovskites. *Accounts of Chemical Research.* 2016. **49** (1). 166–173.
7. Han T. H., Tan S., Xue J., Meng L., Lee J. W., Yang Y., Interface and Defect Engineering for Metal Halide Perovskite Optoelectronic Devices. *Advanced Materials.* 2019. **31** (47). 1803515.
8. Zhou Y., Zhao Y., Chemical stability and instability of inorganic halide perovskites.

Energy & Environmental Science. 2019. **12** (5). 1495–1511.
9. Arain Z., Liu C., Yang Y., Mateen M., Ren Y., Ding Y., Liu X., Ali Z., Kumar M., Dai S., Elucidating the dynamics of solvent engineering for perovskite solar cells. *Science China Materials.* 2018. **62** (2). 161–172.
10. Jung M., Ji S.-G., Kim G., Seok S. I., Perovskite precursor solution chemistry: from fundamentals to photovoltaic applications. *Chemical Society Reviews.* 2019. 48 (7). 2011–2038.
11. Kostylyov V. P., Sachenko A. V., Sokolovskyi I. O., Vlasiuk V. M., Torchyniuk P. V., V'yunov O. I., Belous A. G., Shkrebtii A. I., Influence of the reagents' ratio on photoelectric and optical properties of perovskite films for photovoltaics. *Semiconductor Physics, Quantum Electronics and Optoelectronics.* 2021, **24** (3). 295–303.
12. Torchyniuk P. V., V'yunov O. I., Kovalenko L. L., Ishchenko A. A., Kurdyukova I. V., Belous A. G., Influence of Solvent on Stability and Electrophysical Properties of Organic–Inorganic Perovskites Films $CH_3NH_3PbI_3$. *Theoretical and Experimental Chemistry.* 2021. **57** (2). 113–120.
13. Mei A., Li X., Liu L., Ku Z., Liu T., Rong Y., Xu M., Hu M., Chen J., Yang Y., Gratzel M., Han H., A hole-conductor-free, fully printable mesoscopic perovskite solar cell with high stability. *Science.* 2014. **345** (6194). 295–8.
14. Tress W., Marinova N., Moehl T., Zakeeruddin S. M., Nazeeruddin M. K., Grätzel M., Understanding the rate-dependent J–V hysteresis, slow time component, and aging in $CH_3NH_3PbI_3$ perovskite solar cells: the role of a compensated electric field. *Energy & Environmental Science.* 2015. **8** (3). 995–1004.
15. Certificate of Analysis. Standard Reference Material 1976, Instrument Sensitivity Standard for X-ray Powder Diffraction. National Institute of Standards & Technology, Gaithersburg. 1991. 1–4.
16. McCusker L., Von Dreele R., Cox D., Louer D., Scardi P., Rietveld refinement guidelines. *Journal of Applied Crystallography.* 1999. **32** (1). 36–50.
17. Tan Q., Hinrichs K., Mao-Dong H., Fengler S., Rappich J., Prajongtat P., Nickel N. H., Dittrich T., Temperature Dependent Diffusion of DMSO in $CH_3NH_3PbI_3$ Precursor Films During Layer Formation and Impact on Solar Cells. *ACS Applied Energy Materials.* 2019. **2** (7). 5116–5123.
18. Matsuura N., Umemoto K., Takeda Y., Formulation of stokes' radii in DMF, DMSO and propylene carbonate with solvent structure cavity size as parameter. *Bulletin of the Chemical Society of Japan.* 1975. **48** (8). 2253–2257.
19. Kieslich G., Sun S., Cheetham A. K., An extended Tolerance Factor approach for organic-inorganic perovskites. *Chem Sci.* 2015. **6** (6). 3430–3433.
20. Ansari M. I. H., Qurashi A., Nazeeruddin M. K., Frontiers, opportunities, and challenges in perovskite solar cells: A critical review. *Journal of Photochemistry and Photobiology C: Photochemistry Reviews.* 2018. **35**. 1–24.

Стаття надійшла 18.05.2022.

УДК 541.145 doi: 10.33609/2708-129X.88.04.2022.94-112

ФОТОКАТАЛІТИЧНА АКТИВНІСТЬ МЕЗОПОРИСТОГО TiO_2 (АНАТАЗ) У РЕАКЦІЇ ВИДІЛЕННЯ ВОДНЮ З ВОДНО-ЕТАНОЛЬНОЇ СУМІШІ

Н. І. Єрмохіна[1], Г. В. Коржак[1], Н. І. Романовська[1], В. М. Гребенніков[1], О. В. Шульженко[1], Д. О. Климчук[2], О. М. Пузій[3]*, П. А. Манорик[1]

[1]Інститут фізичної хімії ім. Л. В. Писаржевського НАН України, просп. Науки, 31, Київ 03028, Україна
[2]Інститут ботаніки НАН України, вул. Терещенківська, 2, Київ 01601, Україна
*[3]Національний авіаційний університет, просп. Любомира Гузара 1, Київ 03058, Україна, *e-mail: alexander.puziy@gmail.com*

Зразки мезопористого нанокристалічного TiO_2 (анатаз із розміром кристалітів близько 10 нм) було отримано золь-гель-методом за присутності темплату дібензо-18-краун-6 і невеликих добавок поверхнево-активної речовини додецилметилетиламонію броміду та/або йонів лантану (III) у поєднанні з гідротермальним обробленням з наступним прожарюванням на повітрі при 500 °C.

Фотокаталітичну активність отриманих зразків TiO_2 досліджували у реакції виділення H_2 з водно-етанольної суміші. Встановлено, що у всіх випадках використання гідротермального оброблення значно збільшує фотоактивність зразка, яка в деяких випадках у понад 3–4 рази перевищує відповідну характеристику для комерційного фотокаталізатора Evonik P25.

Показано, що отримані за однакових концентраціях реагентів в реакційної суміші зразки мікросфер TiO_2 демонструють дещо більшу фотокаталітичну активність, ніж відповідні стабілізовані лантаном зразки порошків мезопористого TiO_2 (частинки мікрометрового масштабу за присутності йонів лантану (III) не утворюються). Однак при збільшенні концентрації реагентів в реакційній суміші найбільшу фотокаталітичну активність має отриманий зразок, що містить лантан.

Ключові слова: золь-гель-синтез, мезопористі TiO_2 мікросфери, анатаз, лантан, виділення H_2.

ВСТУП. У сучасних напрямках зеленої хімії нанорозмірний діоксид титану з контрольованою морфологією та текстурою розглядають як найбільш перспективну основу для формування напівпровідникових фотокаталізаторів внаслідок його нетоксичності, високої стійкості до фото- та хімічної корозії, комерційної доступності тощо. Такі наноструктуровані системи потрібні для вирішення глобальних енергетичних та екологічних проблем [1–7].

Ефективність фотокаталітичних систем визначають набором їхніх різних параметрів (характеристик), таких як фазовий склад, ступінь кристалічності, розмір кристалітів, пористість, питома площа поверхні тощо [1, 4, 8, 9]. Мезопористий нанокристалічний TiO_2 (meso-nc-TiO_2) з необхідним поєднанням перелічених вище параметрів демонструє значно більшу фотоактивність, порівняно з нанокристалічним TiO_2 Evonik P25 [7, 10–17].

На сьогодні серед існуючих способів отримання мезопористих оксидів золь-гель-метод є одним із найбільш досконалих [13–23]. Умови проведення золь-гель-процесу та подальше сольво-(гідро-) термальне оброблення (ГТО) (за відносно низьких температур < 200 °С) визначають фазовий склад, кристалічність, морфологію та текстуру отриманих зразків meso-nc-TiO_2. Найбільш фотоактивною кристалічною фазою TiO_2 є анатаз [24]. Кристалізацію зразків TiO_2 проводять, як правило, за температури близько 500 °С [25–30].

Використання темплату і введення різних добавок, що впливають на взаємодію між частинками TiO_2 при утворенні пористого каркасу, дозволяє досягти широкого розмаїття ієрархічно організованих нано- та мікрометрового масштабу (у т. ч. мезопористих мікросфер) частинок TiO_2, які мають високу фотокаталітичну активність [25–33].

Пористі мікросфери TiO_2 демонструють очевидну перевагу як фотокаталізаторів, зокрема в процесах окиснення органічних барвників [34–40], бензолу [41], толуолу [42], бісфенолу А [43], пентахлорфенолу [44], 2-пропанолу [45], сульфонамідів [46], оксидів азоту [47], відновлення Cr(VI) [35], CO_2 [48] тощо. Значне зростання фотоактивності TiO_2 мікросфер, вочевидь, є наслідком можливості проникнення світлового потоку у внутрішні пори мікросфер, де він зазнає багаторазового заломлення та відбиття, тим самим збільшуючи ймовірність поглинання світла [1, 31, 39]. Також є очевидним, що в таких структурах, які сформовані наночастинками (первинні частинки), будуть зберігатися розмірні ефекти, що мають важливе значення для перебігу фотокаталітичних процесів, а саме велика концентрація поверхневих атомів, підвищене світлопоглинання, швидкий вихід на поверхню фотогенерованих зарядів та їхній просторовий поділ і т. д.

Використання в процесі золь-гель-синтезу meso-nc-TiO_2 невеликої добавки йонів La^{3+}, що перешкоджають трансформації анатаз – рутил, дозволяє значно збільшити термічну стабільність, текстурні характеристики та фотокаталітичну активність отриманих мезопористих матеріалів TiO_2. Роль рідкісноземельного катіону у стабілізації структури автори [49–57] пояснюють включенням йонів La^{3+} у каркас оксидної системи TiO_2. Більш електропозитивний, порівняно з титаном, лантан утворює зв'язок La–O. За рахунок часткового перенесення електронів зі зв'язку La–O на зв'язок Ti–O відбувається зміцнення зв'язку Ti–O.

Раніше нами було запропоновано підходи до отримання meso-nc-TiO_2 (анатаз та різнофазові композиції) золь-гель-методом із використанням тетрабутоксиду титану (ТВОТ) у бутанолі (BuOH) за присутності як темплату дибензо-18-краун-6 (DB18C6) без/або у поєднанні з гідротермальним

обробленням при 175 °С проміжного продукту та подальшим прожарюванням при 500 °С [58–61]. Було показано, що введення в реакційну суміш невеликих добавок солі лантану та поверхнево активної речовини (ПАР), наприклад, додецилметилетиламонію броміду (DDMEABr) або пальмітинової кислоти (Palm), значно впливає на ступінь кристалізації, текстуру і морфологію отриманих зразків TiO_2. Встановлено [41], що зразки meso-nc-TiO_2 виявляють високу фотокаталітичну активність у реакціях газофазного окиснення бензолу та етанолу.

У цій роботі розглянуто фотокаталітичні властивості різних зразків meso-nc-TiO_2, які було отримано відповідно до зазначених вище підходів, у реакції виділення H_2 з водно-етанольної суміші.

ЕКСПЕРИМЕНТ ТА ОБГОВОРЕННЯ РЕЗУЛЬТАТІВ

У роботі використовували тетрабутоксид титану (IV), додецилдиметилетиламонію бромід, дибензо-18-краун-6 ("Fluka"), пальмітинову кислоту, н-бутанол, $LaCl_3 \cdot 7H_2O$, $CuCl_2$, NaCl («Хімлаборреактив»), етанол (96%), TiO_2 Evonik P25.

Зразки meso-nc-TiO_2 було отримано модифікованим золь-гель-методом аналогічно [59, 60] шляхом гідролізу тетрабутоксиду титану в бутанолі за присутності комплексу натрію з дибензо-18-краун-6 [Na(DB18C6)] Cl (через низьку розчинність дибензо-18-краун-6 у бутанолі було використано його натрієвий комплекс) із введенням (або без) невеликих добавок поверхнево-активної речовини (DDMEABr або пальмітинової кислоти) та солі лантану. Отриманий продукт піддавали ГТО при 175 °С протягом 24 год. із наступним відпалом при 500 °С на повітрі протягом 4 год. Зразки meso-nc-TiO_2, одержані за різних умов, позначено як Tn, T(MS) n та TnH, T(MS)nH, де MS – мікросфери, n – номер зразка та H – гідротермальне оброблення. Молярні композиції реакційної суміші, використані для синтезу зразків meso-nc-TiO_2, наведено в таблиці 1.

Для рентгенофазного аналізу кристалічної структури зразків використовували дифрактометр "ДРОН-3М" (CuK_α). Середній розмір кристалітів TiO_2 розраховували за шириною дифракційного піку анатазу (101) при $2\theta = 25{,}4^o$, використовуючи добре відому формулу Шеррера.

Зразки досліджували методами просвічувальної (ПЕМ) та сканувальної (СЕМ) електронної мікроскопії з використанням мікроскопів відповідно JEM 1230 та JSM-6060LA («JEOL»). Ізотерми адсорбції/десорбції N_2 реєстрували при –196 °С на газо-адсорбційному аналізаторі Autosorb-6 (Quantachrome). Перед адсорбцією зразок відкачували при 200 °С протягом 20 год. Питому поверхню ($S_{пит.}$) та середній діаметр пор ($D_{пор}$) визначали за методом BET та BJH відповідно.

Розподіл пор за розмірами розраховували з десорбційної гілки ізотерми за допомогою методу NLDFT, використовуючи циліндричну модель пор. Загальна кількість N_2 адсорбованого при $p/p^0 = 0{,}997$ використано для визначення загального об'єму пор (Vпор).

Фотокаталітичну активність отриманих зразків meso-nc-TiO_2 досліджували у модельній реакції фотокаталітичного виділення водню з водно-спиртових сумішей. Умови проведення реакції аналогічні до умов, описаних у роботі [62].

Таблиця 1
Table 1

Умови синтезу meso-nc-TiO_2 зразків
Conditions for the synthesis of meso-nc-TiO_2 samples

Зразок	ТВОТ	NaDBCCl	BuOH	Добавка	
				ПАР	La^{3+}
T(MS) 1	1,0	0,12	78,0	-	-
T(MS) 1H	1,0	0,12	78,0	-	-
T(MS) 2H	3,0	0,36	78,0	-	-
T(MS) 3	1,0	0,12	78,0	0,02 (DDMEABr)	-
T(MS) 3H	1,0	0,12	78,0	0,02 (DDMEABr)	-
T(MS) 4*	1,0	0,12	78,0	-	-
T(MS) 4H*	1,0	0,12	78,0	-	-
T(MS) 5H	1,0	0,12	78,0	0,02 (Palm)	-
T6	1,0	0,12	78,0	-	0,01
T6H	1,0	0,12	78,0	-	0,01
T7	1,0	0,12	78,0	0,02 (DDMEABr)	0,01
T7H	1,0	0,12	78,0	0,02 (DDMEABr)	0,01
T8	2,0	0,24	78,0	0,02 (DDMEABr)	0,01
T8H	2,0	0,24	78,0	0,02 (DDMEABr)	0,01

* Додано воду (1,0 ТВОТ:3H_2O); у решті випадків гідроліз здійснювався вологою з повітря.

Опромінення зразків TiO_2 здійснювали УФ світлом (λ = 310–390 нм) у системі, що містить водно-етанальну суміш (4 об.% H_2O) та $CuCl_2$. Як зразок порівняння використовували комерційний фотокаталізатор TiO_2 Evonik P25. Усі зразки meso-nc-TiO_2, фізичні характеристики яких представлено у табл. 2, отримано у різних умовах золь-гель- синтезу (табл. 1). Як видно, зразки мікросфер мають нижчі величини текстурних характеристик порівняно з відповідними величинами для зразків, отриманих за присутності невеликих добавок йонів La^{3+} або йонів La^{3+} у поєднанні з ПАР. Як випливає зі співставлення текстурних параметрів зразків (табл. 1, 2), гідротермальне оброблення зразка перед кальцинуванням призводить до кардинального зростання $S_{пит.}$, $V_{пор.}$ та $D_{пор,}$. Мікросфери TiO_2 являють собою пористі утворення мікрометрового масштабу (розміром від 1 до 3 мкм), що мають виражену тенденцію до агломерації, внаслідок коалесценції сфер у процесі досить тривалого прожарювання при 500 °С [59]. Введення в реакційну суміш добавки йонів La^{3+} перешкоджає утворенню мікросфер [63]. Як приклад на рис. 1(а-з) представлено ПЕМ- та СЕМ-зображення зразків мікросфер T(MS)2H, T(MS)5H (у тому числі фрагменти зруйнованих мікросфер) та зразків T6H, T8H, отриманих за присутності йонів La^{3+} та їхньої дифрактограми (рис.1 і).

Мікросфери TiO_2 мають ієрархічну будову – вони утворені досить однорідними сферичними частинками розміром від 30 до 200 нм, які, своєю чергою, складаються з первинних будівельних одиниць – однорідних, з чітко вираженою сферичною формою частинок (розміром близько 10 нм), які несуттєво розрізняються між собою

за розміром, про що свідчать ПЕМ-дослідження зразків (рис. 1(а, в) та розрахунки за допомогою рівняння Шеррера з дифрактограми (табл.1, рис. 1 і)).

Слід зазначити, що введення в реакційну суміш при синтезі невеликої добавки пальмітинової кислоти специфічно впливає на морфологію та структуру отриманого продукту TiO_2. Мікрочастинки у зразку T(MS)5H (рис. 1 (б і г)), порівняно з іншими зразками мікросфер [59], являють собою складні агломерати TiO_2 сфероподібної форми (розміром близько 2 мкм), які утворені великими структурними зернами (~200 нм). Ці зерна після ультразвукового оброблення розпадаються на дрібніші структурні одиниці – наночастинки розміром 30–35 нм.

У всіх зразках, отриманих за присутності йонів La^{3+}, мікросфери взагалі не утворюються, а зразки meso-nc-TiO_2 є пористими однорідними порошками, які складаються з частинок сферичної (або сфероїдальної) форми, розмір яких близько 50 нм. Ці наночастинки (вторинні) утворені агрегацією кристалітів анатазу (первинних частинок) розміром близько 10 нм (рис. 1(д–з)). Мезопори у всіх зразках є простором у порах, сформованих шляхом агломерації вторинних частинок.

На рис. 1(і, к) представлено дифрактограми зразків T(MS)2H, T(MS)5H та T6H, T8H. У всіх дифрактограмах головні дифракційні піки індексовано як (101), (200), (105) та (211) рефлекси фази анатазу (JCPDS, № 21–1272) за повної відсутності будь-яких ознак кристалічних фаз брукіту та рутилу.

Таблиця 2
Table 2

Текстурні характеристики зразків meso-nc-TiO_2, а також їхні фотокаталітичні властивості у процесі відновлення води етанолом

Textural characteristics of meso-nc-TiO_2 samples, as well as their photocatalytic properties in the process of water reduction with ethanol.

Зразок	$S_{пит}$, $м^2/г$	$V_{пор}$, $см^3/г$	$D_{пор}$, нм	Розмір кристалітів, нм	H_2 10^7, моль/хв.
				XRD	
T(MS)1	61	0,14	9,0	10,5	3,8
T(MS)1H	84	0,33	15,5	11,0	6,6
T(MS)2H	92	0,37	16,2	10,5	8,5
T(MS)3	33	0,06	5,3	9,9	3,0
T(MS)3H	95	0,46	19,4	11,5	7,2
T(MS)4	97	0,30	12,3	8,7	4,0
T(MS)4H	116	0,50	17,3	10,0	5,0
T(MS)5H	88	0,48	21,8	10,0	6,0
T6	71	0,13	7,0	6,6	2,3
T6H	128	0,54	18,6	6,3	4,9
T7	71	0,14	7,0	6,8	3,3
T7H	131	0,59	15,9	6,6	5,3
T8	69	0,20	13,9	9,9	4,3
T8H	137	0,97	17,3	7,2	9,5
P25	50			25	2,2

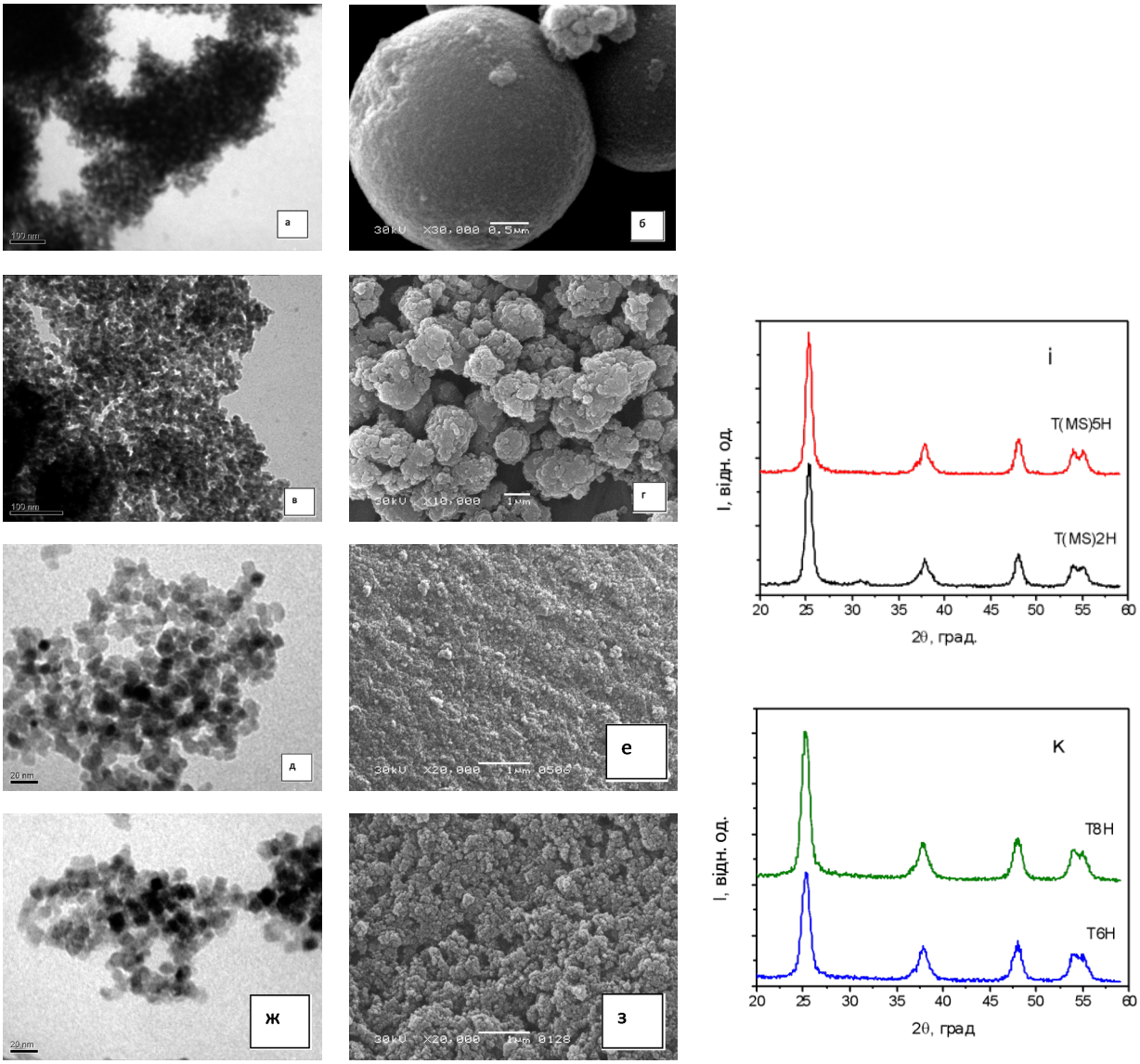

Рис. 1. ПЕМ- та СЕМ-зображення зразків meso-nc-TiO_2: T(MS)2H (а, б), T(MS)5H (в, г), T6H (д, е), T8H (ж, з) та їхні дифрактограми (і, к)

Fig. 1 TEM and SEM images of meso-nc-TiO_2 samples: T (MS) 2H (a, b), T (MS) 5H (c, d), T6H (d, e), T8H (w, c) and their diffraction patterns (i, k).

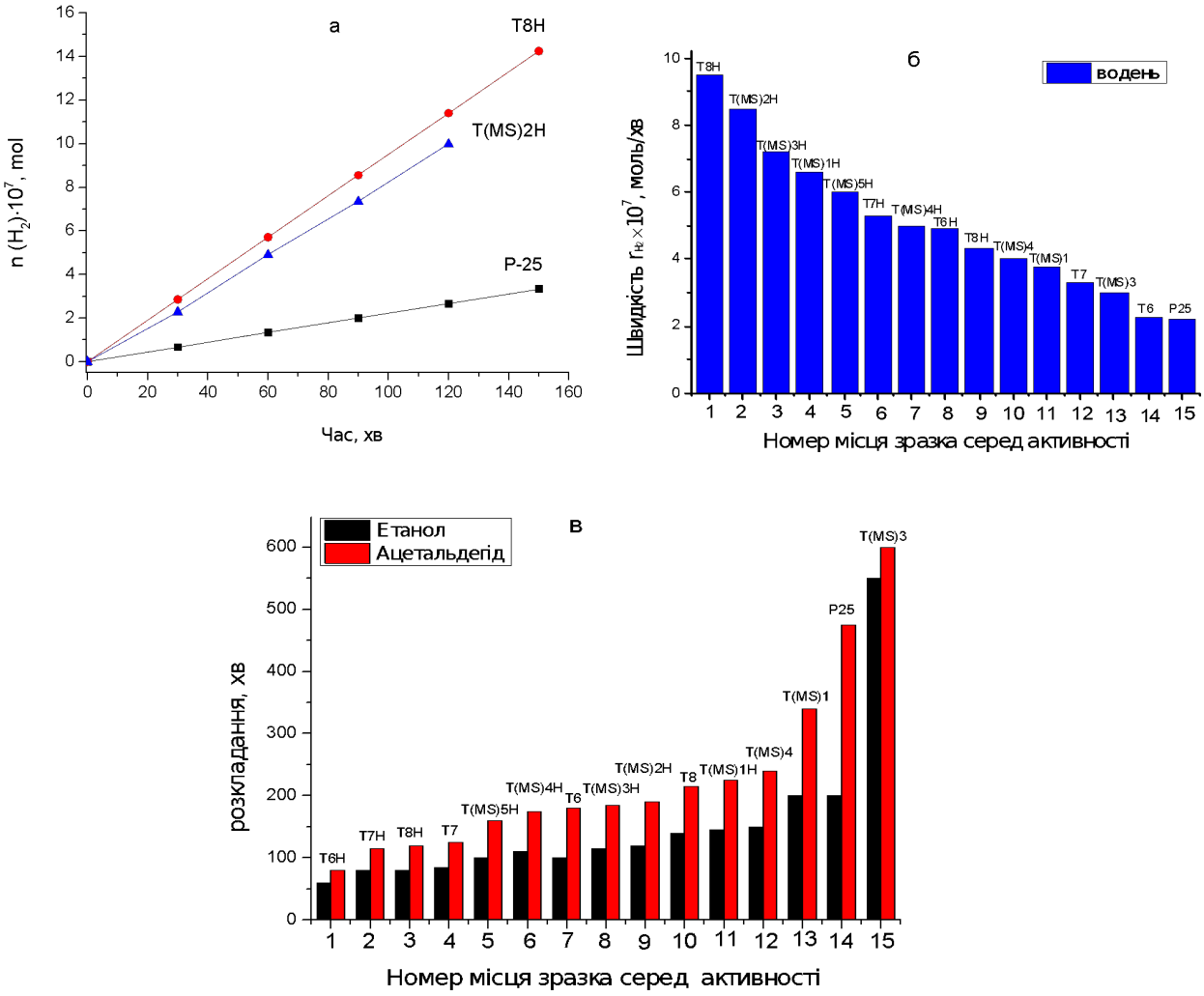

Рис. 2. Кінетичні криві накопичення водню в процесі фотокаталітичного відновлення води етанолом за присутності зразків T8H, T(MS)2H та TiO_2 Evonic P25(a); швидкість фотокаталітичного виділення H_2 (б) та час повного фотокаталітичного окислення етанолу та ацетальдегіду в системі за участю різних зразків meso-nc-TiO_2 (в)

Fig. 2. Kinetic curves of hydrogen accumulation in the process of photocatalytic reduction of water with ethanol in the presence of samples T8H, T (MS) 2H and TiO_2 Evonic P25 (a); rate of photocatalytic release of H2 (b) and time of complete photocatalytic oxidation of ethanol and acetaldehyde in the system with the participation of different samples of meso-nc-TiO_2 (c).

Раніше нами було показано фотокаталітичну активність мезопористого TiO_2, модифікованого наночастинками металів (Cu, Ag, Ni), у процесі виділення водню з водно-етанольних сумішей за дії УФ-світла [64]. У досліджених системах фотоосаджені наночастинки металу відіграють роль співкаталізатора, який акцептує фотогенеровані в зоні провідності TiO_2 електрони та прискорює їхнє перенесення на молекулу води. Найбільш активним співкаталізатором виявилися наночастинки міді. Водночас здійснюється заповнення дірок валентної зони TiO_2 за допомогою перенесення електронів молекул етанолу. В аналогічних умовах при опроміненні зразків meso-nc-TiO_2 (Табл. 2) відбувається швидке фотоосадження наночастинок міді, яке можна спостерігати візуально за зміни забарвлення зразка TiO_2 від білого до темно-коричневого. Швидкість процесу виділення молекулярного водню зберігається постійною протягом усього часу вимірювання. На рис. 2а як приклад наведено кінетичні криві для найбільш активних зразків T8H та T(MS)2H. У цих умовах зразок P25 проявляє значно нижчу фотокаталітичну активність. Як видно з таблиці 2 та рис. 2б, виділення водню за присутності зразка T8H відбувається зі швидкістю більш ніж вчетверо, а у разі зразка T(MS)2H майже вчетверо вищою за швидкість цього процесу за присутності P25.

Комерційний фотокаталізатор складається з суміші нанокристалічних фаз анатазу (≈80%) та рутилу (≈20%) із середнім розміром частинок 20–25 нм та питомою поверхнею 50 $м^2/г$, що значно поступається за величиною відповідним значенням питомої поверхні зразків meso-nc-TiO_2, за винятком зразка T(MS)3 (Табл. 2). Фотокаталітичну активність P25 прийнято пов'язувати з можливістю просторового поділу фотогенерованих різнойменних носіїв заряду між нанокристалами анатазу та рутилу через невелику різницю у величині потенціалу зони провідності цих фаз TiO_2 [65].

Гістограми на рис. 2б наочно демонструють вищу фотокаталітичну активність зразків meso-nc-TiO_2 порівняно з P25. Цілком очевидним є підвищення (більшою чи меншою мірою) активності всіх зразків, які було отримано з використанням ГТО. Ключовий вплив ГТО на підвищення фотоактивності зразків, мабуть, є наслідком кардинального збільшення в оброблених зразках об'єму та діаметра пор, а також зменшенням розмірів кристалітів анатазу. Ці зміни (поряд зі значним зростанням питомої площі поверхні) є більш глибокими для зразків, отриманих за присутності йонів La^{3+}. Серед зразків, отриманих за одних і тих самих концентраційних умов (Табл.1), найбільш активними є зразки мікросфер T(MS)3H, T(MS)1H і T(MS)5H, незважаючи на те, що вони мають менші величини питомої поверхні порівняно зі зразками T6H та T7H. Першим у цьому ряду стоїть зразок T(MS)3H (отриманий за присутності добавки DDMEABr). Зразок мікросфер T(MS)2H (отриманий при збільшенні втричі концентрації реагентів у реакційній суміші) має найбільшу активність серед зразків мікросфер (займає друге місце в загальному ряду зразків). Підвищена фотоактивність мікросфер TiO_2, ймовірно, зумовлена наявністю точок контакту між нещільно агрегованими нанокристалами TiO_2 у їхньому складі, що сприяє електронному транспорту

по мережі контактуючих частинок напівпровідника до наночасток міді, на яких відбувається відновлення води. Дещо вищу активність T(MS)1H порівняно з T(MS)5H можна пояснити більш регулярною формою зразка мікросфер T(MS)1H, що дозволяє повніше реалізувати ефект множинного променезаломлення/світлорозсіювання в об'ємі такої мікросфери та досягти більш інтенсивного поглинання світла [1, 31, 39].

Провідне місце належить зразку T8H, який отримано з використанням добавок йонів La^{3+} та DDMEABr за подвоєної концентрації реагентів у реакційній суміші. Ймовірно, це можна пояснити високими текстурними характеристиками зразка у поєднанні з особливостями його морфології – утворенням вторинних наночасток агломерованих утворень та впливом йонів La^{3+} [60]. Особливо слід відзначити той факт, що фотокаталітична активність зразків, отриманих за присутності йонів La^{3+}, зменшується при зменшенні величини їхньої питомої поверхні.

Незважаючи на те, що зразки мікросфер T(MS)2H, T(MS)3H, T(MS)1H, T(MS)5H та T(MS)4H мають менші величини питомої поверхні порівняно зі зразками T6H, T7H та T8H, вони за своєю фотоактивністю займають місця з другого по п'яте і сьоме, причому зразок T7H (шосте місце) за своєю активністю практично не поступається зразку T(MS)4.

Порівняння гістограм для процесу виділення водню (рис. 2б) та відповідних гістограм для процесу газофазного окиснення етанолу за присутності зразків meso-nc-TiO_2 [59,60] (рис. 2в) демонструє різні картини фотоактивності зразків. У процесі окиснення спирту, згідно з рис. 2в, найбільш активні зразки T6H, T7H і T8H (займають перші три місця) у ряді активності для процесу виділення водню займають відповідно восьме, шосте та перше місце. Серед зразків мікросфер явну перевагу має зразок T(MS)5H. У процесі виділення водню його перевищують зразки мікросфер T(MS)2H, T(MS)3H і T(MS)1H. Аналіз даних дозволяє припустити, що наявність контакту між окремими нещільно агрегованими нанокристалами TiO_2, що є значущим фактором у процесі виділення водню в цій фотокаталітичній системі, напевне, в процесі окиснення етанолу відіграє другорядну роль, а ключовим фактором служить розмір пор. У зразку T(MS)5H, ймовірно, мають місце сприятливіші умови для транспорту кисню до адсорбованого у більших мезопорах фотокаталізатора етанолу та проміжним продуктом його окиснення. Аналогічну картину спостерігаємо у процесі фотокаталітичного окиснення бензолу за присутності зразків цих мікросфер [58].

ВИСНОВКИ

Таким чином, на прикладі широкого кола зразків meso-nc-TiO_2 (анатаз), отриманих у рамках одного модифікованого золь-гель-методу, встановлено, що всі зразки виявляють високу фотокаталітичну активність у процесі виділення H_2 з водно-етанольної суміші. Зразки, що пройшли гідротермальне оброблення, демонструють найбільшу фотокаталітичну активність, що значно перевищує активність комерційного фотокаталізатора Evonik P25, а в деяких випадках більш ніж у 3–4 рази.

Показано, що серед зразків meso-nc-TiO_2, отриманих за однакових концентрацій реагентів реакційної суміші, найбільшу

активність мають зразки мікросфер, а введення добавки DDMEABr або підвищення концентрації реагентів призводить до підвищення фотокаталітичної активності отриманих мікросфер. За присутності добавки йонів La^{3+} частинки мікрометрового масштабу не утворюються, причому фотокаталітична активність отриманих зразків знижується. Однак у разі збільшення концентрації реагентів у реакційній суміші отриманий лантановмісний фотокаталізатор має найбільшу активність.

Роботу виконано за підтримки Національної академії наук України.

PHOTOCATALYTIC ACTIVITY OF MESOPOROUS TiO2 (ANATAS) IN THE REACTION OF HYDROGEN RELEASE FROM AQUEOUS-ETHANOLIC MIXTURE

N. I. Ermokhina[1], G. V. Korzhak[1], N. I. Romanovska[1], V. N. Grebennikov[1], A. V. Shulzshenko[1], D. O. Klymchuk[2], A. M. Puziy[3]*, P. A. Manorik[1]

[1] Pisarzhevskii Institute of Physical Chemistry of the National Academy of Sciences of Ukraine, Ave. Science, 31, Kyiv 03028, Ukraine
[2] Institute of Botany of the National Academy of Sciences of Ukraine, Tereshchenkivska St. 2, Kyiv 01601, Ukraine
[3] National Aviation University, Liubomyr Huzar ave. 1, Kyiv 03058, Ukraine,
**e-mail: alexander.puziy@gmail.com*

Samples of mesoporous nanocrystalline titanium dioxide (anatase with a crystallite size of about 10 nm) were obtained by a modified sol-gel method in the presence of a template of dibenzo-18-crown-6 and small additives of surfactant (dodecylmethylethylammonium bromide) or ions of lanthanum (III) in butyl alcohol in combination with hydrothermal treatment at 175 °C for 24 hours followed by calcination in air at 500 °C for 4 hours. The photocatalytic activity of the obtained TiO_2 samples was investigated in a model reaction of the photocatalytic release of H_2 from an aqueous-ethanol mixture. It was found that in all cases the use of hydrothermal treatment significantly increases the photoactivity of the obtained sample, which in some cases is more than 3-4 times higher than the corresponding characteristic for commercial photocatalyst Evonik P25. The key effect of hydrothermal treatment on the increase of photoactivity of the samples is probably the consequence of a drastic increase in the treated samples of pore volume and diameter, as well as a decrease in the size of anatase crystallites. These changes (along with a significant increase in the specific surface area) are greater for samples obtained in the presence of La^{3+} ions. It is shown that samples of TiO_2 microspheres obtained at the same concentrations of reagents in the reaction mixture show slightly higher photocatalytic activity than the corresponding lanthanum-stabilized samples of mesoporous TiO_2 powders (micrometer-scale particles are not formed in the presence of lanthanum (III) ions). However, with an increasing concentration of reagents in the reaction mixture, the photocatalytic activity has the sample containing lanthanum. Probably, this can be explained by the high textural characteristics of the TiO_2

sample in combination with the peculiarities of its morphology - the formation of secondary nanoparticles of agglomerated formations and the influence of La^{3+} ions. It is worth noting that the photocatalytic activity of TiO_2 samples prepared in the presence of La^{3+} ions reduces as their specific surface area decreases.

Keywords: sol-gel synthesis, mesoporous TiO_2 microspheres, anatase, lanthanum, H_2 release.

ЛІТЕРАТУРА

1. *Nakata K., Fujishima A.* TiO_2 photocatalysis: design and applications // Journal of Photochemistry and Photobiology C: Photochemistry Reviews, 2012. **13**, 3. P. 169–189. https://doi.org/10.1016/j.jphotochemrev.2012. 06.001
2. *Pelaez M., Nolan N.T., Pillai S.C., Seery M.K., Falaras P., Kontos A.G., Dunlop P.S.M., Hamilton J.W.J., Byrne J.A., O'Shea K., Entezari M.H., Dionysiou D.D.* A review on the visible light active titanium dioxide photocatalysts for environmental applications // Applied Catalysis B: Environmental, 2012. **125**. P 331–349. https://doi.org/10.1016/j.apcatb. 2012.05.036
3. *Tong H., Ouyang S., Bi Y., Umezawa N., Oshikiri M., Ye* J. Nanophotocatalytic materials: possibilities and challenges // Advance Materials, 2012. **24**. 2. P 229–251. https://doi.org/10.1002/adma.201102752
4. *Fresno F., Portela R., Suárez S., Coronado J. M.* Photocatalytic materials: recent achievements and near future trends // Journal of Material Chemistry A., 2014. **2**, 9. P. 2863–2884. https://doi.org/10.1039/C3TA13793G
5. *Wang Y., Sun C., Zhao X., Cui B., Zeng Z., Wang A., Liu G., Cui H.* The application of nano-TiO_2 photo semiconductors in agriculture // Nanoscale Research Letters, 2016. **11**. 1. P. 529. http://dx.doi.org/10.1186/s11671-016-1721-1
6. *Kumar N., Chauhan N.S., Mittal A., Sharma S.* TiO_2 and its composites as promising biomaterials: a review // BioMetals, 2018. **31**, 2. P. 147–159. https://doi.org/10.1007/s10534-018-0078-6
7. *Noman M.T., Ashraf M.A., Ali A.* Synthesis and applications of nano-TiO_2: a review // Environmental Science and Pollution Research, 2019. **26**, 4. P. 3262–3291. https://doi.org/10.1007/s11356-018-3884-z
8. *Humayun M., Raziq F., Khan A., Luo W.* Modification strategies of TiO_2 for potential applications in photocatalysis: a critical review // Green Chemistry Letters and Reviews, 2018. **11**, 2. P. 86–102. https://doi.org/10. 1080/17518253.2018.1440324
9. *Paul K.K., Giri P.K.* Shape tailored TiO_2 nanostructures and their hybrids for advanced energy and environmental applications: a review // Journal of Nanoscience and Nanotechnology, 2018. **19**, 1. P. 307–331. https://doi.org/10.1166/jnn.2019.15778
10. *Dionysiou D.D., Puma G.Li., Ye J., Schneider J., Bahnemann D.* Photocatalysis: Applications // Royal Society of Chemistry, Cambridge. 2016. https://doi.org/10.1039/9781782627104
11. *Schneider J., Matsuoka M., Takeuchi M., Zhang J., Horiuchi Y., Anpo M., Bahnemann D.W.* Understanding TiO_2 photocatalysis: mechanisms and materials // Chemical Reviews, 2014. **114**, 19. P. 9919–9986. https://doi.org/10.1021/cr5001892
12. *Anpo M., Kamat P.V.* Environmentally benign photocatalysts // Springer, New York, 2010. https://doi.org/10.1007/978-0-387-48444-0
13. *Laura Cano-Casanova, Ana Amorós-Pérez, Maria Angeles Lillo-Ródenas and María del Carmen Román-Martínez.* Effect of the preparation method (sol–gel or hydrothermal) and conditions on the TiO_2 properties and activity for propane oxidation // Materials (Basel), 2018. **11**, 11. P. 2227. https://doi.org/10.3390/ma11112227
14. *Antonelli D.M., Ying J.Y.* Synthesis of hexagonally packed mesoporous TiO_2 by a modified

sol–gel method // Angewandte Chemie International Edition in English, 1995. **34**, 18. P. 2014–2017. https://doi.org/10.1002/anie. 199520141
15. *Ismail A.A., Bahnemann D.W.* Mesoporous titania photocatalysts: preparation, characterization and reaction mechanisms // Journal of Material Chemistry, 2011. **21**, 32. P. 11686. https://doi.org/10.1039/c1jm10407a
16. *Kumar A.* Different methods used for the synthesis of TiO_2 based nonmaterial's: a review. // American Journal of Nano Research and Application, 2018. **6**, 1. P. 1. https://doi.org/10.11648/j.nano.20180601.11
17. *Shayegan Z., Lee C-S., Haghighat F.* TiO_2 photocatalyst for removal of volatile organic compounds in gas phase: a review // Chemical Engineering Journal, 2018. **334**. P. 2408–2439. https://doi.org/10.1016/j.cej.2017. 09.153
18. *Shen X., Tian B., Zhang J.* Tailored preparation of titania with controllable phases of anatase and brookite by an alkalescent hydrothermal route // Catalysis Today, 2013. **201**. P. 151–158. https://doi.org/10.1016/j.cattod.2012.04.038
19. *Wu M., Lin G., Chen D., Wang G., He D., Feng S., Xu R.* Solhydrothermal synthesis and hydrothermally structural evolution of nanocrystal titanium dioxide // Chemistry of Materials, 2002. **14**, 5. P. 1974–1980. https://doi.org/10.1021/cm0102739
20. *Yang X., Konishi H., Xu H., Wu M.* Comparative Sol– hydro(solvo)thermal synthesis of TiO_2 nanocrystals // European Journal of Inorganic Chemistry, 2006. **11**. P. 2229–2235. https://doi.org/10.1002/ejic.200500855
21. *Wang C-C., Ying J.Y.* Sol–gel synthesis and hydrothermal processing of anatase and rutile titania nanocrystals // Chemistry of Materials, 1999. **11**, 11. P. 3113–3120. https://doi.org/10.1021/cm990180f
22. *Castrejon-Sanchez V., Lopez R., Ramon-Gonzalez M., Enriquez-Perez A., Camacho-Lopez M., Villa-Sanchez G.* Annealing control on the anatase/rutile ratio of nanostructured titanium dioxide obtained by sol–gel // Crystals, 2018. **9**, 1. P. 22. https://doi.org/10.3390/cryst9010022
23. *Bamne J., Sharma P.K., Haque F.Z.* Effect of solvent mixing and calcination temperature on the growth of TiO_2 nanoparticle prepared via sol–gel method // *Materials Focus*, 2018. **7**, 2. P. 232–241. https://doi.org/10.1166/mat.2018.1502
24. *Luttrell T., Halpegamage S., Tao J., Kramer A., Sutter E., Batzill M.* Why is anatase a better photocatalyst than rutile? Model studies on epitaxial TiO_2 films // Scientific Reports, 2015. **4**, 1. P. 4043. https://doi.org/10.1038/srep04043
25. *Sheikhnejad-Bishe O., Zhao F., Rajabtabar-Darvishi A., Khodadad E., Mostofizadeh A., Huang Y.* Influence of temperature and surfactant on the photocatalytic performance of TiO_2 Nanoparticles // International Journal of Electrochemical Science, 2014. **9**, 8. P. 4230–4240.
26. *Masolo E., Meloni M., Garroni S., Mulas G., Enzo S., Baro M., Rossinyol E., Rzeszutek A., Herrmann-Geppert I., Pilo M.* Mesoporous titania powders: the role of precursors, ligand addition and calcination rate on their morphology, crystalline structure and photocatalytic activity // Nanomaterials, 2014. **4**, 3. P. 583–598. https://doi.org/10.3390/nano4030583
27. *Yue Y., Gao Z.* Synthesis of mesoporous TiO_2 with a crystalline framework // Chemical Communications, 2000. **18**. P. 1755–1756. https://doi.org/10.1039/b004124f
28. *Byrappa K., Adschiri T.* Hydrothermal technology for nanotechnology // Progress in Crystal Growth and Characterization of Materials, 2007. **53**, 2. P. 117–166. https://doi.org/10.1016/j.pcrysgrow.2007.04.001
29. *Luis A.M., Neves M.C., Mendonca M.H., Monteiro O.C.* Influence of calcination parameters on the TiO_2 photocatalytic properties // Materials Chemistry and Physics, 2011. **125**, 1–2. P. 20–25. https://doi.org/10.1016/j.matchemphys.2010.08.019

30. *Agarwala P., Makkar P., Sharma S., Garg R.* The effect of heat treatment of TiO_2 nanoparticles on photovoltaic performance of fabricated DSSCs // Journal of Materials Engineering and Performance, 2014. **23**, 10. P. 3703–3709. https://doi.org/10.1007/s11665-014-1131-4
31. *Fattakhova-Rohlfing D., Zaleska A., Bein T,* Three-Dimensional Titanium Dioxide // Nanomaterials, Chem. Rev, 2014. **114**. P. 9487–9558.
32. *Chen L-H., Li X-Y., Deng Z., Hu Z-Y., Rooke J.C., Krief A., Yang X-Y., Su B-L.* Hydrothermal and surfactant treatment to enhance the photocatalytic activity of hierarchically meso – macroporous titanias // Catalysis Today, 2013. **212**. P. 89–97. https://doi.org/10.1016/j.cattod. 2012.07.021
33. *Hung I-M., Wang Y., Huang C-F., Fan Y-S., Han Y-J, Peng H-W.* Effects of templating surfactant concentrations on the mesostructure of ordered mesoporous anatase TiO_2 by an evaporation-induced self-assembly method // Journal of the European Ceramic Society, 2010. **30**, 10. P. 2065–2072. https://doi.org/10.1016/j.jeurceramsoc.2010. 04.015
34. *Pal S., Laera A.M., Licciuli A., Catalano M., Taurino A.* Biphase TiO_2 Microspheres with Enhanced Photocatalytic Activity. // Ind. Eng. Chem. Res., 2014. 53. P. 7931–7938.
35. *Yang Y., Wang G., Deng Q., Ng D. H. L., Zhao H.* Microwave-assisted fabrication of nanoparticulate TiO_2 microspheres for synergistic photocatalytic removal of Cr(VI) and methyl orange // ACS Appl. Mater. Interfaces, 2014. **6**. P. 3008–3015.
36. *He Z., Que W.* Surface scattering and reflecting: the effect on light absorption or photocatalytic activity of TiO_2 scattering microspheres // Phys. Chem. Chem. Phys., 2013. **15**. P. 16768–16773.
37. *Tian S., Yang H., Cui M., Shi R., Zhao H., Wang X., Wang X., Zhang L.* Monodisperse rutile TiO_2 nanorod-based microspheres with various diameters: hydrothermal synthesis, formation mechanism and diameter- and crystallinity-dependent photocatalytic properties // Appl. Phys. A., 2011. **104**. P. 149–158.
38. *Liu B., Nakata K., Sakai M., Saito H., Ochiai T., Murakami T., Takagi K., Fujishima A.* Hierarchical TiO_2 spherical nanostructures with tunable pore size, pore volume, and specific surface area: facile preparation and high-photocatalytic performance // Catal. Sci. Techhol., 2012. **2**. P. 1933–1939.
39. *Cao L., Chen D., Wu W.-Q., Tan J. Z. Y., Caruso R. A.* Monodisperse anatase titania microspheres with high-thermal stability and large pore size (80 nm) as efficient photocatalysts // J. Mater. Chem. A., 2017. **5**. P. 3645–3654.
40. *Deng A., Zhu Y.* Synthesis of $TiO_2/SiO_2/Ag/Ag_2O$ and $TiO_2/Ag/Ag_2O$ nanocomposite spheres with photocatalytic performance // Research on Chemical Intermediates, 2018. **44**. P. 4227–4243.
41. *Строюк А.Л., Ермохина Н.И., Коржак А.В., Андрюшина Н.С., Козицкий А.В., Манорик П.А., Ильин В.Г., Пузий А.М., Сапсай В.И., Щербатюк Н.Н.* Фотокаталитические и фотоэлектрические характеристики мезопористых микросфер диоксида титана // Теорет. и эксперим. химия, 2015. **53**, 3. С. 176–184.
42. *Feng Y., Li L., Ge M., Guo C., Wang J., Liu L.* Improved Catalytic Capability of Mesoporous TiO_2 Microspheres and Photodecomposition of Toluene // ACS Appl. Mater. Interfaces, 2010. **2**. P. 3134–3140.
43. *Guo C., Ge M., Li L., Gao G., Feng Y., Wang Y.* Directed Synthesis of Mesoporous TiO_2 Microspheres: Catalysts and Their Photocatalysis for Bisphenol A Degradation // Environ. Sci. Technol., 2010. **44**. P. 419–425.
44. *Xie J., Bian L., Yao L., Hao Y., Wei Y.* Simple fabrication of mesoporous TiO_2 microspheres for photocatalytic degradation of pentachlorophenol // Mater. Lett., 2013. **91**. P. 213–216.
45. *Yanagishita T., Imaizumi M., Toshiaki K., Masuda H.* TiO_2 Hollow Spheres with Nanoporous Structures Fabricated by Anodization of Ti Particles // RSC Adv., 2015. **5**. P. 41830–41834.

46. *Guo C., Xu J., Zhang Y., He Y.* Hierarchical mesoporous TiO_2 microspheres for the enhanced photocatalytic oxidation of sulfonamides and their mechanism // RSC Adv., 2012. **2**. P. 4720–4727.
47. *Naldoni A., Bianchi C.L., Pirola C., Suslick K.S.* Porous TiO_2 microspheres with tunable properties for photocatalytic air purification // Ultrason. Sonochem., 2013. **20**. P. 445–451.
48. *Fang B., Bonakdarpour A., Reilly K., Xing Y., Taghipour F., Wilkinson D. P.* Large-Scale Synthesis of TiO_2 Microspheres with Hierarchical Nanostructure for Highly Efficient Photo Driven Reduction of CO_2 to CH_4 // ACS Appl. Mater. Interfaces, 2014. **6**. P. 15488–15498.
49. *Yuan, S., Sheng, Q., Zhang, J., Yamashita, H., and He D.* Synthesis of thermally stable mesoporous TiO_2 and investigation of its photocatalytic activity // Microporous and Mesoporous Materials, 2008. **110,** (2–3). P. 501–507.
50. *Sibu C.P., Kumar S.R., Mukundan P., Warrier K. G. K.* Structural Modifications and Associated Properties of Lanthanum Oxide Doped Sol–Gel Nanosized Titanium Oxide // Chemistry of Materials, 2002. **14**, 7. P. 2876–2881. https://doi.org/10.1021/cm010966p
51. *Zhang, W. and Pinnavaia, T.J.* Rare Earth Stabilization of Mesoporous Alumina Molecular Sieves Assembled Through an N0I0 Pathway // Chemical Communication, 1998. P. 1185–1186.
52. *Liqiang J., Xiaojun S., Baifu X., Baiqi W., Weimin C., Honggang F.* The preparation and characterization of La doped TiO_2 nanoparticles and their photocatalytic activity // Journal of Solid State Chemistry, 2004. **177**, 10. P. 3375–3382.
53. *Hanaor D.A.H., Sorrell C.C.* Review of the anatase to rutile phase transformation // Journal of Materials Science, 2011. **46**, 4. P. 855–874. http://dx.doi.org/10.1007/s10853-010-5113-0
54. *Milanović M., Nikolić L. M.* Modification of TiO_2 nanoparticles through lanthanum doping and PEG templating // Processing and Application of Ceramics, 2014. **8**, 4. P. 195–202. https://doi.org/10.2298/PAC1404195M
55. *Rebecca E. Olsen, Calvin H. Bartholomew, Baiyu Huang, Brian F. Woodfield*. Synthesis and characterization of pore and stabilized mesoporous anatase titanias // Microporous and Mesoporous materials, 2014. **184**. P. 7–14.
56. *Huang Yu, Cao Jun-Ji, Kang Fei, You Sheng-Jie, Chang Chia-Wei, Wang Ya-Fen.* High Selectivity of Visible-Light-Driven La-doped TiO_2 Photocatalysts for NO Removal // Aerosol and Air Quality Research, 2017. **17**. P. 2555–2565. https://doi.org/10.4209/aaqr.2017.08.0282
57. *Kefeng Xie, Qiangqiang Jia, Yizhe Wang, Wenxue Zhang and Jingcheng Xu.* The Electronic Structure and Optical Properties of Anatase TiO_2 with Rare Earth Metal Dopants from First-Principles Calculations // Materials, 2018. 11. P. 179. https://doi.org/10.3390/ma11020179
58. *Stroyuk O.L., Ermokhina N.I., Korzhak G.V., Andryushina N.S., Shvalagin V.V., Kozytskiy A.V., Manoryk P.A., Barakov R.Y., Kuchmiy S.Y., Shcherbatyuk M., Sapsay V.I., Puziy A.M.* Photocatalytic and photoelectrochemical properties of hierarchical mesoporous TiO_2 microspheres produced using a crown template // Journal of Photochemistry and Photobiology A Chem., 2017. **334**. P. 26–35. https://doi.org/10.1016/j. jphotochem.2016.10.039
59. *Shvalagin V., Ermokhina N., Romanovska N., Barakov R., Manorik P., Sapsay V., Shcherbakov S., Poddubnaya O., Puziy A*. Mesoporous TiO_2 microspheres with improved efficiency for photooxidation of volatile organic compounds // Research on Chemical Intermediates, 2019. **45**, 8. P. 4133–4148. https://dx.doi.org/10.1007/s11164-019-03896-z
60. *Ермохина Н. И., Швалагин В. В., Романовская Н. И., Сидорова Н. А., Манорик П. А., Бараков Р. Ю., Щербатюк М. М., Климчук Д. О., Пузий А. М.* Фотокаталитическая активность мезопористого диоксида титана,

стабилизированного лантаном, при газофазном окислении этанолом // Теорет. и эксперим. химия, 2017. **53**, 6. С. 368–374.

61. *Ermokhina N.I, Shvalagin V.V., Romanovska N.I., Manoryk P.A., Barakov R.Yu., Kompanets M.O.,·Sapsay V.I., Klymchuk D.O., Puziy A.M.* Synthesis and characterization of different binary and ternary phasemixtures of mesoporous nanocrystalline titanium dioxide // SN Applied Sciences, 2021. **3**. P. 491. https://link.springer.com/article/10.1007/s42452-021-04474-y
62. *Раевская А. Е. Коржак А. В. Строюк А. Л., Кучмий С. Я.* Фотокаталитическое выделение водорода из водно-спиртовых сред с участием мезопористого TiO_2 // Теорет. и эксперим. химия, 2009. **45**, 6. С. 331–335.
63. *Ermokhina N.I., Nevinskiy V.A., Manorik P.A., Ilyin V.G., Novichenko V.N., Shcherbatiuk M.M., Klymchuk D.O., Tsyba M.M., Puziy A.M.* Synthesis and characterization of thermally stable large-pore mesoporous nanocrystalline anatase // Journal Solid State Chemistry, 2013. **200**. P. 90– 98. https://doi.org/10.1016/j.jssc.2012.12.034
64. *Korzhak A.V., Ermokhina N.I., Stroyuk A.L., Bukhtiyarov V.K., Raevskaya A.E., Litvin V.I., Kuchmiy S.Y., Ilyin V.G., Manorik P.A.* Photocatalytic hydrogen evolution over mesoporous TiO_2/metal nanocomposites // J. Photochem. Photobiol. A. Chem., 2008. **198**, 2. P. 126–134. http://dx.doi.org/10.1016/j.jphotochem.2008.02.026
65. *Schneider J., Bahnemann D., Ye J., Puma, G. Li., Dionysiou D.D.* Photocatalysis: fundamentals and perspectives. Royal Society of Chemistry, Cambridge, 2016. https://doi.org/10.1039/9781782622338

REFERENCES

1. Nakata K., Fujishima A. TiO_2 photocatalysis: design and applications. *Journal of Photochemistry and Photobiology C: Photochemistry Reviews,* 2012. 13(3): 169–189. https://doi.org/10.1016/j.jphotochemrev.2012. 06.001
2. Pelaez M., Nolan N.T., Pillai S.C., Seery M.K., Falaras P., Kontos A.G., Dunlop P.S.M., Hamilton J.W.J., Byrne J.A., O'Shea K., Entezari M.H., Dionysiou D.D. A review on the visible light active titanium dioxide photocatalysts for environmental applications. *Applied Catalysis B: Environmental.* 2012. **125**: 331–349. https://doi.org/10.1016/j.apcatb. 2012.05.036
3. Tong H., Ouyang S., Bi Y., Umezawa N., Oshikiri M., Ye J. Nanophotocatalytic materials: possibilities and challenges. *Advance Materials*. 2012. 24(2): 229–251. https://doi.org/10.1002/adma.201102752
4. Fresno F., Portela R., Suárez S., Coronado J.M. Photocatalytic materials: recent achievements and near future trends. *Journal of Material Chemistry* A. 2014. 2(9): 2863–2884. https://doi.org/10.1039/C3TA13793G
5. Wang Y., Sun C., Zhao X., Cui B., Zeng Z., Wang A., Liu G., Cui H. The application of nano-TiO_2 photo semiconductors in agriculture. *Nanoscale Research Letters*. 2016. 11(1): 529. http://dx.doi.org/10.1186/s11671-016-1721-1
6. Kumar N., Chauhan N.S., Mittal A., Sharma S. TiO_2 and its composites as promising biomaterials: a review. *BioMetals*. 2018. 31(2): 147–159. https://doi.org/10.1007/s10534-018-0078-6
7. Noman M.T., Ashraf M.A., Ali A. Synthesis and applications of nano-TiO_2: a review. *Environmental Science and Pollution Research.* 2019. 26(4): 3262–3291. https://doi.org/10.1007/s11356-018-3884-z
8. Humayun M., Raziq F., Khan A., Luo W. Modification strategies of TiO_2 for potential applications in photocatalysis: a critical review. *Green Chemistry Letters and Reviews.* 2018. 11(2): 86–102. https://doi.org/10. 1080/17518253.2018.1440324
9. Paul K.K., Giri P.K. Shape tailored TiO_2 nanostructures and their hybrids for advanced energy and environmental applications: a re-

view. *Journal of Nanoscience and Nanotechnology.* 2018. 19(1): 307–331. https://doi.org/10.1166/jnn.2019.15778
10. Dionysiou D.D., Puma G.Li., Ye J., Schneider J., Bahnemann D. Photocatalysis: applications. *Royal Society of Chemistry, Cambridge*. 2016. https://doi.org/10.1039/9781782627104
11. Schneider J., Matsuoka M., Takeuchi M., Zhang J., Horiuchi Y., Anpo M., Bahnemann D.W. Understanding TiO_2 photocatalysis: mechanisms and materials. *Chemical Reviews*. 2014. 114(19): 9919–9986. https://doi.org/10.1021/cr5001892
12. Anpo M., Kamat P.V. Environmentally benign photocatalysts. *Springer*, New York. 2010. https://doi.org/10.1007/978-0-387-48444-0
13. Laura Cano-Casanova, Ana Amorós-Pérez, Maria Angeles Lillo-Ródenas and María del Carmen Román-Martínez. Effect of the preparation method (sol–gel or hydrothermal) and conditions on the TiO_2 properties and activity for propane oxidation. *Materials (Basel)*. 2018. 11(11): 2227. https://doi.org/10.3390/ma11112227
14. Antonelli D.M., Ying J.Y. Synthesis of hexagonally packed mesoporous TiO_2 by a modified sol–gel method. *Angewandte Chemie International Edition in English.* 1995. 34(18): 2014–2017. https://doi.org/10.1002/anie. 199520141
15. Ismail A.A., Bahnemann D.W. Mesoporous titania photocatalysts: preparation, characterization and reaction mechanisms. *Journal of Material Chemistry*. 2011. 21(32):11686. https://doi.org/10.1039/c1jm10407a
16. Kumar A. Different methods used for the synthesis of TiO_2 based nanomaterials: a review. *American Journal of Nano Research and Application*. 2018. 6(1):1. https://doi.org/10.11648/j.nano.20180601.11
17. Shayegan Z., Lee C-S., Haghighat F. TiO_2 photocatalyst for removal of volatile organic compounds in gas phase: a review. *Chemical Engineering Journal*. 2018. 334: 2408–2439. https://doi.org/10.1016/j.cej.2017. 09.153
18. Shen X., Tian B., Zhang J. Tailored preparation of titania with controllable phases of anatase and brookite by an alkalescent hydrothermal route. *Catalysis Today*. 2013. 201: 151–158. https://doi. org/10.1016/j.cattod.2012.04.038
19. Wu M., Lin G., Chen D., Wang G., He D., Feng S., Xu R. Solhydrothermal synthesis and hydrothermally structural evolution of nanocrystal titanium dioxide. *Chemistry of Materials*. 2002. 14(5): 1974–1980. https://doi.org/10.1021/cm0102739
20. Yang X., Konishi H., Xu H., Wu M. Comparative Sol– hydro(solvo)thermal synthesis of TiO_2 nanocrystals. *European Journal of Inorganic Chemistry*. 2006. (11): 2229–2235. https://doi.org/10.1002/ejic.200500855
21. Wang C-C., Ying J.Y. Sol–gel synthesis and hydrothermal processing of anatase and rutile titania nanocrystals. *Chemistry of Materials*. 1999. 11(11): 3113–3120. https://doi.org/10.1021/cm990180f
22. Castrejon-Sanchez V., Lopez R., Ramon-Gonzalez M., Enriquez-Perez A., Camacho-Lopez M., Villa-Sanchez G. Annealing control on the anatase/rutile ratio of nanostructured titanium dioxide obtained by sol–gel. *Crystals*. 2018. 9(1): 22. https://doi.org/10. 3390/cryst9010022
23. Bamne J., Sharma P.K., Haque F.Z. Effect of solvent mixing and calcination temperature on the growth of TiO_2 nanoparticle prepared via sol–gel method. *Materials Focus*. 2018. 7(2): 232–241. https://doi.org/10.1166/mat.2018.1502
24. Luttrell T., Halpegamage S., Tao J., Kramer A., Sutter E., Batzill M. Why is anatase a better photocatalyst than rutile? Model studies on epitaxial TiO_2 films. *Scientific Reports*. 2015. 4(1): 4043. https://doi.org/10.1038/srep04043
25. Sheikhnejad-Bishe O., Zhao F., Rajabtabar-Darvishi A., Khodadad E., Mostofizadeh A., Huang Y. Influence of temperature and surfactant on the photocatalytic performance of TiO_2 Nanoparticles. *International Journal of*

Electrochemical Science. 2014. 9(8): 4230–4240.
26. Masolo E., Meloni M., Garroni S., Mulas G., Enzo S., Baro M., Rossinyol E., Rzeszutek A., Herrmann-Geppert I., Pilo M. Mesoporous titania powders: the role of precursors, ligand addition and calcination rate on their morphology, crystalline structure and photocatalytic activity. *Nanomaterials*. 2014. 4(3): 583–598. https://doi.org/10.3390/nano4030583
27. Yue Y., Gao Z. Synthesis of mesoporous TiO_2 with a crystalline framework. *Chemical Communications*. 2000. 18:1755–1756. https://doi.org/10.1039/b004124f
28. Byrappa K., Adschiri T. Hydrothermal technology for nanotechnology. *Progress in Crystal Growth and Characterization of Materials*. 2007. 53(2): 117–166. https://doi.org/10.1016/j.pcrysgrow.2007.04.001
29. Luis A.M., Neves M.C., Mendonca M.H., Monteiro O.C. Influence of calcination parameters on the TiO_2 photocatalytic properties. *Materials Chemistry and Physics*. 2011. 125(1–2): 20–25. https://doi.org/10.1016/j.matchemphys.2010.08.019
30. Agarwala P., Makkar P., Sharma S., Garg R. The effect of heat treatment of TiO_2 nanoparticles on photovoltaic performance of fabricated DSSCs. *Journal of Materials Engineering and Performance*. 2014. 23(10): 3703–3709. https://doi.org/10.1007/s11665-014-1131-4
31. Fattakhova-Rohlfing D., Zaleska A., Bein T. Three-Dimensional Titanium Dioxide. *Nanomaterials*, *Chem. Rev*. 2014. 114: 9487–9558.
32. Chen L-H., Li X-Y., Deng Z., Hu Z-Y., Rooke J.C., Krief A., Yang X-Y., Su B-L. Hydrothermal and surfactant treatment to enhance the photocatalytic activity of hierarchically meso – macroporous titanias. *Catalysis Today*. 2013. 212: 89–97. https://doi.org/10.1016/j.cattod. 2012.07.021
33. Hung I-M., Wang Y., Huang C-F., Fan Y-S., Han Y-J, Peng H-W. Effects of templating surfactant concentrations on the mesostructure of ordered mesoporous anatase TiO_2 by an evaporation-induced self-assembly method. *Journal of the European Ceramic Society*. 2010. 30(10): 2065–2072. https://doi.org/10.1016/j.jeurceramsoc.2010. 04.015
34. Pal S., Laera A.M., Licciuli A., Catalano M., Taurino A. Biphase TiO_2 Microspheres with Enhanced Photocatalytic Activity. *Ind. Eng. Chem. Res*. 2014. 53: 7931–7938.
35. Yang Y., Wang G., Deng Q., Ng D. H. L., Zhao H. Microwave-assisted fabrication of nanoparticulate TiO_2 microspheres for synergistic photocatalytic removal of Cr(VI) and methyl orange. *ACS Appl. Mater. Interfaces*. 2014. 6: 3008–3015.
36. He Z., Que W., Surface scattering and reflecting: the effect on light absorption or photocatalytic activity of TiO_2 scattering microspheres. *Phys. Chem. Chem. Phys*. 2013. 15: 16768–16773.
37. Tian S., Yang H., Cui M., Shi R., Zhao H., Wang X., Wang X., Zhang L. Monodisperse rutile TiO_2 nanorod-based microspheres with various diameters: hydrothermal synthesis, formation mechanism and diameter- and crystallinity-dependent photocatalytic properties. *Appl. Phys*. A. 2011. 104: 149–158.
38. Liu B., Nakata K., Sakai M., Saito H., Ochiai T., Murakami T., Takagi K., Fujishima A. Hierarchical TiO_2 spherical nanostructures with tunable pore size, pore volume, and specific surface area: facile preparation and high-photocatalytic performance. *Catal. Sci. Techhol*. 2012. 2: 1933–1939.
39. Cao L., Chen D., Wu W.-Q., Tan J. Z. Y., Caruso R. A. Monodisperse anatase titania microspheres with high-thermal stability and large pore size (80 nm) as efficient photocatalysts. *J. Mater. Chem*. A. 2017. 5: 3645–3654.
40. Deng A., Zhu Y. Synthesis of $TiO_2/SiO_2/Ag/Ag_2O$ and $TiO_2/Ag/Ag_2O$ nanocomposite spheres with photocatalytic performance. *Research on Chemical Intermediates*. 2018. 44: 4227–4243.
41. Stroyuk A.L., Ermokhina N.I., Korzhak A.V., Andryushina N.S., Kozytskiy A.V., Manorik

P.A., Ilyin V.G., Puziy A.M., Sapsai V.I., Shcherbatyuk N.N. Photocatalytic and photoelectrochemical characteristics of mesoporous titanium dioxide microspheres. *Theoret. and Experim. Chemistry*. 2015. 51(3): 183–190. https://doi.org/10.1007/s11237-015-9414-x

42. Feng Y., Li L., Ge M., Guo C., Wang J., Liu L. Improved Catalytic Capability of Mesoporous TiO_2 Microspheres and Photodecomposition of Toluene. *ACS Appl. Mater. Interfaces*. 2010. 2: 3134–3140.
43. Guo C., Ge M., Li L., Gao G., Feng Y., Wang Y. Directed Synthesis of Mesoporous TiO_2 Microspheres: Catalysts and Their Photocatalysis for Bisphenol A Degradation. *Environ. Sci. Technol*. 2010. 44: 419–425.
44. Xie J., Bian L., Yao L., Hao Y., Wei Y. Simple fabrication of mesoporous TiO_2 microspheres for photocatalytic degradation of pentachlorophenol. *Mater. Lett.* 2013. 91: 213–216.
45. Yanagishita T., Imaizumi M., Toshiaki K., Masuda H. TiO_2 Hollow Spheres with Nanoporous Structures Fabricated by Anodization of Ti Particles. *RSC Adv.* 2015. 5: 41830–41834.
46. Guo C., Xu J., Zhang Y., He Y. Hierarchical mesoporous TiO_2 microspheres for the enhanced photocatalytic oxidation of sulfonamides and their mechanism. *RSC Adv.* 2012. 2: 4720–4727.
47. Naldoni A., Bianchi C.L., Pirola C., Suslick K.S. Porous TiO_2 microspheres with tunable properties for photocatalytic air purification. *Ultrason. Sonochem.* 2013. 20: 445–451.
48. Fang B., Bonakdarpour A., Reilly K., Xing Y., Taghipour F., Wilkinson D. P. Large-Scale Synthesis of TiO_2 Microspheres with Hierarchical Nanostructure for Highly Efficient Photo Driven Reduction of CO_2 to CH_4. *ACS Appl. Mater. Interfaces*. 2014. 6: 15488–15498.
49. Yuan, S., Sheng, Q., Zhang, J., Yamashita, H., and He D. Synthesis of thermally stable mesoporous TiO_2 and investigation of its photocatalytic activity. *Microporous and Mesoporous Materials*. 2008. 110 (2–3): 501–507.
50. Sibu C.P., Kumar S.R., Mukundan P., Warrier K. G. K. Structural Modifications and Associated Properties of Lanthanum Oxide Doped Sol–Gel Nanosized Titanium Oxide // *Chemistry of Materials.* 2002, 14, (7): 2876–2881. https://doi.org/10.1021/cm010966p
51. Zhang, W. and Pinnavaia, T.J. Rare Earth Stabilization of Mesoporous Alumina Molecular Sieves Assembled Through an N0I0 Pathway. *Chemical Communication*. 1998. 1185–1186.
52. Liqiang J., Xiaojun S., Baifu X., Baiqi W., Weimin C., Honggang F. The preparation and characterization of La doped TiO_2 nanoparticles and their photocatalytic activity. *Journal of Solid State Chemistry*. 2004. 177(10): 3375–3382.
53. Hanaor D.A.H., Sorrell C.C. Review of the anatase to rutile phase transformation // *Journal of Materials Science.* 2011. 46(4): 855-874. http://dx.doi.org/10.1007/s10853-010-5113-0
54. Milanović M., Nikolić L. M. Modification of TiO_2 nanoparticles through lanthanum doping and PEG templating // *Processing and Application of Ceramics*. 2014. 8(4): 195–202. https://doi.org/10.2298/PAC1404195M
55. Rebecca E. Olsen, Calvin H. Bartholomew, Baiyu Huang, Brian F. Woodfield. Synthesis and characterization of pore and stabilized mesoporous anatase titanias. *Microporous and Mesoporous materials*. 2014. 184: 7–14.
56. Huang Yu, Cao Jun-Ji, Kang Fei, You Sheng-Jie, Chang Chia-Wei, Wang Ya-Fen. High Selectivity of Visible-Light-Driven La-doped TiO_2 Photocatalysts for NO Removal. *Aerosol and Air Quality Research*. 2017. 17: 2555–2565. https://doi.org/10.4209/aaqr.2017.08.0282
57. Kefeng Xie, Qiangqiang Jia, Yizhe Wang, Wenxue Zhang and Jingcheng Xu. The Electronic Structure and Optical Properties of Anatase TiO_2 with Rare Earth Metal Dopants from First-Principles Calculations. *Materials* – 2018. 11: 179. https://doi.org/10.3390/ma11020179
58. Stroyuk O.L., Ermokhina N.I., Korzhak G.V.,

Andryushina N.S., Shvalagin V.V., Kozytskiy A.V., Manoryk P.A., Barakov R.Y., Kuchmiy S.Y., Shcherbatyuk M., Sapsay V.I., Puziy A.M. Photocatalytic and photoelectrochemical properties of hierarchical mesoporous TiO_2 microspheres produced using a crown template. *Journal of Photochemistry and Photobiology* A Chem. 2017. 334: 26–35. https://doi.org/10.1016/j. jphotochem.2016.10.039

59. Shvalagin V., Ermokhina N., Romanovska N., Barakov R., Manorik P., Sapsay V., Shcherbakov S., Poddubnaya O., Puziy A. Mesoporous TiO_2 microspheres with improved efficiency for photooxidation of volatile organic compounds. *Research on Chemical Intermediates*. 2019. 45(8): 4133–4148. https://dx.doi.org/10.1007/s11164-019-03896-z
60. Ermokhina N.I., Shvalagin V.V., Romanovska N.I., Sydorova N.A., Manoryk P.A., Barakov R.Y., Shcherbatyuk M.M., Klymchuk D.O., Puziy A.M. Photocatalytic activity of mesoporous titanium dioxide stabilized with lanthanum in the gas-phase oxidation of ethanol. *Theoret. and Experim. Chemistry*. 2018. 53(6): 395–401. https://doi.org/10.1007/s11237-018-9537-y
61. Ermokhina N.I, Shvalagin V.V., Romanovska N.I., Manoryk P.A., Barakov R.Yu., Kompanets M.O.,·Sapsay V.I., Klymchuk D.O., Puziy A.M.. Synthesis and characterization of different binary and ternary phasemixtures of mesoporous nanocrystalline titanium dioxide. *SN Applied Sciences*. 2021. 3: 491. https://doi.org/10.1007/s42452-021-04474-y
62. Raevskaya A.E., Korzhak A.V., Stroyuk A.L., Kuchmii S.Ya. Photocatalytic production of hydrogen from water-alcohol media with the participation of mesoporous TiO_2. *Theoret. and Experim. Chemistry*. 2009. 45(6): 343–348.
63. Ermokhina N.I., Nevinskiy V.A., Manorik P.A., Ilyin V.G., Novichenko V.N., Shcherbatiuk M.M., Klymchuk D.O., Tsyba M.M., Puziy A.M. Synthesis and characterization of thermally stable large-pore mesoporous nanocrystalline anatase. *Journal Solid State Chemistry*. 2013. 200: 90–98. https://doi.org/10.1016/j.jssc.2012.12.034
64. Korzhak A.V., Ermokhina N.I., Stroyuk A.L., Bukhtiyarov V.K., Raevskaya A.E., Litvin V.I., Kuchmiy S.Y., Ilyin V.G., Manorik P.A. Photocatalytic hydrogen evolution over mesoporous TiO_2/metal nanocomposites. *J. Photochem. Photobiol. A. Chem.* 2008. 198 (2): 126–134. http://dx.doi.org/10.1016/j.jphotochem.2008.02.026
65. Schneider J., Bahnemann D., Ye J., Puma G. Li., Dionysiou D.D. Photocatalysis: fundamentals and perspectives. *Royal Society of Chemistry*, Cambridge. 2016. https://doi.org/10.1039/9781782622338

Стаття надійшла 11.05.2022.

UDC 541.49. doi: 10.33609/2708-129X.88.04.2022.113-122

DETERMINATION OF POLYLIGAND COMPLEXES OF COBALT (II) WITH CITRATE AND PYROPHOSPHATE IONS

V. M. Nikitenko, Yu. S. Yapontseva*, V. S. Kublanovsky

V. I. Vernadsky Institute of General and Inorganic Chemistry of the NAS of Ukraine,
Acad. Palladina av. 32/34, 03142 Kyiv, Ukraine
**e-mail: juliya_yap@ukr.net*

In the work it is shown by the spectrophotometry method that depending on the concentration ratio of ligands $[PPi^{4-}]/[Cit^{3-}]$ in the pyrophosphate-citrate electrolyte, cobalt (II) ions form not only citrate $[Co(Cit)_2]^{4-}$ and pyrophosphate $[Co(PPi)_2]^{6-}$, but also polyligand complexes $[Co(PPi)_m(Cit)_n]^{+2-(4m+3n)}$. The composition of polyligand complexes $[Co(PPi)Cit]^{5-}$ was determined, and the equilibrium constant of the reaction of their formation and the constant of their stability were calculated ($p\beta = 8.47$). The dependence of the degree of formation of citrate, polyligand, and pyrophosphate complexes of cobalt (II) in the pyrophosphate-citrate electrolyte on the logarithm of the ratio of equilibrium concentrations of ligands is calculated.

Keywords: cobalt (II), polyligand complex, composition, stability constant, spectrophotometry.

INTRODUCTION. The structure of metal and alloy coatings deposited from complex electrolytes, the uniformity of their distribution on the sample surface are determined by the magnitude of the overvoltage of the cathodic process – a preliminary chemical reaction and the magnitude of activation energy of electrochemically active complexes (EAC). Overvoltage is the most important characteristic of the electrode process, as it affects the morphology, structure and functional properties of metal and alloy coatings. In the development of technological processes for coating from complex electrolytes not only the composition and stability of coordination compounds, but also the geometric structure and electronic configuration of the EAC are important. These factors ultimately determine the rate and mechanism of electrode processes.

Monoligand and polyligand (pyrophosphate, citrate and pyrophosphate-citrate) electrolytes have been widely used for the deposition of coatings of binary and ternary alloys of refractory metals (Mo, W and Re) with iron subgroup metals (Fe, Co, Ni), in particular cobalt. [1].

A pyrophosphate-citrate electrolyte was chosen as the study object because it allows the deposition of high-quality coatings of molybdenum, tungsten, and rhenium alloys with

cobalt with a higher current efficiency than monoligand electrolytes [1–9]. These alloys have valuable physicochemical and operational properties [2], which make them indispensable in practical use.

Determining the ionic composition in the bulk electrolyte for polyligand systems such as electrolyte containing cobalt (II) ions and two ligands simultaneously – citrate (Cit^{3-}) and pyrophosphate (PPi^{4-}) is an important and challenging task. Information on the composition of complex compounds in the bulk of pyrophosphate-citrate electrolyte, kinetics and mechanism of deposition of alloys will allow to control the relevant processes of their production, and hence the structure and functional properties of the resulting coatings.

The aim of the work aim is to establish the composition and determine the stability constant of polyligand complexes of cobalt (II) with Cit^{3-} and PPi^{4-} ions by spectrophotometric method and to study the effect of the ionic composition in the electrolyte on the ratio of ligand equilibrium concentrations.

Cobalt (II) ions form with Cit^{3-} and PPi^{4-} ions, depending on the solution pH and the equilibrium concentration of ligands, protonated and unprotonated pyrophosphate $[CoHPPi]^{-}$, $[Co(HPPi)_2]^{4-}$, $[Co(HPPi)(PPi)]^{5-}$, $[CoPPi]^{2-}$, $[Co(PPi)_2]^{6-}$ and citrate $[CoH_2Cit]^{+}$, [CoHCit], $[CoCit]^{-}$, $[Co(Cit)_2]^{4-}$ complexes [10, 11]. Polymeric, polynuclear complexes of cobalt (II) with citrate of the compositions $[Co_4(Cit)_4\ [Co(H_2O)_5]_2^{4-}$, $K_3[Co_2(Cit)_2(H_2O)_4]\cdot 6H_2O$ were synthesized and isolated in solid the state [12, 13] and others, which have magnetic properties [13] and biocompatibility [14, 15]. The thermodynamics of protonated cobalt (II) citrate complexes formation have also been studied [16]. There are no data on the possibility of formation of polyligand complexes of cobalt (II) with Cit^{3-} and PPi^{4-} ions in the pyrophosphate-citrate electrolyte, their composition and stability constant are not available in the literature.

Spectrophotometry is one of the most pretentious methods for determining the composition and stability constants of colored complex compounds. General characteristics of methods for determining the composition and stability constants of metal complexes from spectrophotometric measurements, their advantages, scope, limitations and disadvantages are detailed in the monograph of A.K. Babko [17].

The spectrophotometric study of the formation of polyligand complexes of cobalt (II) with Cit^{3-} and PPi^{4-} ions involves significant difficulties, because along with them in the system under study, depending on the pH of the solution, there may also exist monoligand protonated and unprotonated citrate and pyrophosphate complexes of Co (II). The distribution of complexes in the bulk electrolyte in this case strongly depends on the equilibrium concentration of metal ions, the ratio of the equilibrium concentrations of free ligands and the pH of the solution.

Since Cit^{3-} and PPi^{4-} ions are anions of weak acids, their equilibrium concentrations in the test solution depend on the pH of the solution and can be determined by the pH-potentiometric method. Therefore, when conducting spectrophotometric studies it is necessary to maintain the optimal and constant concentration of hydrogen ions (pH = const) to form complex ions of constant composition at a certain ratio of the concentrations of the main components of the investigated solution $C_{Co^{2+}}:C_{PPi^{4-}}$ and $C_{Co^{2+}}:C_{Cit^{3-}}$ = const.

The values of the equilibrium concentrations of free ligands $[PPi]^{4-}$ and $[Cit]^{3-}$ were determined from the spectrophotometric studies, considering their total concentrations and the pH according to the equation (1) [18, 19]:

$$[L]^{m-} = \frac{C_{H_mL} - n^*(C_{Co^{2+}} - [Co]^{2+})}{1 + \sum_{i=1}^{i=4} K_i [H^+]^i}, \quad (1)$$

where $C_{HmL,}$ $[L]^{m-}$ are the total and equilibrium concentrations of ligands (citrate and pyrophosphate) in the test solution (mol·l^{-1}) respectively; C_{Co}^{2+} and $[Co]^{2+}$ are the total and equilibrium concentrations of cobalt (II) ions in the test solution (mol·l^{-1}) respectively; n^* is the average coordination number of pyrophosphate and citrate complexes formed in the test solution; K_i is the general stability constants of citrate and pyrophosphate ions ($pK_1 = 5.68$; $pK_2 = 10.03$; $pK_3 = 12.90$ i $pK_1 = 8.30$; $pK_2 = 14.30$; $pK_3 = 17.00$; $pK_4 = 19.50$) [20].

The equilibrium concentrations of free ligands $[Cit]^{3-}$ and $[PPi]^{4-}$, determined by spectrophotometric studies conditions based on their total concentrations, mol·l^{-1}: $C_{Co}^{2+} = 0.01$; $C_{PPi}^{4-} = 0.05$; $C_{Cit}^{3-} = 0.05$ at the solution pH 9.0 according to equation (1) [18, 19] are $3.0 \cdot 10^{-2}$ and $2.5 \cdot 10^{-2}$ ($n^* = 2$); $4.0 \cdot 10^{-2}$ and $3.3 \cdot 10^{-2}$ ($n^* = 1$),respectively. The ratio of free ligand equilibrium concentrations $[PPi]^4 : [Cit]^{3-}$ in a pyrophosphate-citrate electrolyte at a pH of 9.0 practically does not change, that is $[Cit]^{3-} / [PPi]^{4-} = 1.2$ at $1 \le n^* \le 2$.

The relation between the absorption and composition of the studied solution in the ideal case described by the Lambert – Bouguer – Beer law [21, 22] is:

$$D = l \cdot \sum \varepsilon_i C_i, \quad (2)$$

where D is the absorption of the solution; l is the thickness of the absorbing layer (cuvette length, cm); ε_i is the molar absorption coefficient of the i-th particle at a given wavelength λ and temperature; C_i is the molar concentration of the absorbing particle.

The main requirement for the spectrophotometric method is that the absorption of the solution *D,* property of the measured system must be, according to the Lambert – Beer law, a strictly linear function of the molar concentration of absorbing complexes C_i. In addition, the colored complex should have high stability (stability constant), constant composition (in a wide range of ratios of the concentrations of the main components and pH of the solution), as well as high color intensity per 1 g mole of the substance (molar absorption coefficient ε_i) [23, 24].

EXPERIMENT AND DISCUSSION OF THE RESULTS. Composition of the studied solutions, mol·1^{-1}: $Co^{2+} = 0.01$; $PPi^{4-} = 0.05$; $Cit^{3-} = 0.05$; $Na_2SO_4 = 0.30$; pH 9.0. Analytical grade reagents were used to prepare electrolytes. The pH of the studied solutions was corrected on an electronic pH meter (pH-150MI) using NaOH and Na_2SO_4.

The absorption spectra of the studied solutions of cobalt (II) complexes were recorded on a UV-VIS Spectrophotometer UV mini 1240 (Shimadzu) in a 1 cm cuvette.

The possibility of the formation of polyligand complexes of cobalt (II) from Cit^{3-} and PPi^{4-} ions was studied by the method of isomolar series [17, 21, 25] at a constant ionic strength of the solution (0.3 mol·1^{-1} Na_2SO_4) using initial solutions with a constant ratio of the concentrations of ions $C_{Co}^{2+} : C_{Cit}^{3-} = 1 : 5$ and $C_{Co}^{2+} : C_{PPi}^{4-} = 1 : 5$. The use of this solution is due to the fact that at pH 9.0, in contrast to the citrate solution with $C_{Co}^{2+} : C_{Cit}^{3-} = 1 : 2$ it is

impossible to experimentally prepare an initial pyrophosphate solution with a constant concentration ratio of $C_{Co}^{2+} : C_{PPi}^{4-} = 1 : 2$ because under these conditions, partial hydrolysis of the cobalt(II) salt and, as a result, clouding of the solution take place, since the solubility product of cobalt(II) hydroxide $SP(Co(OH)_2) = 1{,}8 \cdot 10^{-18}$ [26]; the instability constant K of $[Co(PPi)_2]^{6-}$ pyrophosphate complexes is $1.8 \cdot 10^{-9}$ [10]; the total concentration of cobalt (II) ions in the test solution is 0.01 mol·l^{-1}.

To establish the composition and determine the stability constant of the polyligand complexes of cobalt (II) formed in the system under study, the absorption of the solution D, as a function of its composition was determined by the method of isomolar series (Ostromyslensky Zhoba method) [17, 21, 25]. A series of solutions was prepared by mixing initial solutions with a constant concentration ratio of $C_{Co}^{2+} : C_{Cit}^{3-} = 1 : 5$ (x ml) and $C_{Co}^{2+} : C_{PPi}^{4-} = 1 : 5$ ($10 - x$) ml at a constant total concentration of cobalt (II) ions ($C_{Co}^{2+} = 0.01$ mol·l^{-1}) and wavelength λ. In this case, the total concentration of metal ions in the studied solutions remains constant, and the ratio of the total concentrations of ligands $C_{PPI}^{4-} : (C_{PPi}^{4-} + C_{Cit}^{3-})$ decreases from 1 to 0. The ratio of the total concentrations of ligands $C_{Cit}^{3-} : (C_{PPi}^{4-} + C_{Cit}^{3-})$ increases from 0 to 1. The ratios of the equilibrium concentrations of free ligands $[PPi]^{4-}:([PPi]^{4-} + [Cit]^{3-})$ and $[Cit]^{3-}:([Cit]^{3-} + [PPi]^{4-})$ change in a similar way.

The absorption spectra of the studied solutions are shown in Fig. 1. The presence of two isosbestic points on the absorption curves at the wavelengths λ = 592 and 632 nm allows us to assume that there are three complex compounds in the solution under study, namely: citrate $[Co(Cit)_2]^{4-}$, pyrophosphate $[Co(PPi)_2]^{6-}$ and polyligand complexes of cobalt (II). At the isosbestic point (λ = 592 nm), as can be seen from Fig. 1, two complex compounds are in equilibrium: pyrophosphate $[Co(PPi)_2]^{6-}$ (curve 1) and polyligand $[Co(PPi)_m(Cit)_n]^{+2-(4m+3n)}$ (curves 2–6) cobalt(II) complexes. Citrate complexes $[Co(Cit)_2]^{4-}$ do not take part in the equilibrium, since curve 7 does not pass through this isosbestic point (λ = 592 nm).

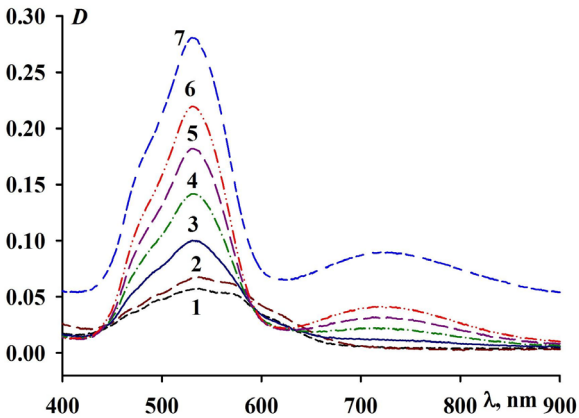

Fig. 1. Absorption spectra in pyrophosphate-citrate electrolyte obtained by the isomolar series method at pH 9.0, a concentration of cobalt (II) ions of 0.01 mol·l^{-1} with the ratio of concentrations $C_{PPi}^{4-} : C_{Cit}^{3-} = 10 : 0$ (1); 9 : 1 (2); 7 : 3 (3); 5 : 5 (4); 3 : 7 (5); 1 : 9 (6); 0 : 10 (7).

Since $[Co(Cit)_2]^{4-}$ citrate complexes do not take part in the formation of polyligand complexes $[Co(PPi)_m(Cit)_n]^{+2-(4m+3n)}$, the equilibrium between the latter and pyrophosphate complexes $[Co(PPi)_2]^{6-}$ is described by the equation:

$$[Co(PPi)_2]^{6-} + [Cit]^{3-} \leftrightarrow [Co(PPi)Cit]^{5-} + [PPi]^{4-}. \quad (3)$$

Therefore, the equilibrium constant K_r of the reaction for the formation of polyligand complexes of cobalt (II) is:

$$K_r = \beta / \beta'_2, \quad (4)$$

where β and β'_2 are the stability constants of polyligand and pyrophosphate complexes $[Co(PPi)_2]^{6-}$, respectively.

It should be noted that the interpretation of spectrophotometric data for the systems under study, in which three or more complex compounds are formed, can be ambiguous [26], since the error in determining the stability constants of the corresponding complexes increases. In this case, the determination of the stability constants of the complexes formed in the system under study from spectrophotometric data must be carried out at a wavelength corresponding to the isosbestic point in absorption spectra, at which the extinction coefficients of all absorbing species are equal ($\varepsilon_1 = \varepsilon_2 = \ldots = \varepsilon_n = \varepsilon^*$) [26].

The results of the analysis of spectrophotometric data are shown in Fig. 2 at the wavelengths λ = 500 and 540 nm in the coordinates: $D = f\,[\,C_{PPi}^{4-}] / [C_{PPi}^{4-} + C_{Cit}^{3-})$ (curves 1, 2) and $D = f\,(C_{Cit}^{3-} / (C_{Cit}^{3-} + C_{PPi}^{4-})$ (curves 3, 4) [21, 25], where D is the absorption of the test solution, C_{PPi}^{4-} and C_{Cit}^{3-} are the total concentrations of ligands. The linear plots indicate the formation of stable polyligand complexes of cobalt (II) with Cit^{3-} and PPi^{4-} ions in the system under study. The abscissa of the point of maximum absorption x_{max} does not depend on the wavelength $\lfloor$ = 500 (curves 1, 3) and 540 nm (curves 2, 4) and is given by:

$$X_{max} = C_{PPi}^{4-} /(C_{PPi}^{4-} + C_{Cit}^{3-}) = \\ = n /(n + m) = 0.5. \qquad (5)$$

This is consistent with the data [21] that when a polyligand (mixed) complex with the composition MLX is formed by the reaction:

$$ML_2 + MX_2 \leftrightarrow 2\,MLX, \qquad (6)$$

the partial mole fraction of each of the complexes ML_2 and MX_2 is 0.50 since $\alpha_1 + \alpha_2 = 1$.

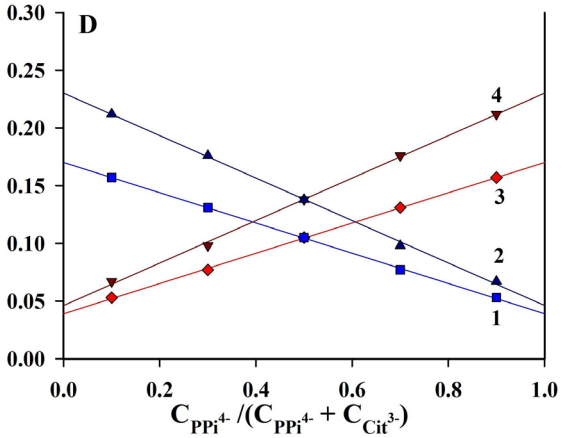

Fig. 2. Absorption of isomolar series in a pyrophosphate-citrate electrolyte at pH 9.0 and wavelengths λ = 500 nm (curves *1*, *3*) and 540 nm (curves *2*, *4*) and the concentration of cobalt ions in the investigated solutions $C_{Co}^{2+} = 0.01$ mol·l^{-1}.

The obtained data (Fig. 2) make it possible to determine the composition of the cobalt (II) polyligand complexes formed under the experimental conditions. The maximum coordination numbers m and n for the polydentate ligands PPi^{4-} and Cit^{3-} of cobalt (II) polyligand complex formed in the system under study, as follows from Fig. 2 and equation (5), are equal to m = n = 1. Thus, polyligand complexes $[Co(PPi)Cit]^{5-}$ are formed in the pyrophosphate–citrate electrolyte at pH 9.0.

The composition of the cobalt (II) polyligand complexes formed in the system under study under given conditions and their stability constant were also determined by the equilibrium shift method [17]. We denote the maximum absorption of the solution under study at the corresponding wavelength λ = 500 nm by D_o, and the optical density of the solution at certain ratios of equilibrium concentrations of ligands $[PPI]^{4-} / [Cit]^{3-}$ until almost complete binding of the central ion into a colored polyligand complex D_x. Since the

optical density of the solution by D_x is proportional to the concentration of the colored complex $[Co(PPi)_m(Cit)_n]^{+2-(4m+3n)}$, the ratio is $[Co(PPi)_m(Cit)_n]^{+2-(4m+3n)} / [Co(PPi)_2]^{6-} = D_x / (D_o - D_x)$. So, from the plots of $\lg D_x / (D_o - D_x) = f(\lg [PPi]^{4-}/ [Cit]^{3-})$ (Fig. 3a, curve 1) and $\lg D_x / (D_o - D_x) = f(\lg [Cit]^{3-}/ [PPi]^{4-})$ (Fig. 3a, curve 2) it is possible to establish the composition of the cobalt (II) polyligand complexes that are formed in the studying system at pH 9.0 and their stability constant.

The plots of $\lg D_x/(D_o - D_x) = f(\lg [PPi]^{4-}/ [Cit]^{3-})$ (Fig. 3a, curve 1) and $\lg D_x/(D_o - D_x) = f(\lg [Cit]^{3-}/[PPi]^{4-})$ (Fig. 3a, curve 2) are rectilinear; the abscissa of the intersection point of them $\lg ([PPi]^{4-}/ [Cit]^{3-}) = 0$. This indicates that the molar ratio of the equilibrium concentrations of polydentate ligands $[PPi]^{4-}/ [Cit]^{3-}$ in the polyligand complex $[Co(PPi)_m(Cit)_n]^{+2-(4m+3n)}$ is 1, i.e. m=n=1 . The ratio $[Cit]^{3-}/ [PPi]^{4-}$, as can be seen from Fig. 3a, curve 2 is 1. Thus, polyligand complexes $[Co(PPi)Cit]^{5-}$ are formed in the system under study at pH 9.0. The slope of the straight line $\lg D_x/(D_o-D_x) = f(\lg [PPi]^{4-}/[Cit]^{3-})$ (Fig. 3a, curve 1) is –0.4886 and is equal to the logarithm of the equilibrium constant *K*r of the reaction of formation of polyligand complexes $[Co(PPi)Cit]^{5-}$. The value of the equilibrium constant *K*r calculated from equation (3) is 0.3246.

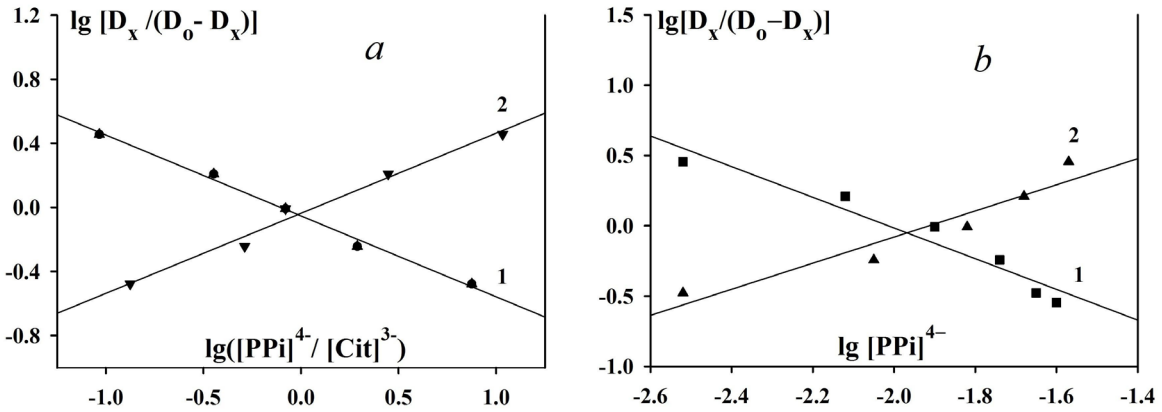

Fig. 3. Dependences $\lg D_x / (D_o - D_x)$ obtained by the method of equilibrium shift in the studied system at pH 9.0, the concentration of ions C_{Co}^{2+} – 0.01 mol·l^{-1}, the wavelength λ = 500 nm on $\lg([PPi]^{4-}: [Cit]^{3-})$ (Fig. 3a, (1)); on $\lg([Cit]^{3-}: [PPi]^{4-})$ (Fig. 3a, (2)); on $\lg[PPi]^{4-}$ (Fig. 3b, (1)) and on $\lg[Cit]^{3-}$ (Fig. 3b, (2)).

The value of the stability constant β of $[Co(PPi)Cit]^{5-}$ polyligand complexes calculated by the equilibrium shift method [17] using experimental data (Fig. 3a) according to equation (4) is $1.80 \cdot 10^8$ (pβ = 8.26).

The composition of cobalt (II) polyligand complexes, and not only the ratio of coordination numbers m/n, was determined from spectrophotometric data (Fig. 1) by the equilibrium shift method [17]; plots of $\lg D_x / (D_o - D_x) = f(\lg [PPi]^{4-})$ (Fig. 3b, curve 1) and $\lg D_x / (D_o - D_x) = f(\lg [Cit]^{3-})$ (Fig. 3b, curve 2) obtained from the spectrophotometric data (Fig. 1) by the equilibrium shift method in the system under study at pH 9.0, the total concentration of C_{Co}^{2+} ions – 0.01 mol·l^{-1}, and the wavelength λ = 500 nm (Fig. 3b) are shown in Fig. 3b.

The slope of the straight line $\lg D_x/(D_o-D_x)$

$= f(\lg [PPi]^{4-})$ (Fig. 3b, curve 1) at $[Cit]^{3-} \to 0$ is equal to the coordination number m of the polyligand complex for $[PPi]^{4-}$ ions and is 1.07:

$$\lim \frac{\partial \lg[D_x/(D_0 - D_x)]}{\partial \lg[P_2O_7]^{4-}} = m. \qquad (7)$$

The value of the coordination number n, calculated from the slope of the straight line $\lg D_x / (D_o - D_x) = f(\lg [Cit]^{3-})$ at $[PPi]^{4-} \to 0$, is 0.96. The obtained values of the coordination numbers m and n (m=n=1) indicate the formation of $[Co(PPi)Cit]^{5-}$ polyligand complexes in the pyrophosphate–citrate electrolyte at pH 9.0.

The composition of $[Co(PPi)Cit]^{5-}$ polyligand complexes in a pyrophosphate–citrate electrolyte was confirmed by the Newman and Hume method [27]. This method is one of the most reliable methods for determining the composition of polyligand complexes and their formation constants [25]. The equilibrium constant *Kr* of reaction (3) for the formation of $[Co(PPi)Cit]^{5-}$ polyligand complexes in the system under study at pH 9.0 calculated by the Newman and Hume method (Fig. 4a) according to the equation:

$$D = C_{Co} \cdot \varepsilon_{Cit\text{-}PPi} - 1/K_r[(D - C_{Co} \cdot \varepsilon_{PPi}) \cdot ([PPi]^{4-}/[Cit]^{3-}), \qquad (8)$$

where $\varepsilon_{Cit\text{-}PPi}$ and ε_{PPi} are the molar absorption coefficients of the polyligand and pyrophosphate complexes of cobalt (II), respectively, is 0.5755.

As can be seen from Fig. 4a, the experimental points lie on a straight line, which confirms the correctness of the determination from equation (8) of the numbers of coordination groups of ligands (m=n=1) in the polyligand complex $[Co(PPi)_m(Cit)_n]^{+2-(4m+3n)}$. Thus, polyligand cobalt (II) complexes $[Co(PPi)Cit]^{5-}$ are formed in the system under study at pH 9.0.

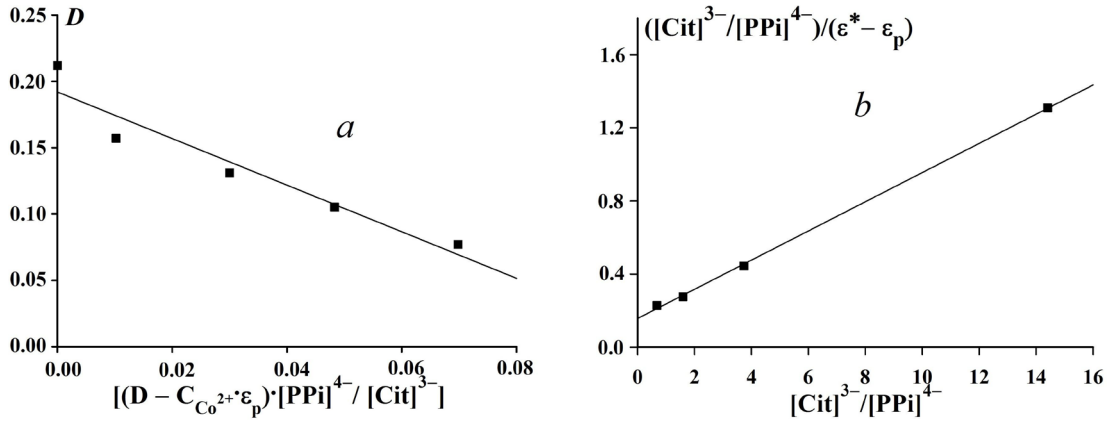

Fig. 4. Graphical determination of the equilibrium constant K_r of the polyligand cobalt (II) complexes formation reaction in pyrophosphate-citrate electrolyte at pH 9.0, wavelength λ = 500 nm by the method: (a) – Newman and Hume; (b) – Watters.

The equilibrium constant Kr of formation of $[Co(PPi)Cit]^{5-}$ polyligand complexes at pH 9 by reaction (3) was also determined by the Watters method [28] (Fig. 4b) according to the equation:

$$([Cit]^{3-}/[PPi]^{4-})/(\varepsilon^* - \varepsilon_p) = 1/[(\varepsilon_{зм} - \varepsilon_{пір}) \cdot K_r] + 1/(\varepsilon_{зм} - \varepsilon_{пір}) \cdot ([Cit]^{3-}/[PPi]^{4-}), \qquad (9)$$

where $\varepsilon_{Cit\text{-}PPi}$ and ε_{PPi} are the molar absorption coefficients of a polyligand and a pyrophosphate complex of cobalt (II), respectively; ε^* is the average coefficient of molar absorption of all forms of cobalt (II) ions.

The value of the equilibrium constant *K*r of the reaction of formation of polyligand complexes $[Co(PPi)Cit]^{5-}$ formation reaction, calculated from the slope of the linear plot of $([Cit]^{3-}/[PPi]^{4-})/(\varepsilon^* - \varepsilon_p) = f([Cit]^{3-}/[PPi]^{4-})$, which is $1/(\varepsilon_{Cit\text{-}PPi} - \varepsilon_{PPi}) = 0.0794$ (Fig. 4b), and the y-intercept $(1/(\varepsilon_{зм} - \varepsilon_{пір})K_r = 0.160)$ is 0.4963. The value of the equilibrium constant Kr of formation of polyligand complexes obtained by the Watters method [28] agrees with the Kr value obtained by the Newman and Hume method [27] (0.5755).

The stability constants of $[Co(PPi)Cit]^{5-}$ polyligand complexes calculated by the Watters [28], Newman and Hume [27] methods using the equilibrium constants Kr of the reaction of their formation of 0.4963 and 0.5755 respectively, in accordance with Eq. (4) are $2.76\cdot10^8$ ($p\beta = 8.44$) and $3.20\cdot10^8$ ($p\beta = 8.51$), respectively. The obtained average value of the stability constant of $[Co(PPi)Cit]^{5-}$ polyligand complexes ($\beta = 2.98\cdot10^8$ ($p\beta = 8.47$)) agrees with the value calculated from experimental data (Fig. 3a) by the equilibrium shift method ($p\beta = 8.26$).

Taking into account the stability constants of citrate $[Co(Cit)_2]^{4-}$ ($p\beta_2 = 5.30$), pyrophosphate $[Co(PPi)_2]^{6-}$ ($p\beta'_2 = 8.74$) and polyligand $[Co(PPi)Cit]^{5-}$ ($p\beta = 8.47$) complexes of cobalt (II), the dependence of the degree of their formation in a pyrophosphate-citrate electrolyte on the ratio of equilibrium concentrations of ligands lg ($[PPi]^{4-}/[Cit]^{3-}$) was calculated (Fig. 5). As can be seen from fig. 5, citrate complexes $[Co(Cit)_2]^{4-}$ exist in the range of the ratios of equilibrium concentrations of ligands lg ($[PPi]^{4-}/[Cit]^{3-}$) from –1 to +1, polyligand complexes $[Co(PPi)Cit]^{5-}$ in the range from –1 to +2, and $[Co(PPi)_2]^{6-}$ pyrophosphate complexes in the range >0.

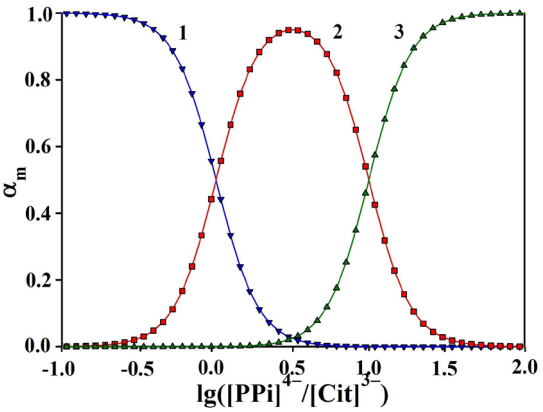

Fig. 5. Dependence of the degree of formation of citrate (1), polyligand (2) and pyrophosphate (3) complexes of cobalt (II) in pyrophosphate-citrate electrolyte on the logarithm of the ratio of equilibrium concentrations of ligands: *1* – $[Co(Cit)_2]^{4-}$; *2* – $[Co(PPi)Cit]^{5-}$; *3* – $[Co(PPi)_2]^{6-}$.

CONCLUSIONS.

It has been established that in a pyrophosphate-citrate electrolyte at pH 9.0, cobalt (II) ions form with Cit^{3-} and PPi^{4-} ions not only citrate $[Co(Cit)_2]^{4-}$ and pyrophosphate $[Co(PPi)_2]^{6-}$, but also polyligand complexes $[Co(PPi)_m(Cit)_n]^{+2-(4m+3n)}$. The composition of $[Co(PPi)Cit]^{5-}$ polyligand complexes was determined, the equilibrium constant *K*r of the reaction of their formation and their stability constant ($p\beta$=8.47) were calculated. In terms of stability, $[Co(PPi)Cit]^{5-}$ ($p\beta = 8.47$) polyligand complexes approach pyrophosphate complexes $[Co(PPi)_2]^{6-}$ ($p\beta'_2 = 8.74$). The dependence of the degree of formation of citrate, polyligand, and pyrophosphate complexes of cobalt

(II) in a pyrophosphate-citrate electrolyte on the logarithm of the ratio of equilibrium concentrations of ligands was calculated.

ACKNOWLEDGMENT. This work was carried out in the framework of the target research program of the NAS of Ukraine «Promising basic research and innovative development of nanomaterials and nanotechnologies for the needs of industry, health and agriculture», project № 28/22-N, 2022.

ВИЗНАЧЕННЯ ПОЛІЛІГАНДНИХ КОМПЛЕКСІВ КОБАЛЬТУ (II) З ЦИТРАТНИМИ ТА ПІРОФОСФАТНИМИ ІОНАМИ

В. М. Нікітенко, Ю. С. Японцева*, В. С. Кублановський

Інститут загальної та неорганічної хімії ім. В. І. Вернадського НАН України, просп. Академіка Палладіна, 32/34, Київ 03142, Україна
**e-mail: juliya_yap@ukr.net*

Спектрофотометричним методом встановлено, що у пірофосфатно-цитратному електроліті іони кобальту (II) утворюють залежно від співвідношення концентрацій лігандів $[PPi^{4-}]$ / $[Cit^{3-}]$ не тільки цитратні $[Co(Cit)_2]^{4-}$, пірофосфатні $[Co(PPi)_2]^{6-}$, а й полілігандні комплекси $[Co(PPi)_m(Cit)_n]^{+2-(4m+3n)}$. Визначено склад полілігандних комплексів $[Co(PPi)Cit]^{5-}$, обчислено константу рівноваги реакції їхнього утворення та константу їхньої стійкості ($p\beta = 8.47$). Розраховано залежність ступеня утворення цитратних, полілігандних та пірофосфатних комплексів кобальту(II) в пірофосфатно-цитратному електроліті від логарифму співвідношення рівноважних концентрацій лігандів.

Ключові слова: кобальт (II), полілігандні комплекси, склад, константа стійкості, спектрофотометрія.

REFERENCES

1. Yapontseva Y.S., Maltseva T.V. Kublanovsky V.S. Corrosion Properties of Electrolytic Coatings Based on CoW, CoRe, and CoWRe Alloys. *Mater Sci.* 2021. **56**: 649–653.
2. Eliaz N., Gileadi E. Induced codeposition of alloys of tungsten, molybdenum and rhenium with transition metals, in: C.G. Vayenas, R.E. White, M.E. Gamboa-Aldeco (Eds.), *Modern Aspects of Electrochemistry*. **42**. Springer, New York. 2008. P. 191 (Chapter 4).
3. Yapontseva Yu. S., Maltseva T.V., Kublanovsky V.S., Vyshnevskyi O.A. Electrodeposition of CoWRe alloys from polyligand citrate-pyrophosphate electrolyte. *J. Alloys Compd.* 2019. **803**: 1–8.
4. Vernickaite E., Tsyntsaru N., Sobczak K., Cesiulis H. Electrodeposited tungsten-rich Ni-W, Co-W and Fe-W cathodes for efficient hydrogen evolution in alkaline medium. *Electrochimica Acta*. 2019. **318**: 597.
5. Yapontseva Yu., Maltseva T., Kublanovsky V. Electrosynthesis of nanostructured thin coatings with superalloys CoW, CoRe and CoWRe with valuable properties in hardness and corrosion Resistance. *Materials Today: Proceedings*. 2021. **35**: 584–587.
6. Naor A., Eliaz N., Gileadi E. Electrodeposition of Alloys of Rhenium with Iron-Group Metals from Aqueous Solutions *J. Electrochemical Society*. 2010. **157**: 422.
7. Naor A., Eliaz N., Gileadi E. Electrodeposition of rhenium–nickel alloys from aqueous solutions. *Electrochimica Acta*. 2009. **54**: 6028.

8. Silkin S. A., Belevskii S. S., Tsyntsaru N. I. et al., Shul'man A. I., Shchuplyakov A. N., and Dikusar A. I. Influence of Long-Term Operation of Electrolytes on the Composition, Morphology, and Mechanical Properties of Surfaces Produced at Deposition of Co–W Coatings from Citrate Solutions. *Surface Engineering and Applied Electrochemistry*. 2009. **45** (1): 1.
9. Tsyntsaru N., Cesiulis H., Donten M. et al., Sort J., Pellicer E., Podlaha-Murphy E. J. Modern Trends in Tungsten Alloys Electrodeposition with Iron Group Metals. *Surface Engineering and Applied Electrochemistry*. 2012. **48**(6): 491.
10. Gapon Ju.K., Sahnenko N.D., M.V. Ved', Nenastina T.A. Zakonomernosti obrazovanija kompleksov kobal'ta (II). *Visnyk NTU HPI.* 2014. **51**: 136 (in Russian).
11. Sillen L.G., Martell A. E. Stability Constants of Metal–Ion Complexes and Supplement. Special Publications No. 17 and 25. London: The Chemical Society. 1964. **1**. 1971: **2**.
12. Zhao-Hui, Yuan-Fu Dong, and Hui-Lin Wan. Structural Diversities of Cobalt(II) Coordination Polymers with Citric Acid. *Crystal Growth & Design*. 2005. **5** (3): 1109.
13. Galloway K. W., Whyte A. M., Wernsdorfer W., Sanchez-Benitez J., Kamenev K. V., Parkin A., Peacock R. D., Murrie M. Cobalt(II) Citrate Cubane Single-Molecule Magnet. *Inorg. Chem*. 2008. **47**: 7438.
14. Kotsakis N., Raptopoulou C.P., Tangoulis V., Terzis A., Giapintzakis J., Jakusch T., Kiss T., Salifoglou A. Correlations of Synthetic, Spectroscopic, Structural, and Speciation Studies in the Biologically Relevant Cobalt(II)-Citrate System: The Tale of the First Aqueous Dinuclear Cobalt(II)-Citrate Complex. *Inorg. Chem.* 2003. **42**: 22.
15. Matezapetakis M., Dakanali M., Raptopoulou C.P. et al. Tangoulis V., Terzis A., Moon N., Giapintzakis J., Sulifoglou A. Synthetic, Spectroscopic, and Structural characterization of the first aqueous Cobalt(II)-Citrate complex: toward a potentially bioavailable form of cobalt in biologically relevant fluids. *JBIC*. 2000. **5**: 469.
16. Wyrzykowski D., Chmurzynski L. Thermodynamics of Citrate complexation with Mn^{2+}, Co^{2+}, Ni^{2+} and Zn^{2+} ions *J. Therm. Anal. Calorim*. 2010. **102**: 61.
17. Babko A.K. Physicochemical analysis of complex compounds in solutions. Kyiv: Publishing House of the USSR Academy of Sciences, 1955 (in Russian).
18. H.L. Schläfer, Komplexbildung in Lösung. Springer-Verlag: Berlin, Göttingen, Heidelberg. 1961 (in German).
19. Kravtsov V.I. Equilibrium and kinetics of electrode reactions of metal complexes. Khimiya, Leningrad. 1985 (in Russian).
20. Kratkij spravochnik po himii. Eds. O.D. Kurilenko. K.: Nauk. dumka. 1974 (in Russian).
21. Beck M., Nagypal I. Chemistry of complex equilibria. Budapest: Akademiai Kiado. 1989.
22. Drago R.S. Physical methods in chemistryю Saunders company: Philadelphia, London, Toronto. 1978.
23. Babko A.K., Pilipenko A.T. Kolorimetricheskij analiz. M.: L.: GNTI. 1951 (in Russian).
24. Babko A.K., Pjatnickij I.V. Kolichestvennyj analiz. M.: Vysshaja shkola. 1962 (in Russian).
25. Spektroskopicheskie metody v himii kompleksnyh soedinenij. Eds. V.M. Vdovenko. M., L.: Himija. 1964 (in Russian).
26. Rossotti F.J.C., Rossotti H. The determination of stability constants and other equilibrium constants in solution. McGraw-Hill book company: New York, Toronto, London, 1961.
27. Newman L., Hume D.N. Determination of Successive Formation Constants by Spectrophotometry. *J. Amer. Chem. Soc*. 1957. **79**: 4571.
28. Watters J.I., Mason J., Aaron A. J. Spectrophotometric Investigation of the Mixed Complex Formed by Copper Ions with Ammonium and Pyrophosphate ions in Aqueous Solutions *J. Amer. Chem. Soc*. 1953. **75**: 5212.

Стаття надійшла 18.04.2022.